NASA
Contractor Report 4077

AVSCOM
Technical Report 87-C-17

A Computer Solution for the Dynamic Load, Lubricant Film Thickness and Surface Temperatures in Spiral Bevel Gears

H. C. Chao and H. S. Cheng

GRANT NSG-3143
JULY 1987

NASA

US ARMY
AVIATION
SYSTEMS COMMAND
AVIATION R&T ACTIVITY

NASA
Contractor Report 4077

AVSCOM
Technical Report 87-C-17

A Computer Solution for the Dynamic Load, Lubricant Film Thickness and Surface Temperatures in Spiral Bevel Gears

H. C. Chao and H. S. Cheng
Northwestern University
Evanston, Illinois

Prepared for
Propulsion Directorate
USAARTA-AVSCOM and
NASA Lewis Research Center
under Grant NSG-3143

National Aeronautics
and Space Administration

**Scientific and Technical
Information Office**

1987

A COMPUTER SOLUTION FOR THE DYNAMIC LOAD, LUBRICANT FILM THICKNESS AND SURFACE TEMPERATURES IN SPIRAL BEVEL GEARS

SUMMARY

A complete analysis of spiral bevel gear sets is presented. The gear profile is described by the movements of the cutting tools. The contact patterns of the rigid body gears are investigated. The tooth dynamic force is studied by combining the effects of variable teeth meshing stiffness, speed, damping and bearing stiffness. The lubrication performance is also accomplished by including the effects of the lubricant viscosity, ambient temperature and gear speed. A set of numerical results is also presented.

TABLE OF CONTENTS

CHAPTER I

INTRODUCTION

Spiral bevel gears, found in many machine tools, automobile differential gears, and aircraft gears, are important elements for power transmissions. However, the basic mechanisms which govern the major failure modes of spiral bevel gears are not fully understood. Unlike spur or helical gears, the complicated geometry of spiral bevel gears makes the problem considerably more difficult. In military applications such as gear transmissions used in recent V/STOL aircraft, gears are often designed under conditions very close to the failure limits to gain a maximum power density. A thorough understanding of spiral bevel gears under critical operation is urgently needed to prevent premature failure.

Basically, there are two classifications of gear failure, one of which is structural failure, which includes flexure fatigue, tooth breakage and case crushing, and the other is the lubrication related failure which includes wear, surface pitting and scuffing.

Structural failures are usually related to the material properties and improper geometrical design or unexpected overloading. While the reliability of spiral bevel gears can be improved by better material selection and better geometrical design, it can also be enhanced by a more accurate understanding of the dynamic loading between a pair of

teeth as it travels through the contact.

Since the basic lubrication process in bevel gears is not clearly understood, the lubrication related failures,particularly in surface pitting and scuffing,are much more difficult to predict. Current methods used in industries to predict lubrication related failures are not satisfactory because they are mainly empirical. It has been shown in failure tests of gears and rollers that the surface pitting and scuffing are affected critically by lubricant film thickness and surface temperature. A tool that can predict film thickness and surface temperature in the gear teeth contact is welcome in design against pitting and scuffing.

This paper presents an analysis to predict the dynamic loads between gear teeth contact which has a contact ratio greater than unity and a variable stiffness along the path of contact. In addition, an analysis is presented to predict the minimum film thickness and the surface temperature under given dynamic loads. It is based on the most recent theories on film thickness and traction in elastohydrodynamic contacts.

CHAPTER II

TOOTH PROFILE AND CONTACT PATTERN OF SPIRAL BEVEL GEARS

2.1 Introduction

Recent developments in the finite element method (FEM) and elastohydrodynamic lubrication (EHD) have stimulated a growing interest in the basic research of the dynamics and lubrication process in spur and helical gears (1-6). This interest is now gradually being extended to spiral bevel gears for which there seems to be little known about the tooth load sharing and lubrication characteristics, especially at high speeds and heavy loads.

Unlike involute spur and helical gears whose surface geometry is relatively simple and readily derivable, the surface geometry of spiral bevel gears is extremely complex owing to its three dimensional characteristics. For studying the performance and failure of spiral bevel gears, it is essential first to find an efficient method to describe the surface geometry of a pair of mating gears in terms of the tooth form and the tooth contact patterns. Although this method is currently available at Gleason Gear Works (7-11), it is not fully sufficient for studying the dynamic load and lubrication analysis. It is the intent of this research to extend the existing surface geometry analysis, known as the Tooth Contact Analysis (TCA), to generate additional quantities needed for the lubrication and dynamic analysis.

The formulae for obtaining the coordinates of tooth surfaces based on the Gleason generating system are derived in Section 2.2. The position of each point on the surface is described in cylindrical coordinates in terms of its position along the rotational axis of the pinion or gear, its radial distance from the axis, and its angular position about the axis from an arbitrarily chosen reference plane. The equations are solved by an iterative method.

The contact points of a pair of mating gears and pinions for a running position are determined in Section 2.3. The sliding velocity and the direction of the unit normal vector at each contact point can be obtained. In addition, the principal radii of the mating surfaces which characterize the geometry at the contact point can be computed.

Some numerical results of a typical case are shown in Section 2.4. The effect of different running positions on contact patterns are studied. Finite element grids of a typical spiral bevel tooth profile are presented.

2.2 Determination of Tooth Surfaces for Generated Spiral Bevel Gears

In Tooth Contact Analysis (TCA) the gear and pinion tooth surfaces are mathematically described by the machine settings and the cutter specifications used in making the gears. Before proceeding to describe TCA, it is first desirable to review some basic concepts of bevel gearing. The principal reference planes of a spiral bevel gearing system are shown in Fig. 2-1. The axial plane of a single gear is the plane containing the gear axis and a given point on the tooth surface. The pitch plane is the plane perpendicular to the axial plane and tangent to the pitch circle. The transverse plane is perpendicular to the axial plane and the pitch plane. Figure 2-2 and Figure 2-3 show, respectively, the sectional views in the axial and transverse plane of a bevel and pinion system, and illustrate the most common terms used in bevel gears.

In order to understand the formulae derived in this chapter, a brief explanation of the cutting process is in order. Figure 2-4 illustrates the Gleason cutting process -- 1) the wheel cutter used in cutting spiral gears, 2) the cradle which positions the cutter in reference to the work and carries it through its generating motion, and 3) the blank into which the teeth are cut. The dresser, which is used to restore the cutting action of the wheel by fracturing and tearing away the dull grains to expose fresh cutting edges or clear away the imbedded material, is shown in Figure 2-5. Before the teeth are cut, the wheel cutter is predressed to shape the cutter. The relation between rotation of the cradle and rotation of the work is controlled

by the rotation of a cam which rotates about a fixed center.

The formulae derived here are based on the kinematics of two contacting bodies. There is no relative velocity in the normal direction at the cutting point and the teeth are assumed to be rigid. The formulae are written in vector notation. Most of these vectors are self-explanatory except for the following two terms:

$\bar{A}(\bar{g},\theta)^R$, a rotation of vector $\bar{A}$ through an angle θ about the unit vector $\bar{g}$.

$(-,\bar{t},\bar{n})^T$, a 3 x 3 matrix to transform a vector into a new coordinate system having the base vectors indicated in the parentheses. Since the right hand cartesian coordinate is used, it is only necessary to indicate two base vectors.

2.2.1 Basic Formulae

To describe the manufacturing process, one needs to know the relationship among the rotating elements, and the relative movement between the work and these elements.

2.2.2 Data Defining the Gear Tooth Surface

The gear tooth surfaces are controlled by the machine settings. The symbols of data required are listed in Table I. Sample data are given in Appendix A. These values are usually tabulated on a Gleason Gear Engineering Standard form.

A spiral bevel gear and pinion are always of opposite hand. The formulae considered here apply to a set consisting of a left-hand pinion shown

TABLE I

SYMBOLS OF DATA FOR MACHINE SETTING

	Gear	Pinion	
		Concave	Convex
Number of teeth	N	n	
Face width		F	
Shaft angle		Σ	
Outer cone distance		A_0	
Addendum	a_g	a_p	
Dedendum	b_g	b_p	
Pitch angle	Γ	τ	
Face angle	Γ_0	τ_0	
Root angle	Γ_r	τ_r	
Spiral angle		ψ_M	
Nominal wheel diameter		D_ω	
Machine center to back	X_g	X_p	X_p
Sliding base	X_{bg}	X_{bp}	X_{bp}
Blank offset	E_{mg}	E_{mp}	E_{mp}
Cam setting	T_g	T_p	T_p
Eccentric angle	β_g	β_p	β_p
Cradle angle	Q_g	Q_p	Q_p
Cam guide angle	α_g	α_p	α_p
Standard cam setting	T_{g0}	T_{p0}	T_{p0}
Cam pitch radius	ηu_g	ηu_p	ηu_p
Index interval	n_{ig}	n_{ip}	n_{ip}

TABLE I (continued)

	Gear	Pinion	
		Concave	Convex
Dresser block angle		$\Sigma\phi_d$	
Outside pressure angle	ϕ_{dg}	ϕ_{dp}	ϕ_{dp}
Side dresser radial	r_{dg}	r_{dp}	r_{dp}
Outside dresser arm length	L_{dog}	L_{dop}	L_{dop}
Outside diamond setting	X_{dog}	X_{dop}	X_{dop}
Inside dresser arm length	L_{dig}	L_{dip}	L_{dip}
Inside diamond setting	X_{dig}	X_{dip}	X_{dip}
Side dresser axial	Z_{dg}	Z_{dp}	Z_{dp}
Side dresser offset	E_{dg}	E_{dp}	E_{dp}

in Figure 2-6 and right-hand gear shown in Figure 2-7. The drive side is assumed to be the concave side of the pinion running with the convex side of the gear. The opposite combination is the coast side. Since the gear tooth data define the side under consideration, these general formulae apply to either the drive side or the coast side.

2.2.3 Mechanism of Cam

The relative rotation of the work and cradle is controlled by the index head and cam. The index head is used to transfer accurately the rotation ratio between the cam and workpiece. By describing the motion of the cam with a specific index head setting, one can obtain the rotations of the work and cradle, and their angular speed ratio.

The follower of the heart-shaped cam is fixed in the cradle, and the cam rotation center is fixed. Figure 2-8 shows the position for a standard cam setting. As the cam rotates about its own rotation center, the fixed follower forces the cradle to rotate about its center. The required rotation of the work is obtained by using the proper indexing. The relative motion can be readily changed by using a different cam geometry, cam setting, cam guide angle and index interval.

The symbols used in the motion formulae are:

ε cam rotation

λ work rotation

ψ cradle rotation

α cam guide angle

$\Delta\eta_u$ change in cam setting

η_u cam pitch radius

T cam setting

T_o standard cam setting

For a standard heart-shaped cam, the mechanism of motion of the cam and cradle at center of roll can be thought of as a pair of internal gears which has a pitch radius η_u for the pinion and DC + η_u for the gear (see Figure 2-9). If the cam rotates an angle ε_o, the cradle will rotate an angle $\eta_u/(\eta_u + DC)$ times ε_o.

The change in cam setting $\Delta\eta_u$ is defined as the actual cam setting T minus the standard cam setting T_o (see Figure 2-10). The dashed lines are for the standard cam setting for a rotation ε_o. For a change in $\Delta\eta_u$, the following relations are derived.

$$\psi_o = \frac{\eta_u}{DC + \eta_u \varepsilon_o} \varepsilon_o \tag{2.1}$$

$$\sin \psi = \sin \psi_o + \frac{\Delta\eta_u}{DC} \sin(\varepsilon_o - \psi_o) \tag{2.2}$$

$$\varepsilon = \varepsilon_o + \psi - \psi_o \tag{2.3}$$

where ψ and ε are the actual rotations for the current setting.

A center line of the follower is parallel to and is in the middle of the follower surfaces. The cam guide angle is defined as the angle between this center line and the line from the cradle center to the cam rotation center before the cam rotates (see Figure 2-11a). Because the follower is fixed in the cradle, the distance from the cradle center

to the center line of the follower is constant and is always equal to DC sin α.

Figure 2-11b shows the relative positions with a cam guide angle. Using ε_o as the standard cam rotation angle, one obtains

$$\psi_0 = \frac{\eta_u}{DC + \eta_u} \varepsilon_0 \tag{2.4}$$

$$\sin \psi_2 = \sin \psi_0 + \sin \alpha \tag{2.5}$$

$$\psi = \psi_2 - \alpha \tag{2.6}$$

$$\varepsilon_2 = \varepsilon_0 + \psi_2 - \psi_0 \tag{2.7}$$

$$\varepsilon = \varepsilon_2 - \alpha \tag{2.8}$$

If both the cam setting and the cam guide angle are changed, one can find the following relations based on the geometry shown in Fig. 2-12 for a standard cam rotation ε_o:

$$\psi_0 = \frac{\eta_u}{DC + \eta_u} \varepsilon_0 \tag{2.9}$$

$$\sin \psi_2 = \sin \psi_0 + \sin \alpha + \frac{\Delta \eta_u}{DC} \sin(\varepsilon_0 - \psi_0) \tag{2.10}$$

$$\psi = \psi_2 - \alpha \tag{2.11}$$

$$\varepsilon_2 = \varepsilon_0 + \psi_2 - \psi_2 \tag{2.12}$$

$$\varepsilon = \varepsilon_2 - \alpha \tag{2.13}$$

$$\lambda = \frac{n_i}{n} \quad \varepsilon \tag{2.14}$$

The ratio between the cradle and the work rotation becomes

$$\frac{d\psi}{d\lambda} = \frac{n}{n_1} \frac{N_M}{D_M} \tag{2.15}$$

where

$$N_M = \eta_u \cos \psi_0 + \Delta\eta_u \cos(\varepsilon_0 - \psi_0) \tag{2.16}$$

$$D_M = N_M + DC \cos \psi_2 \tag{2.17}$$

These ratios of the rotational velocity and the rotation of the work and the cradle are necessary for computing the velocity and the normal direction at the contact point. Their derivations are shown in Appendix B.

2.2.4 Basic Machine Set-up and Vector Coordinate System

The cradle settings in the spiral bevel gear cutting machines of the Gleason Works are shown in Fig. 2-13. The settings are fixed during the cutting process. From this figure, the following relations are obtained.

$$s_p = 16 \sin \frac{\beta_p}{2} \tag{2.18}$$

$$q_{p0} = \frac{\beta_p}{2} - Q_p + 360° \tag{2.19}$$

$$s_g = 16 \sin \frac{\beta_g}{2} \tag{2.20}$$

$$q_{g0} = Q_g - \frac{\beta_g}{2} \tag{2.21}$$

Vectors in these formulae have been taken with respect to a set of right-hand rectangular cartesian coordinates, x, y, z fixed in the machine plane viewed from the front of the cutter toward the gear as shown in Fig. 2-14.

In order to be consistent with the vector formulae, the following matrix for unit vectors, $\overline{d}$, $\overline{e}$, and $\overline{c}$ is used.

$$\begin{aligned} \overline{d} &= (1, 0, 0) \\ \overline{e} &= (0, 1, 0) \\ \overline{c} &= (0, 0, 1) \end{aligned} \tag{2.22}$$

2.2.5 Point on the Gear

In cutting the gear, the moving parts include the rotating work, cradle, wheel cutter, cam, and dresser. The work rotation, cradle rotation and cam rotation are related to each other. It is desirable to choose cam rotation as the independent variable. Thus, there are only three independent rotations which define a specific point on the gear tooth surface, i.e. the cam, dresser, and wheel cutter.

The procedure to determine a point on the gear tooth surface is to choose arbitrary values for the cam rotation and wheel cutter rotation, then find a value of dresser rotation such that the kinematic requirement of contact is satisfied, i.e., the relative velocity at the cutting point is perpendicular to the normal of the point being cut in the gear tooth.

Symbols shown in Fig. 2-14 for all position vectors are

defined as:

$\overline{A}$: vector from the machine center to the point on the surface

$\overline{S}$: vector from the machine center to the intersection of plane containing the cutter tips and the wheel cutter axis.

$\overline{R}$: vector from the crossing point to the point on the surface.

$\overline{B}$: vector from wheel center to the point on the surface.

$\overline{r}$: vector from the intersection of plane containing the cutter tips and the wheel cutter axis to cutter tips.

$\overline{n}$: unit normal vector to the cutter blade.

$\overline{t}$: unit vector along the direction of dressing diamond movement.

$\overline{g}$: unit vector along the gear axis.

$\overline{p}$: unit vector along the pinion axis.

The initial position of these vectors when $q_g = 0$, $\theta_g = 0$ are

$$\overline{g} = (-\cos \Gamma_r,\ 0,\ -\sin \Gamma_r)$$

$$\overline{\gamma}_{go} = -\gamma_{dg}\ \overline{e}$$

$$\overline{S}_{go} = S_g\ \overline{d}$$

$$\overline{n}_{go} = (0,\ \cos \phi_g,\ \sin \phi_g)$$

$$\overline{t}_{go} = (0,\ \sin \phi_g,\ -\cos \phi_g)$$

Because the convex side of the gear tooth is formed by an inside blade of the cutter, by using the sign convention given below, the same

formulae (used in computer programs) can be used for both sides:

Drive Side	Coast Side
$\phi_g = \Sigma\phi_{dg} - \phi_{dg}$	$\phi_g = - \phi_{dg}$
$X_{dg} = X_{dig}$	$X_{dg} = - X_{dog}$
$L_{dg} = L_{dig}$	$L_{dg} = L_{dog}$

Reasonable initial values of cam rotation ε_{0g} (standard cam setting) and wheel rotation θ_g are

$$\varepsilon_{0g} \simeq 0 \tag{2.23}$$

$$\theta_g \simeq q_{g0} - \psi_M \tag{2.24}$$

where ψ_M is the spiral angle, using ε_{0g} from cam formulae to obtain ψ_g, λ_g and ratio of cradle rotation to work rotation. The new position vectors become

$$q_g = q_{g0} + \psi_g$$

$$\overline{S}_g = \overline{S}_{g0}(\overline{c},\ q_g)^R$$

$$\overline{r}_g = \overline{r}_{go}(\overline{c},\ q_g - \theta_g)^R$$

$$t_{1g} = t_{g0}(\overline{c},\ q_g - \theta_g)^R$$

$$\bar{n}_{1g} = \bar{n}_{go}(\bar{c},\ q_g - \theta_g)^R$$

$$\bar{d}_{1g} = \bar{d}_g(\bar{c},\ q_g - \theta_g)^R$$

$$\bar{B}_{g0} = \bar{r}_g - (0.2 - a_{dg})\,\bar{c} + X_{dg}\bar{n}_{1g} - (2.0 - E_{dg})\,\bar{d}_{1g} \qquad (2.25)$$

$$\bar{A}_{g0} = \bar{S}_g + \bar{B}_{g0}$$

$$\bar{R}_{g0} = X_g\,\bar{g} - \bar{E}mg\,\bar{e} - X_{bg}\,\bar{c} + \bar{A}_{g0}$$

where $\bar{B}_{g0}$: vector from wheel center to dresser center.

$\bar{A}_{g0}$: vector from machine center to dresser center.

$\bar{R}_{g0}$: vector from crossing point to dresser center.

After setting certain values for the two independent variables ε_{0g} and θ_g, one can determine the dresser angle θ_{dg} that satisfies the kinematic requirement of contact between tooth surface and cutter. To find this dresser angle θ_{dg}, an initial value ($\theta_{dg} \simeq 0$) is first assumed. From Fig. 2-14, the new position vectors are

$$\bar{d}_{2g} = \bar{d}_{1g}(\bar{n}_{1g},\ \theta_{dg})^R$$

$$\bar{t}_{2G} = \bar{t}_{1g}(\bar{n}_{1g},\ \theta_{dg})^R$$

$$\bar{A}_g = \bar{A}_{g0} + L_{dg}\bar{d}_{2g} \qquad (2.26)$$

$$\bar{R}_g = \bar{R}_{g0} + L_{dg}\bar{d}_{2g}$$

$$\bar{B}_g = \bar{B}_{g0} + L_{dg}\bar{d}_{2g}$$

The normal of the cutter blade at this instant (given ϵ_{0g}, θ_{eg} values) is

$$\bar{n}_g = \{ \bar{c} \times \bar{B}_g) \times \bar{t}_{2g} \}_{unit} \tag{2.27}$$

The velocity of the cutt er relative to the work at the point being cut is

$$\bar{V}_g = \left(\frac{d\psi}{c\lambda}\right)_g \bar{c} \times \bar{A}_g + \bar{g} \times \bar{R}_g \tag{2.28}$$

The product $\bar{n}_g \cdot \bar{V}$ is checked to see whether or not it is zero; if not, the secant method is used to iterate θ_{dg} until $\bar{n}_g \cdot \bar{V}_g = 0$ is satisfied for the prescribed values of ϵ_{0g} and θ_g.

The tooth surface can be described completely with the formulae derived so far by varying the values of ϵ_{0g} and θ_g independently.

2.2.6 Point on the Pinion

The procedure to find the pinion tooth surface is exactly the same as that for the gear tooth surface, except for some initial vectors which are different. From Fig. 2-15, the mathematical forms are described briefly as follows:

Drive Side	Coast Side
$\phi_p = \phi_{dp}$	$\phi_p = \phi_{dp} - \Sigma\phi_{dp}$
$X_{dp} = X_{dop}$	$X_{dp} = = X_{dip}$
$L_{dp} = L_{dop}$	$L_{dp} = L_{dip}$

The initial position vectors are:

$$\bar{p} = (-\cos \gamma_r,\ 0,\ -\sin \gamma_r)$$

$$\bar{S}_{p0} = S_p\ \bar{d}$$

$$\bar{r}_{p0} = r_{dp}\ \bar{e} \tag{2.29}$$

$$\bar{n}_{p0} = (0,\ -\cos \phi_p,\ -\sin \phi_p)$$

$$\bar{t}_{p0} = (0,\ -\sin \phi_p,\ \cos \phi_p)$$

Assume $\varepsilon_{0p} \simeq 0$, $\theta_p = q_{p0} - \psi_M$; one can calculate λ_p, ψ_p and ratio of cradle rotation to work rotation by cam formulae described earlier.

$$q_p = q_{p0} - \psi_p$$

$$\bar{S}_p = \bar{S}_{p0}(\bar{c},\ -q_p)^R$$

$$\bar{r}_p = \bar{r}_{p0}(\bar{c},\ \theta_p - q_p)^R$$

$$\bar{t}_{1p} = \bar{t}_{p0}(\bar{c},\ \theta_p - q_p)^R \tag{2.30}$$

$$\bar{n}_{1p} = \bar{n}_{p0}(\bar{c},\ \theta_p - q_p)^R$$

$$\bar{d}_{1p} = \bar{d}(\bar{c},\ \theta_p - q_p)^R$$

$$\bar{B}_{po} = \bar{r}_p - (0.2 - Z_{dp})\ \bar{c} - X_{dp}\ \bar{n}_{1p} - (2.0 - E_{dp})\ \bar{d}_{1p}$$

$$\bar{A}_{p0} = \bar{S}_p + \bar{B}_{p0}$$

$$\bar{R}_{p0} = x_p\ \bar{p} + E_{mp}\ \bar{e} - X_{bp}\ \bar{c} + \bar{A}$$

Assume a value of dresser angle θ_{dp}

$$\begin{aligned}
\bar{d}_{2p} &= \bar{d}_{1p}(\bar{n}_{1p},\ \theta_{dp})^R \\
\bar{t}_{2p} &= \bar{t}_{1p}(\bar{n}_{1p},\ \theta_{dp})^R \\
\bar{A}_p &= \bar{A}_{p0} + L_{dp}\,\bar{d}_{2p} \\
\bar{R}_p &= \bar{R}_{p0} + L_{dp}\,\bar{d}_{2p} \\
\bar{B}_p &= \bar{B}_{p0} + L_{dp}\,\bar{d}_{2p} \\
\bar{n}_p &= \{\bar{t}_{2p} \times (\bar{c} \times \bar{B}_p)\}_{unit} \\
\bar{V}_p &= \left(\frac{d\psi}{d\lambda}\right)_p \bar{c} \times \bar{A}_p + \bar{p} \times \bar{R}_p
\end{aligned} \tag{2.31}$$

change θ_{dp} until $\bar{V} \cdot \bar{n}_p = 0$.

The tooth surface of pinion is thus determined by changing the values of ε_{0p} and θ_p independently.

2.3 Tooth Contact Behavior and Motion Graph

The only tooth curvature of involute gears with an infinite lengthwise radius of curvature is the tooth profile curvature, so the instantaneous tooth contact pattern will be a straight line extending from one end of the tooth to the other. If elastic deformation is included, the contact pattern will be an elongated rectangle, from one end of the tooth to the other. If the teeth are crowned, lengthwise curvature is introduced. This results in a point contact for rigid teeth, or an elliptical contact for elastically deformed teeth.

Theoretical conjugate bevel gear teeth can be manufactured, but they are sensitive to shaft misalignment and housing deformation. Due to this, bevel gears are produced with a lengthwise and a profilewise mismatch. Therefore, the instantaneous tooth contact pattern will be a theoretical point for rigid teeth or an ellipse when elastic deformation is included.

By choosing the proper amount of mismatch in both directions for a particular case, edge contact and excessive contact pressure can be avoided in the presence of misalignment due to shaft and housing deformations.

The purpose of the motion graph is to describe the nature of the motion transmitted and the effects of contact between adjacent pairs of teeth on the tooth contact pattern.

The gear contact problem is essentially a Hertzian contact problem, with the pressure distribution in the Hertzian ellipse a main concern in EHD. The shape of the Hertzian ellipse can be readily determined

from the principal radii which can be computed analytically from the gear teeth geometry.

2.3.1 Matching a Contact Point

A method to find the contact point by machine setting and running position is derived in this section.

In addition to the rectangular cartesian coordinate used in Chapter II, a point on the tooth surface with respect to the tooth axis and the crossing point can be specified in the axial plane by:

L : the distance along the tooth axis from the crossing point.

R : the radius from the tooth axis.

The primary effect of misalignment is to shift the tooth contact to the boundaries of the tooth surface, resulting in edge contact and extreme loading conditions. Figure 2-16 shows a pair of spiral bevel gears; the following errors in relative running position of the pinion with respect to gear are discussed:

Σ_r : running shaft angle.

X_{pr} : pinion apex withdraw-which is the linear displacement in the H-direction (along the pinion axis).

X_{gr} : gear apex withdraw-which is the linear displacement in the Z-direction (along the gear axis).

E_r : offset-which is the linear displacement in the V-direction.

Consider a point on the gear tooth surface obtained by assumed values of ε_{0g} and θ_g as described in Section 2.2, in order to match the gear axis from its manufacturing position to a proper running position relative to the pinion axis. Suppose one lets the manufacturing axis of the pinion coincide with the pinion axis at running position. Then the gear axis at running position is as shown in Figure 2-17, and the new position vectors relative to the new gear axis are:

$$\mu = \lambda_g + \eta_g + \pi \tag{2.32}$$

$$\Delta\Sigma = \Sigma_r + \Gamma_r + \tau_r$$

$$\begin{Vmatrix} \bar{R}_{g1} \\ \bar{A}_{g1} \\ \bar{n}_{g1} \\ \bar{t}_{g1} \\ \bar{g}_1 \end{Vmatrix} = \begin{Vmatrix} \bar{R}_g \\ \bar{A}_g \\ \bar{n}_g \\ \bar{t}_{2g} \\ \bar{g} \end{Vmatrix} (\bar{g}, \mu)^R (\bar{e}, \Delta\Sigma)^R \tag{2.33}$$

where μ_g is the desired rotation angle of the gear from a specified reference. In the computer program, η_g is set at zero to find the first contact point, and then is increased to obtain the successive contact points.

Assuming that a point P on the gear surface obtained by a pair

of values ε_{0g} and θ_g is a contact point under running conditions, the position vector for this point expressed in the pinion axis can be obtained by placing the gear in running position relative to the pinion as shown in Figure 2-18

$$\overline{R}_{pl} = X_{pr}\overline{p} + E_r\overline{e} - X_{gr}\overline{g}_l + \overline{R}_{gl} \tag{2.34}$$

One can define this contact point P in the pinion without considering its angular position by

$$\begin{aligned} L_{pl} &= -\overline{R}_{pl} \cdot \overline{p} \\ R_{pl} &= |\overline{R}_{pl} \times \overline{p}| \end{aligned} \tag{2.35}$$

In the manufacturing procedure, there is a set of particular values of ε_{0p} and θ_p to produce a point in the pinion with the same values of L_p and R_p as those of L_{pl} and R_{pl}.

The mathematical way to find these particular values of ε_{0p} and θ_p is described as follows.

Assuming arbitrarily ε_{0p} and θ_p and using the method described in section 2.2, one can get $\overline{R}_p$ which is the vector from crossing point to the contact point Q between cutter blade and work. The vector $\overline{R}_p$ can be specified by

$$\begin{aligned} L_p &= -\overline{R}_p \cdot \overline{p} \\ R_p &= |\overline{R}_p \times \overline{p}| \end{aligned} \tag{2.36}$$

Iterate ε_{0p} and θ_p simultaneously until $L_p = L_{p1}$ and $R_p = R_{p1}$, that is, the same distance around the pinion axis from crossing point is obtained for point Q and point P.

Then rotate the pinion axis to make point Q coincide with the contact point P; the rotation angle required, $\Delta\eta_p$, is shown in Figure 2-19.

$$\Delta\eta_p = \sin^{-1}\left(\frac{\bar{R}_p \cdot (\bar{R}_{p1} \times \bar{p})}{R_p^2}\right) \tag{2.37}$$

Point P is obtained under the assumption that arbitrary values of ε_{0g} and θ_g were made. Under a given tooth profile and running position, not every point in the tooth could be a common contact point. A common contact point must have the same normal direction for both pinion and gear.

Assuming that a point P is the common contact point, the normal direction at this point on the gear for ε_{0g} and θ_g is $\bar{n}_{g1}$, on the pinion it is

$$\bar{n}_{p1} = \bar{n}_p(\bar{p}, \Delta\eta_p)^R \tag{2.38}$$

where $\bar{n}_p$ is obtained at point Q. n_{g1} and n_{p1} are compared to see if they agree to within a specified error. If not, the secant method is used to to change ε_{og} and θ_g simultaneously to find another contact point until the two normal directions agree. This procedure yields a point of contact between gear and pinion.

In fully matched gears, the constant velocity ratio is maintained. In single mismatch case (lengthwise mismatch) the theoretical contact point is a point of the original surface, so the uniform velocity will be maintained. There is only one theoretical contact point in combined mismatch, the point of the original surface; therefore, the velocity ratio will not remain constant, and there is a theoretical instantaneous velocity change at each changeover.

The motion graph shows the error in angular displacement of the driven member against rotation of the driver. It is assumed throughout that the pinion is the driving member and that it is rotating at a constant velocity.

2.3.2 Condition of Contact

The surface topography of spiral bevel gears cannot be readily expressed mathematically by an analytical function. However, one can use second-order surface approximations to describe the surface around a point of contact. By this approximation the principal radii and relative surface velocity at the contact point can be analytically determined. Approximating a surface to the second order gives

$$z = 0.5\ a\ x^2 + b\ x\ y + 0.5\ c\ y^2 \qquad (2.39)$$

The numeric coefficients were chosen so that

$$a = \frac{\partial^2 z}{\partial x^2}$$ curvature in x-direction

$$b = \frac{\partial^2 z}{\partial x \partial y} \qquad \text{twisting} \tag{2.40}$$

$$c = \frac{\partial^2 z}{\partial y^2} \qquad \text{curvature in y-direction}$$

express this surface equation in compact form $(s) = \begin{pmatrix} a & b \\ b & c \end{pmatrix}$.

Except for the tooth breakage, the tooth failure modes are mainly due to local contact pressure which causes surface pitting or scoring at high sliding velocities. Therefore, to develop reliable formulae for gear design it is necessary to have knowledge of contact pressure and surface velocity on the gear tooth.

2.3.2.1 Surface Coefficients

Figure 1-20 shows the surface at the point of contact for the gear. The tangent plane coordinate system is chosen in such a way that the plane containing the normal direction vector of contact point ($\bar{n}_g$) and the vector $\bar{c}$ of wheel axis is the yz plane of the tangent plane coordinate system as shown. Let $\bar{t}_g$ coincide with y axis and $\bar{n}_g$ with z axis, so the vector $\bar{t}_g \times \bar{n}_g$ is in the direction of the x-axis.

In this chosen tangent plane coordinate system, there is no twisting for the surface of the generator which is the wheel surface around the point of contact ($b_{s\omega g} = 0$) and the curvature in the x-axis direction of this generator surface ($a_{s\omega g}$) can be derived based on the geometry shown in Figure 2-20.

$$\sin \psi_{\omega g} = \bar{n}_g \cdot \bar{c} \tag{2.41}$$

$$r_{ng} = |\bar{B}_g \times \bar{c}| \sec \psi_{\omega g} \tag{2.42}$$

$$a_{s\omega g} = \frac{1}{r_{ng}} \tag{2.43}$$

The curvature in the y-axis direction ($c_{s\omega g}$) is shown in Fig. 2-21.

$$\bar{t}_g = \bar{n}_g \tan \psi_{\omega g} - \bar{c} \sec \psi_{\omega g}$$

$$\sin i_g = \bar{n}_{1g} \cdot (\bar{t}_{2g} \times \bar{n}_g) \tag{2.44}$$

$$\sin \alpha_{\omega g} = \bar{t}_{2g} \cdot (\bar{t}_g \times \bar{n}_g)$$

$$x = L_{dg} \sin \alpha_{\omega g}\, \theta + \text{---} \tag{2.45}$$

$$y = L_{dg} \cos \alpha_{\omega g}\, \theta + \text{---} \tag{2.46}$$

$$\Delta = 0.5\, L_{dg} (\sin i_g) \theta^2 - 0.5 x^2 \frac{1}{r_{ng}} \tag{2.47}$$

$$= 0.5\, \theta^2 \left[-L_{dg} \sin i_g - \frac{L_{dg}^2}{r_{ng}} \sin^2 \alpha_{\omega g}\right]$$

but $$\Delta = 0.5\, y^2 \frac{1}{\rho_{\omega g}}$$

hence $$\frac{1}{\rho_{\omega g}} = \frac{1}{L_{dg}} \frac{\sin i_g}{\cos^2 \alpha_{\omega g}} - \frac{1}{r_{ng}} \tan^2 \alpha_{\omega g} \tag{2.48}$$

$$c_{s\omega g} = \frac{1}{\rho_{\omega g}} \tag{2.49}$$

where $\rho_{\omega g}$ is the radius of curvature in y-axis direction.

In the actual running position, the z-axis of the tangent plane is $\bar{n}_{gl}$ and the y-axis is

$$\bar{t}_{gt} = \bar{t}_g(\bar{g},\mu)^R \ (e,\ \Delta\Sigma)^R \tag{2.50}$$

For the pinion, the surface of the generator around the point of contact is shown in Fig. 2-22, and surface coefficients $a_{s\omega p}$, $b_{s\omega p}$ and $c_{s\omega p}$ can then be obtained:

$$\sin \psi_{\omega p} = -\bar{n}_p \cdot \bar{c} \tag{2.51}$$

$$\bar{t}_p = \bar{n}_p \tan \psi_{\omega p} + \bar{c} \sec \psi_{\omega p} \tag{2.52}$$

$$\sin i_p = \bar{n}_{lp} \cdot (\bar{t}_{2p} \times \bar{n}_p) \tag{2.53}$$

$$\sin \alpha_{\omega p} = \bar{t}_{2p} \cdot (\bar{t}_p \times \bar{n}_p) \tag{2.54}$$

$$r_{np} = |\bar{B}_p \times \bar{c}| \sec \psi_{\omega p} \tag{2.55}$$

$$\frac{1}{\rho_{\omega p}} = \frac{1}{L_{dp}} \frac{\sin i_p}{\cos^2 \alpha_{\omega p}} - \frac{1}{r_{np}} \tan^2 \alpha_{\omega p} \tag{2.56}$$

$$a_{s\omega p} = \frac{1}{r_{np}}$$

$$b_{s\omega p} = 0 \qquad (2.57)$$

$$c_{s\omega p} = \frac{1}{\rho_{\omega p}}$$

In the real running position, the tangent plane coordinate in the z-axis direction is

$$\bar{n}_{pl} = \bar{n}_{gl} \qquad (2.58)$$

and in the y-axis direction is

$$\bar{t}_{pt} = \bar{t}_{p}(\bar{p},\ \Delta\eta_{p})^{R} \qquad (2.59)$$

One uses the vectorial velocity and acceleration of a known point on the wheel and angular velocity vector of the wheel about that point to describe the movement of the generator. This point is chosen as a point of contact at a given instant. The motion parameters are:

$\bar{V}$: linear velocity vector.

$\bar{a}$: linear acceleration vector.

$\bar{\omega}$: angular velocity vector.

The above are relative motion vectors denoting the motion of a moving generator relative to a generatee.

The values of these motion parameters can be computed for the gear as follows (see Fig. 2-23 for direction of vectors):

$$\omega_{cg} = \left(\frac{d\psi}{d\lambda}\right)_g \quad , \quad \alpha_{cg} = \left(\frac{d^2\psi}{d\lambda^2}\right)_g \tag{2.60}$$

$$\bar{\omega}_g = {}_{cg}\bar{c} + \bar{g} \tag{2.61}$$

$$\bar{E}_g = \bar{R}_g - \bar{A}_g \tag{2.62}$$

$$\bar{V}_g = \bar{g} \times \bar{E} + \bar{\omega}_g \times \bar{A}_g \tag{2.63}$$

$$\bar{a}_g = \bar{g} \times (\bar{g} \times \bar{E}_g) + (\omega_{cg}\, \bar{g} \times \bar{c} + \alpha_{cg}\, \bar{c}) \times \bar{A}_g \tag{2.64}$$

$$+ \bar{\omega}_g \times (\bar{\omega}_g \times \bar{A}_g) \tag{2.64}$$

Transforming these vectors to tangent plane coordinates:

$$\bar{\omega}_{tg} = \bar{\omega}_g(-, \bar{t}_g, \bar{n}_g)^T$$

$$\bar{V}_{tg} = \bar{V}_g(-, \bar{t}_g, \bar{n}_g)^T \tag{2.65}$$

$$\bar{a}_{tG} + \bar{a}_G(-, \bar{t}_g, \bar{n}_g)^T$$

Similarly, for the pinion, one obtains

$$\omega_{cp} = \left(\frac{d\psi}{d\lambda}\right)_p \quad , \quad \alpha_{cp} = \left(\frac{d^2\psi}{d\lambda^2}\right)_p \tag{2.66}$$

$$\bar{\omega}_p = \omega_{cp}\,\bar{c} + \bar{p} \tag{2.67}$$

$$\bar{E}_p = \bar{R}_p - \bar{A}_p \tag{2.68}$$

$$\bar{V}_p = \bar{p} \times \bar{E}_p + \bar{\omega}_p \times \bar{A}_p \tag{2.69}$$

$$\bar{a}_p = \bar{p} \times (\bar{p} \times \bar{E}_p) + (\omega_{cp}\,\bar{p} \times \bar{c} + \alpha_{cp}\,\bar{c}) \times \bar{A}_p + \bar{\omega}_p \times (\bar{\omega}_p \times \bar{A}_p) \tag{2.70}$$

Transforming to the tangent plane coordinate system,

$$\bar{\omega}_{tp} = \bar{\omega}_p(-,\ \bar{t}_p,\ \bar{n}_p)^T$$

$$\bar{V}_{tp} = \bar{V}_p(-,\ \bar{t}_p,\ \bar{n}_p)^T \tag{2.71}$$

$$\bar{a}_{tp} = \bar{a}_p(-,\ \bar{t}_p,\ \bar{n}_p)^T$$

The problem is, then, to determine the three components of the difference surface matrix (Δa, Δb, Δc) in terms of the given surface components and the motion parameters. From 2.12, the following relations are obtained for the gear (subscripts x,y,z denote the component of a vector):

$$\tan \alpha_{sg} = \frac{\omega_{tgy} + a_{s\omega g} V_{tgx}}{\omega_{tgx} - c_{s\omega g} V_{tgy}} \tag{2.72}$$

$$v_g = - \frac{a_{tgz} + V_{tgx} \omega_{tgy} - V_{tgy} \omega_{tgx}}{\omega_{tgx} - c_{s\omega g} V_{tgy}} \tag{2.73}$$

$$\Delta c_g = \frac{\omega_{tgy} - c_{s\omega g} V_{tgy}}{v_g + V_{tgy} - V_{tgx} \tan \alpha_{sg}} \tag{2.74}$$

$$\Delta b_g = - \Delta c_g \tan \alpha_{sg} \tag{2.75}$$

$$\Delta a_g = - \Delta b_g \tan \alpha_{sg} \tag{2.76}$$

The coefficients of the surface of the gear around the contact point are:

$$\begin{aligned} a_{sg} &= a_{s\omega g} + \Delta a_g \\ b_{sg} &= \Delta b_g \\ c_{sg} &= c_{s\omega g} + \Delta c_g \end{aligned} \tag{2.77}$$

for the pinion:

$$\tan \alpha_{sp} = \frac{\omega_{tpy} + a_{s\omega p} V_{tpx}}{\omega_{tpx} - c_{s\omega p} V_{tpy}} \tag{2.78}$$

$$v_p = - \frac{a_{tpz} + V_{tpx}\,\omega_{tpy} - V_{tpy}\,\omega_{tpx}}{\omega_{tpx} - c_{s\omega p}\,V_{tpy}} \tag{2.79}$$

$$\Delta c_p = \frac{\omega_{tpx} - c_{s\omega p}\,V_{tpy}}{v_p + V_{tpy} - V_{tpx}\tan\alpha_{sp}}$$

$$\Delta b_p = -\Delta c_p \tan\alpha_{sp} \tag{2.80}$$

$$\Delta a_p = -\Delta b_p \tan\alpha_{sp}$$

The coefficients of the surface of the pinion in the pinion tangent plane coordinate system are

$$a_{sp} = a_{s\omega p} + \Delta a_p$$

$$b_{sp} = \Delta b_p \tag{2.81}$$

$$c_{sp} = c_{s\omega p} + \Delta c_p$$

It is necessary to rotate the pinion tangent plane coordinate system to coincide with the gear tangent plane coordinate system in order to express the coefficients of both surfaces in the same coordinate system. The angle required for rotation is Δ which can be found from

$$\sin\Delta = \bar{t}_{pt} \cdot (\bar{t}_{gt} \times \bar{n}_{gl}) \tag{2.82}$$

and then to transform the coefficients of the pinion surface into this coordinate system,

$$a_{spg} = a_{sp} \cos^2 \Delta + 2\, b_{sp} \cos \Delta \sin \Delta + c_{sp} \sin^2 \Delta$$

$$b_{spg} = (c_{sp} - a_{sp}) \cos \Delta \sin \Delta + b_{sp}(\cos^2 \Delta - \sin^2 \Delta) \qquad (2.83)$$

$$c_{spg} = c_{sp} \cos^2 \Delta - 2\, b_{sp} \cos \Delta \sin \Delta + a_{sp} \sin^2 \Delta$$

2.3.2.2 Geometric Contact Ellipse

Using a value of 0.00025" for the separation at the extremities of the contact and the surface curvatures of each member at the point of contact, the size and direction of the contact ellipse are determined as (Fig. 2-24).

$$\Delta a = a_{spg} - a_{sg}$$

$$\Delta b = b_{spg} - b_{sg} \qquad (2.84)$$

$$\Delta c = c_{spg} - c_{sg}$$

$$\tan 2g = \frac{2\Delta b}{\Delta a - \Delta c}$$

The two values of g are the principal directions. Assuming that g_2 is in first or fourth quadrant, the curvatures in the g_1 and g_2 directions are:

$$\frac{1}{\rho_1} = \Delta a \cos^2 g_1 + 2\,\Delta b \cos g_1 \sin g_1 + \Delta c \sin^2 g_1$$

$$\frac{1}{\rho_1} = \Delta a \cos^2 g_2 + 2\,\Delta b \cos g_2 \sin g_2 + \Delta c \sin^2 g_2 \qquad (2.85)$$

ρ_1 and ρ_2 are the principal radii of the difference surface of gear and pinion surface, the lengths of the semi-axes of the contact ellipse in the tangent plane are:

$$l_1 = \frac{\sqrt{0.0005\,\frac{1}{\rho_1}}}{\frac{1}{\rho_1}}$$

$$l_2 = \frac{\sqrt{0.0005\,\frac{1}{\rho_2}}}{\frac{1}{\rho_2}} \qquad (2.86)$$

2.3.2.3 Velocity of Contact Point

Consider that the gear surface is stationary. During a small unit time, the contact point on pinion moves from P to P' with velocity V_s due to rotation of the pinion. During this same time interval, the point of contact moves on the pinion surface to P" with a velocity $\bar{v}$ (Fig. 2-25), the velocity of contact point is the sum of these two parts.

$$\bar{u} = \bar{V}_s + \bar{v} \qquad (2.87)$$

The pinion point velocity relative to the gear for unit pinion rotational velocity is

$$\bar{V}_{sl} = m_i(\bar{R}_{gl} \times \bar{g}) + (\bar{R}_{pl} \times \bar{p}) \tag{2.88}$$

Transforming this vector into the common tangent plane

$$\bar{V}_s = \bar{V}_{sl}(-, \bar{t}_{gt}, \bar{n}_{gl})^T \tag{2.89}$$

The angular velocity of the pinion body relative to the gear is

$$\bar{\omega}_1 = -\bar{p} - m_i \bar{g} \tag{2.90}$$

Transforming this vector into the tangent plane,

$$\bar{\omega} = \bar{\omega}_1(-, \bar{t}_{gt}, \bar{n}_{gl})^T \tag{2.91}$$

The surface coefficients of gear and pinion in this tangent plane are

$$(s_g) = \begin{pmatrix} a_{sg} & b_{sg} \\ b_{sg} & c_{sg} \end{pmatrix}$$

$$(s_p) = \begin{pmatrix} a_{spg} & b_{spg} \\ b_{spg} & c_{spg} \end{pmatrix} \tag{2.92}$$

Since p" is to be a point of contact, the rate of change of the normals of the gear surface and the pinion must be the same:

$$\frac{d\bar{n}}{dt} = -\bar{u}(s_g) \qquad \text{for the gear}$$

$$= -\bar{v}(s_p) + \bar{\omega} \times \bar{n} \qquad \text{for the pinion}$$

where $\bar{\omega} \times \bar{n}$ is due to the rotation of the pinion surface, and $-\bar{v}(s_p)$ is due to curvature of pinion surface. Hence,

$$-\bar{u}(s_g) = -(\bar{u} - \bar{V}_s)\ (s_p) + \bar{\omega} \times \bar{n}$$

$$\bar{u}[(s_g) - (s_p)] = \bar{\omega} \times \bar{n} + \bar{V}_s(s_p) \qquad (2.93)$$

$$\bar{u}(\Delta s) = \bar{\omega} \times \bar{n} + \bar{V}_s(s_p)$$

$$\bar{u} = [\bar{\omega} \times \bar{n} + \bar{V}_s(s_p)]\ (\Delta s)^{-1}$$

2.4 Results and Discussion

One typical set of spiral gears currently being tested at NASA Lewis Research Center was used to illustrate the numerical calculations. The machine settings, which are provided by Gleason Works, are shown in Appendix A. The points on the tooth surface were obtained by procedures described in Section 2.2. The contact condition was determined by the method shown in Section 2.3. A series of solutions were obtained to simulate the spiral bevel gears subjected to a range of operating conditions, and results are presented here. In order to obtain a unified view, all the curves are plotted in the axial plane.

2.4.1 Tooth Profile

The methods in Section 2.2, which use actual cutting motions of the gear cutting tools, result in an exact description of the tooth-forms as functions of spiral angle, blade-edge radius, etc.

A typical tooth profile for the gear shown in Fig. 2-26 was plotted in Fig. 2-27. For the purpose of applying FEM in gear design, a typical finite element model for a single gear tooth was shown in Fig. 2-28.

2.4.2 Contact Pattern

The spiral bevel gears are relieved both profilewise and lengthwise, so that there is only a single contact point in the center of the tooth. This combined mismatch permits the gear pair to tolerate displacements under load and assembly errors. Theoretical point contact is, of course, only an imaginary concept. Under even light loads, tooth surfaces

compress and deflect to cause surface contact. This surface contact area is roughly elliptical. The sum of those elliptical contact areas along the path of contact is called "Tooth Bearing." Correctly made teeth will show a tooth bearing centrally located on the tooth surface, when the gears are in their standard relative running positions. The amount of lengthwise mismatch is readily observed by the length of the tooth bearing. Profile mismatch is not observed as readily owing to the fact that the tooth height is relatively small; nevertheless, the existence of profile mismatch is evidenced by the lack of any heavy concentration of bearing at the tips of the teeth.

The results illustrated here were obtained by analyzing the effects of running position errors on the path of contact. The errors discussed here include pinion apex withdraw (X_{pr}), gear apex withdraw (X_{gr}), running shaft angle (Σ_r) and running offset (E_r). Their effects are calculated by changing the value of a single term while keeping the others unchanged, and these results are shown from Fig. 2-29 to Fig. 2-33. The path of contact moves to the toe as the pinion apex withdraw increases and moves to the heel as it decreases. The shape of the path of contact remains the same, but is inclined more as it approaches both sides. The gear apex withdraw will produce the same effect, but in the opposite direction. As X_{gr} increases, the path of contact moves to the heel, and the opposite occurs as X_{gr} decreases. Both of these have as their chief effect a pressure angle error; the tooth contact will move toward the tooth tips on the gear tooth and toward the tooth flanks on the pinion. When the shaft angle becomes larger, the contact on both the gear and the pinion shifts to the toe. At the same time, the contact moves toward the tooth tips. The contact goes the opposite way when the

shaft angle decreases. This effect is expected. The principal effect of the offset is to tilt the tooth in its mating slot, so that the contact shifts to the toe on one side and to the heel on the other side.

Usually, the running position errors are introduced simultaneously; the results on the drive side are investigated for the sliding velocity and radii of the difference surface at the contact point with three separate sets of errors which result in the center contact, heel contact, and toe contact. The tooth bearing for these three contact cases is plotted respectively on the same graph. Assuming the combined Hertzian deformation to be 0.00025", which corresponds approximately to to the case of a pair of lightly loaded gears, and, using the curvatures of the contacting surfaces, the size and direction of the contact ellipse are determined. The larger the radius, the bigger the ellipse. The sliding velocity has also been plotted at selected points. See Fig. 2-34 and Fig. 2-35.

2.4.3 Motion Graphs

The rotation errors of the driven member against the driving member for the entire duration of contact for several adjacent meshing pairs were plotted. The corresponding velocity errors were shown in the same graph. Fig. 2-36 shows the curves on the drive side with a running position which results in a center contact. Fig. 2-37 shows the results on the coast side with the same running position. Figs. 2-38 and 2-39 illustrate the contact patterns for the motion curves shown in Figs. 2-36 and 2-37.

The velocity curves in those figures do not intersect; at the transfer points there is a sudden jump in the velocity with which the driving tooth strikes its mate. This value is, therefore, a measure of the impact occurring at each tooth mesh. As mismatch is increased, the impact increases in magnitude, resulting in noise and stress. It is therefore essential that mismatch be kept to the smallest value compatible with the adjustability to the running position errors. This concept of motion errors is only applied to the case under a very light load. The elastic deformation due to moderate load will smooth out these errors.

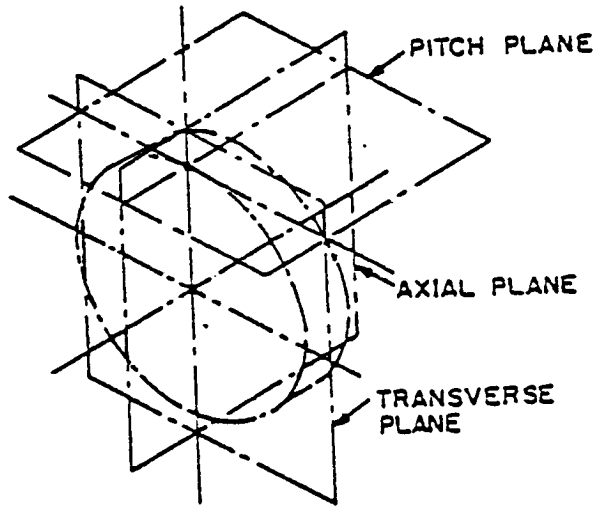

Fig. 2-1. Principal Reference Planes

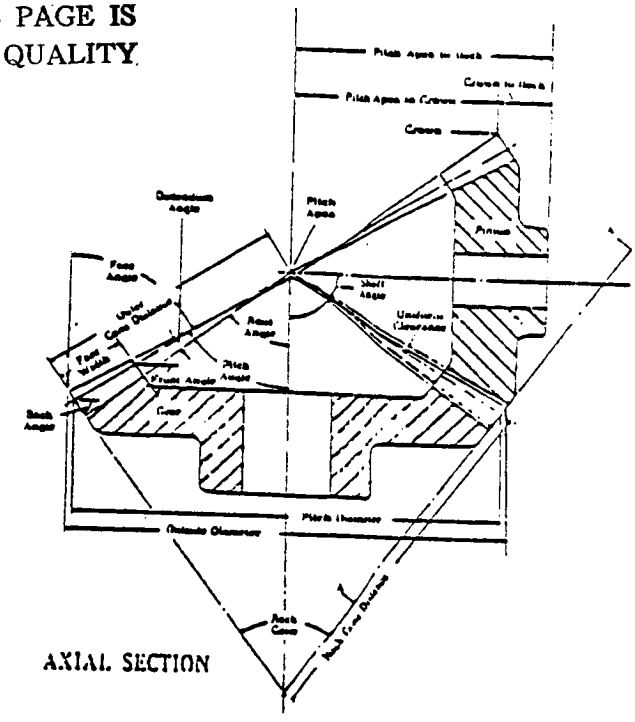

Fig. 2-2. Sectional View in The Axial Plane For A Pair of Spiral Bevel Gears

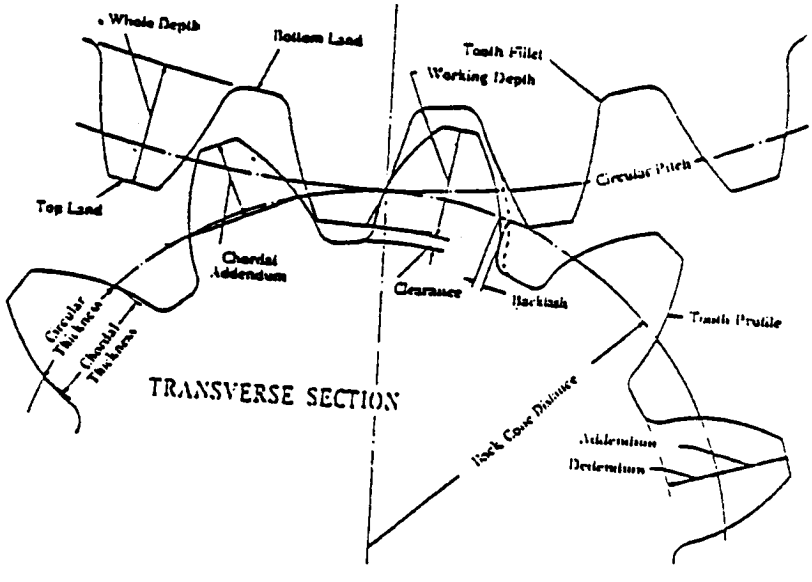

Fig. 2-3. Sectional View in The Transverse Plane For A Pair of Spiral Bevel Gears

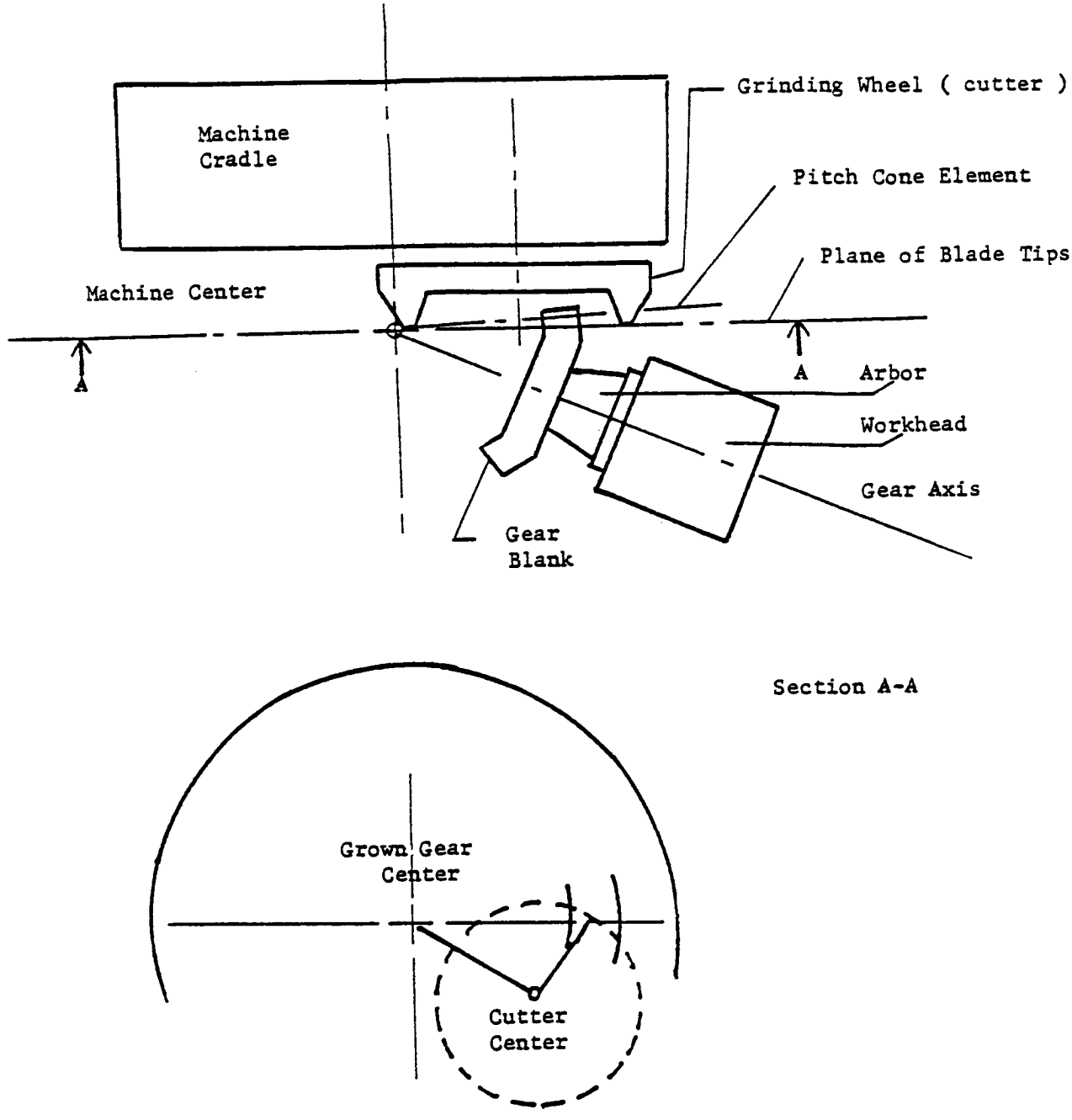

Fig. 2-4. Gleason Cutting Process For Spiral Bevel Gears

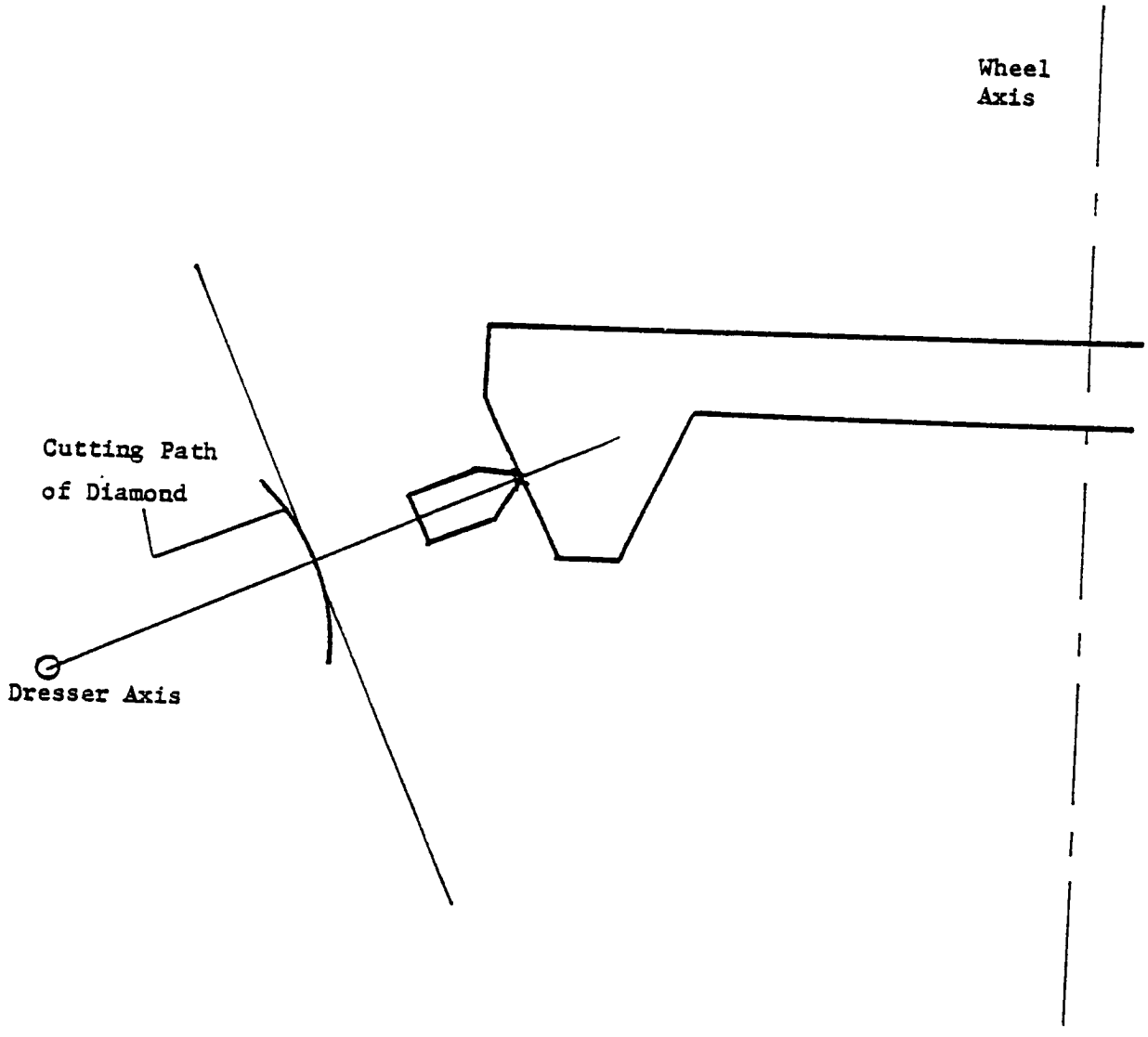

Fig. 2-5. Movement of the Dresser

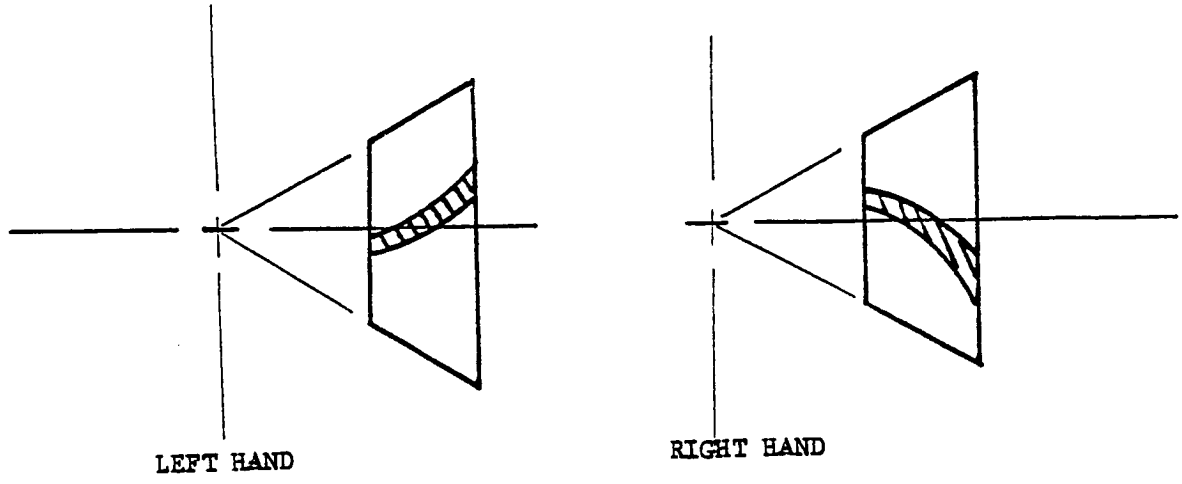

Fig. 2-6. Spiral Bevel Pinions

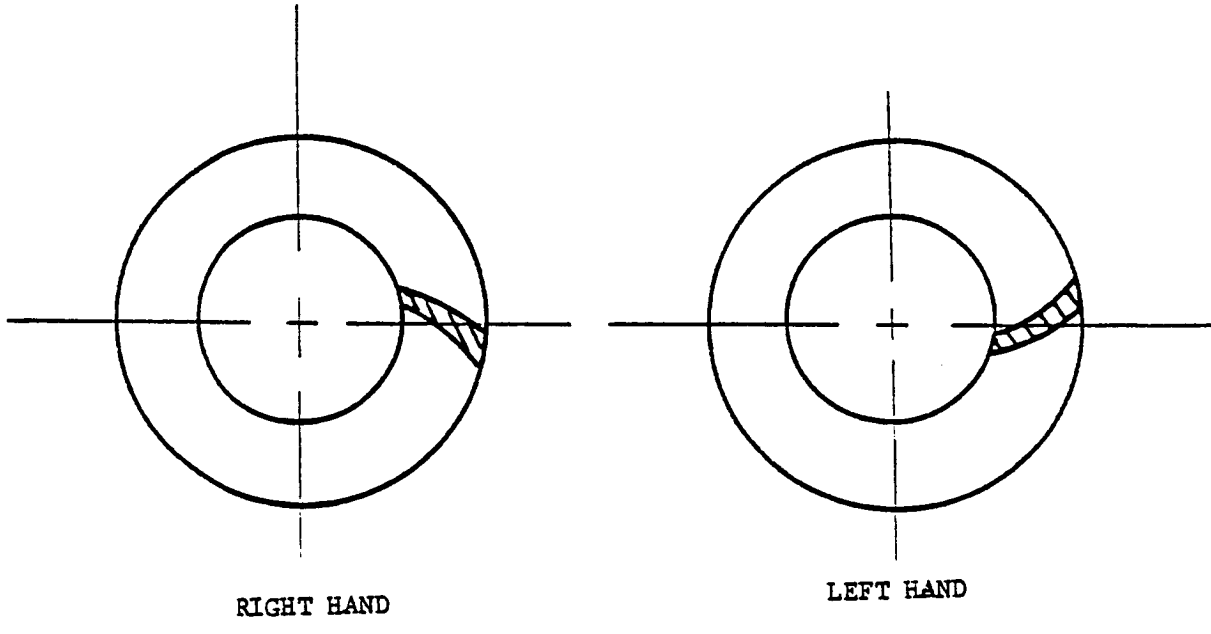

Fig. 2-7. Spiral Bevel Gears

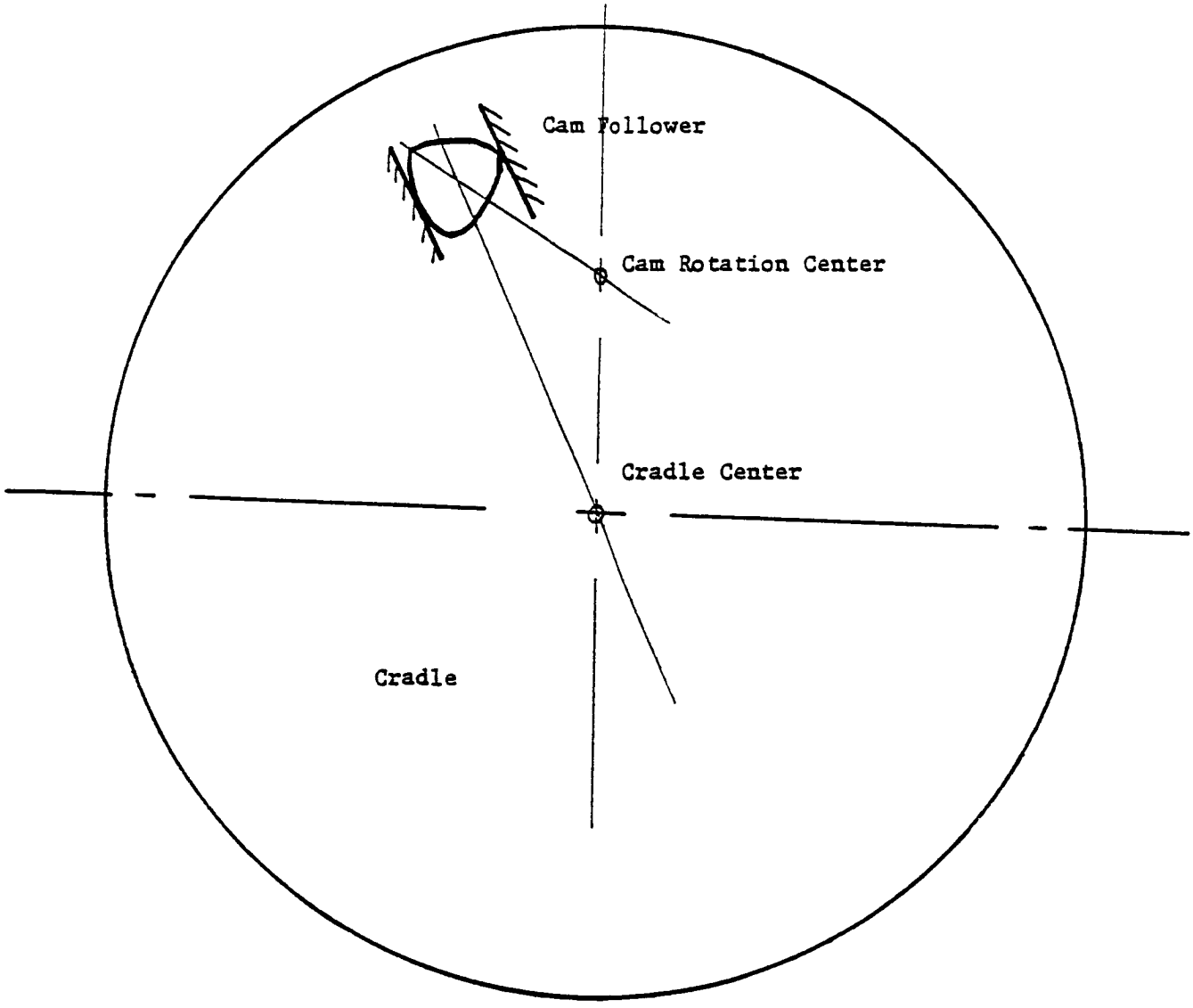

Fig. 2-8. Standard Cam Setting

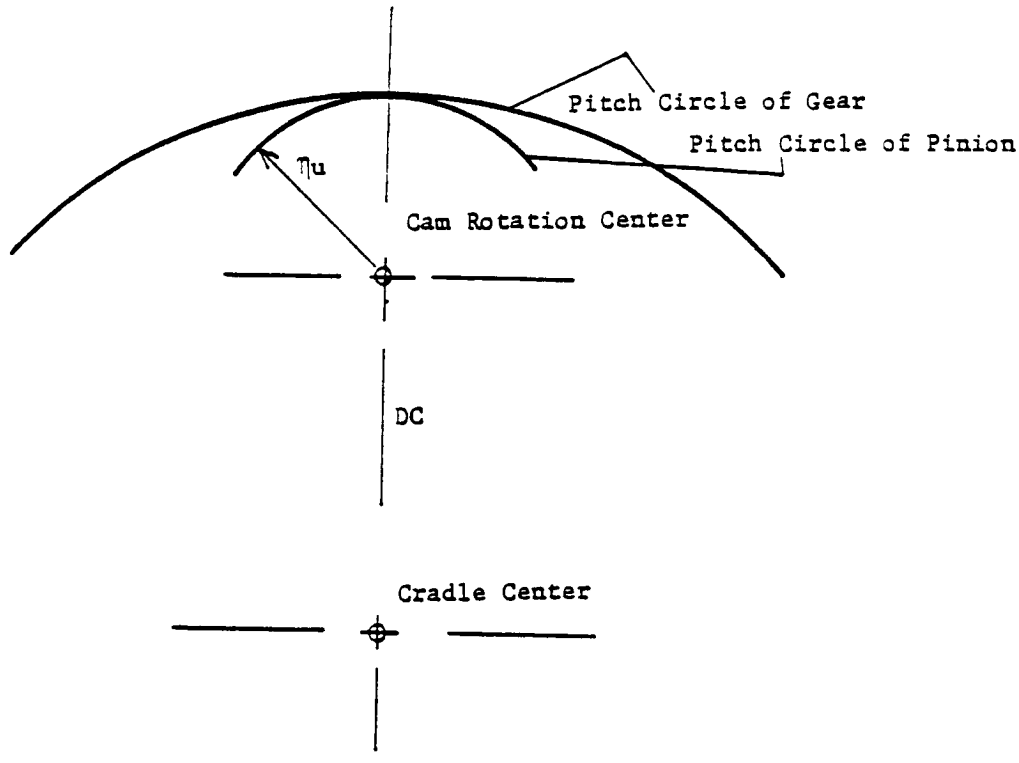

Fig. 2-9. The Movement of Standard Cam Setting.

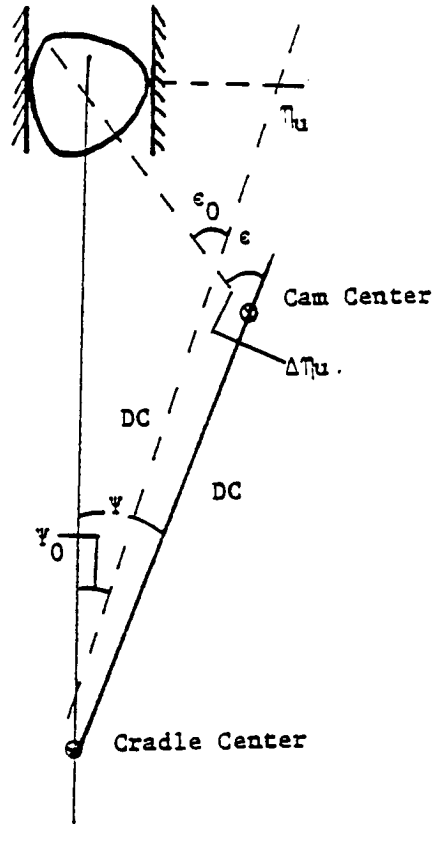

Fig. 2-10. The Movement of Cam With a Change in Cam Setting $\Delta\eta_\alpha$.

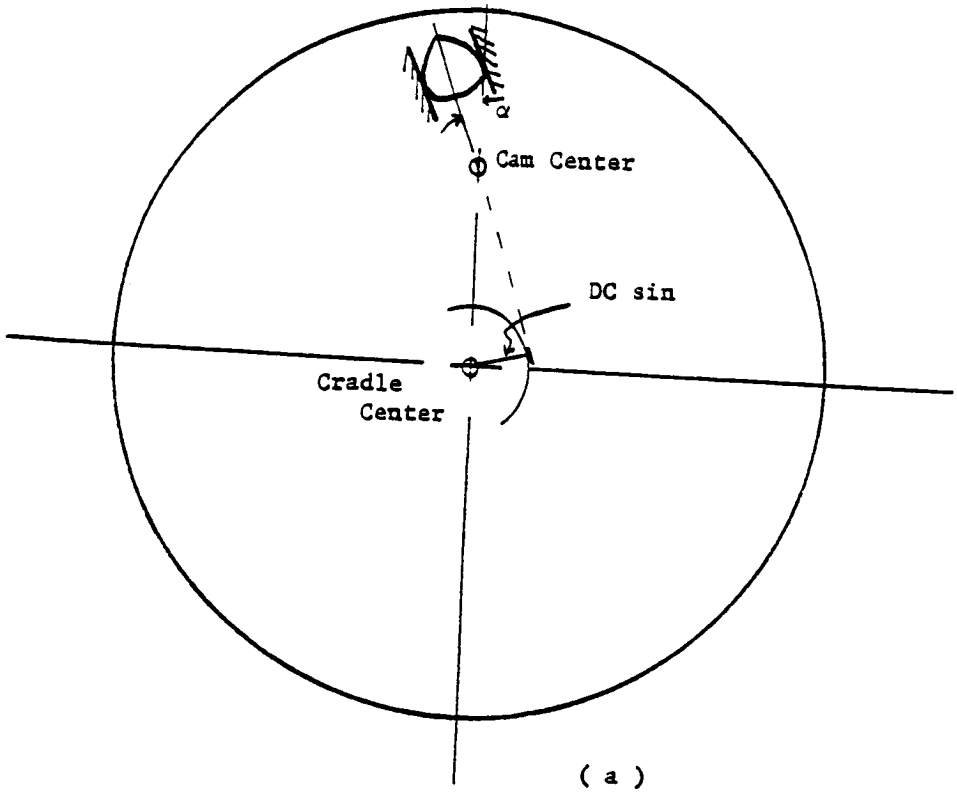

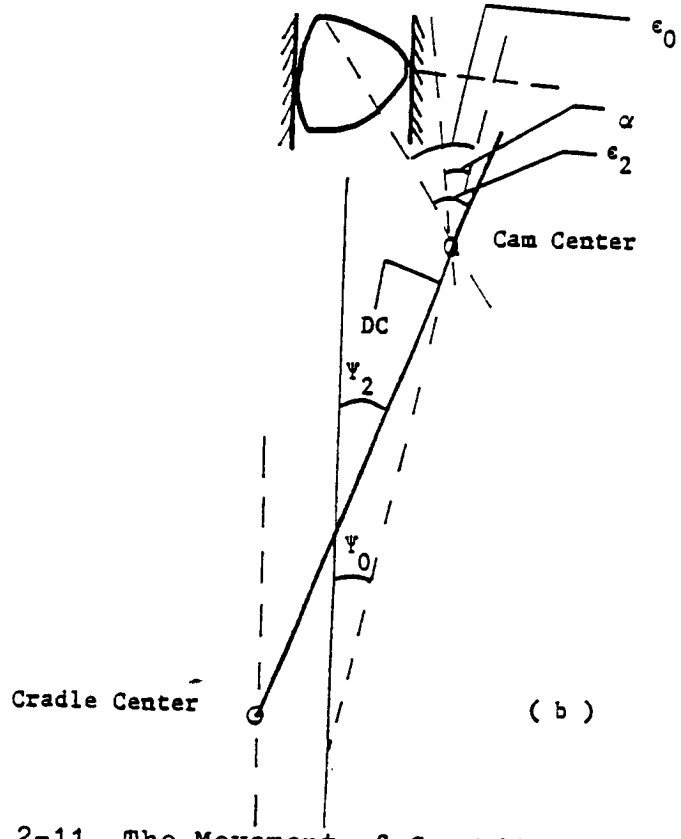

Fig. 2-11. The Movement of Cam With a Cam Guide Angle α

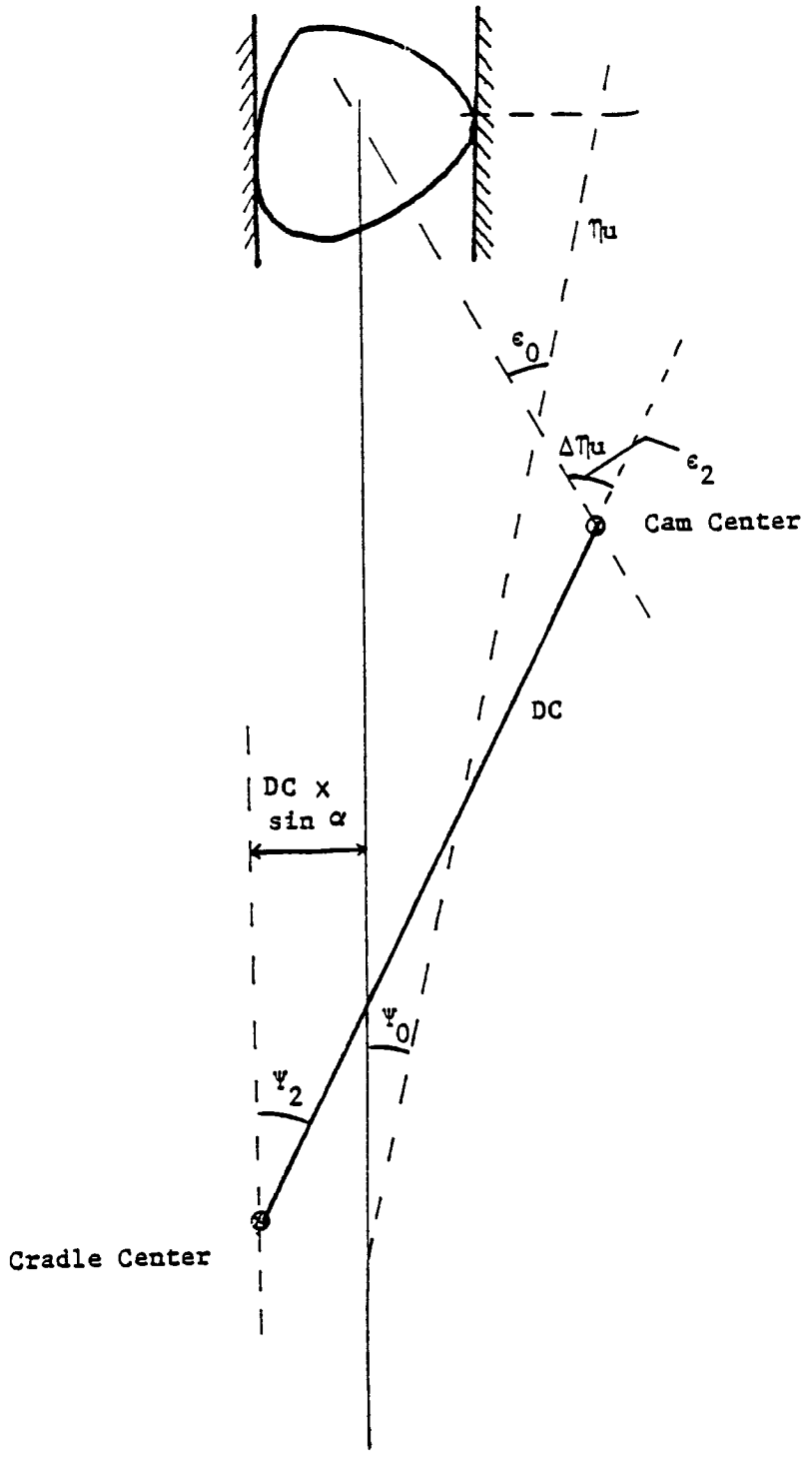

Fig. 2-12. The Movement of Cam With Change in Setting $\Delta\eta_u$ and Cam Guide Angle α

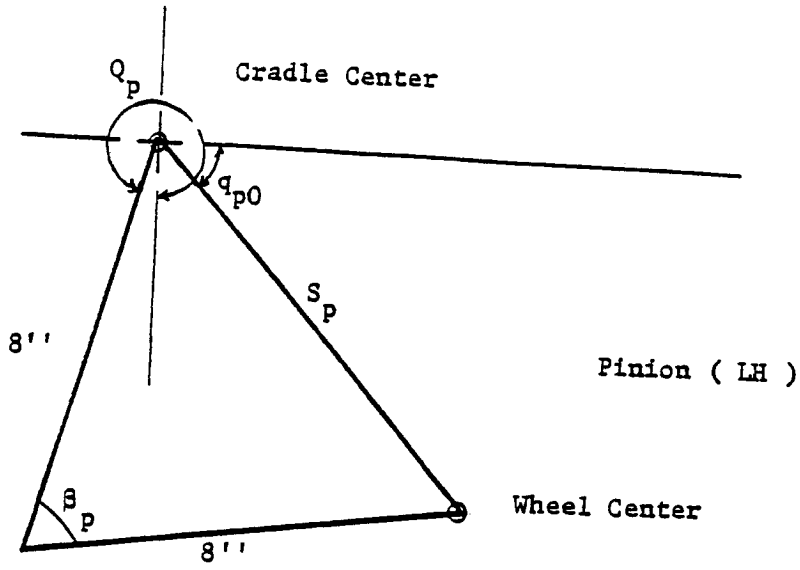

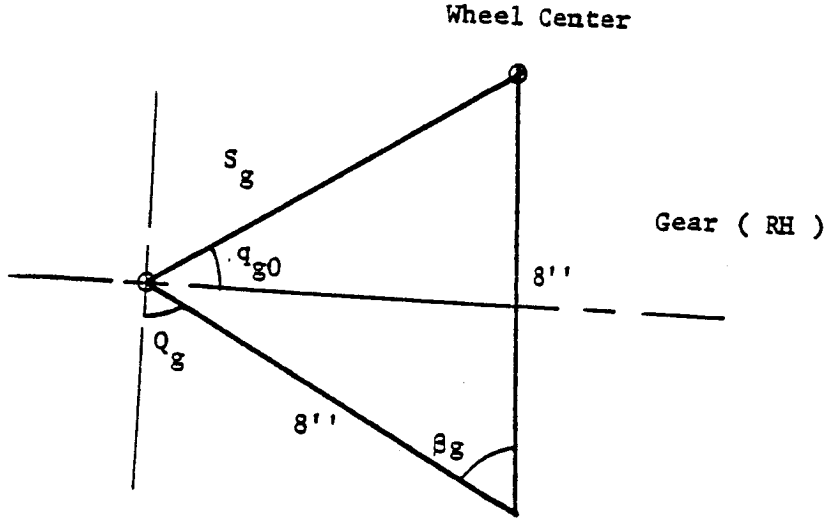

Fig. 2-13. Cradle Settings in the Spiral Bevel Gear Cutting Machine of the Gleason Works

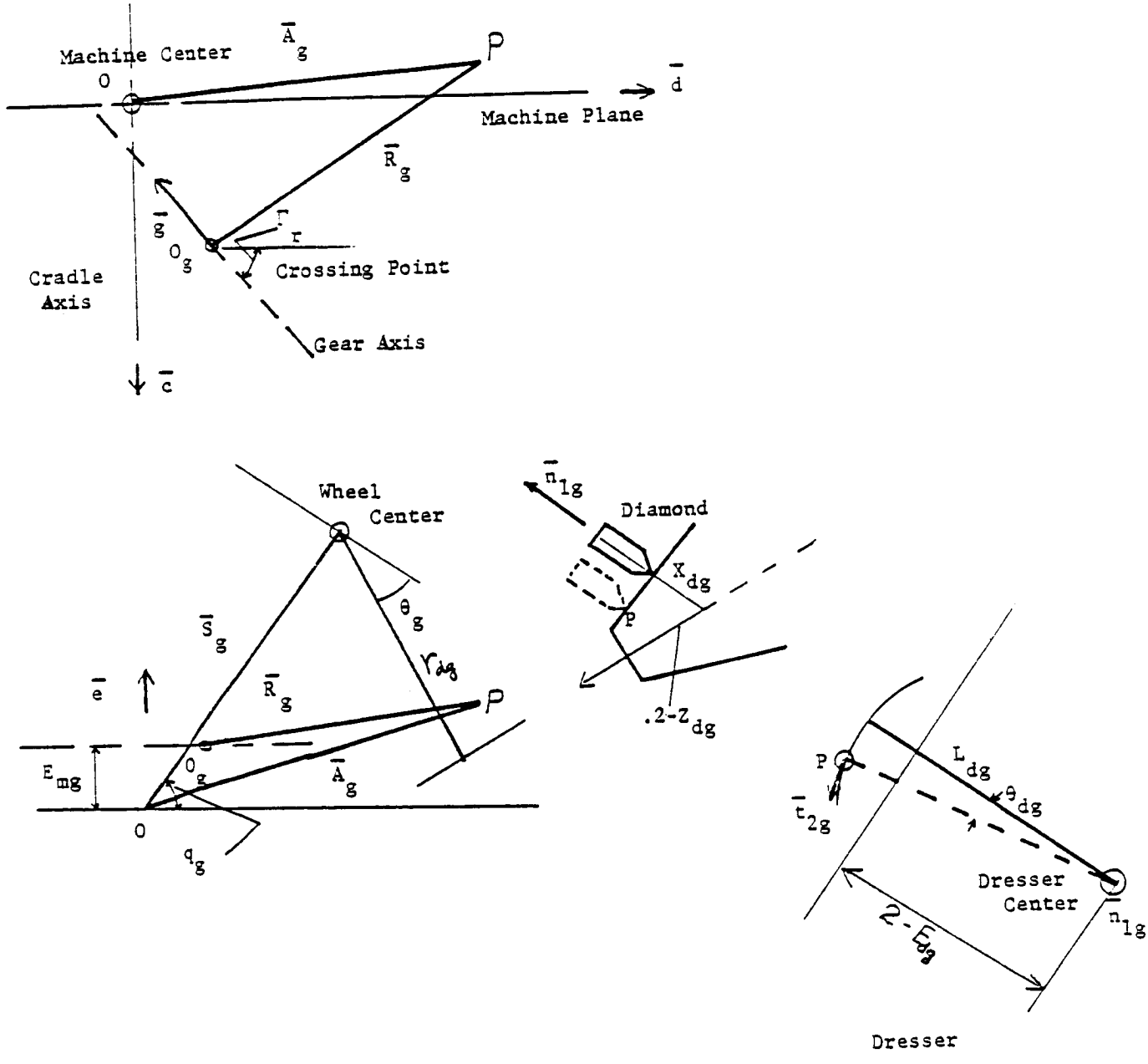

Fig. 2-14. Position Vectors in Machine Plane (Gear)

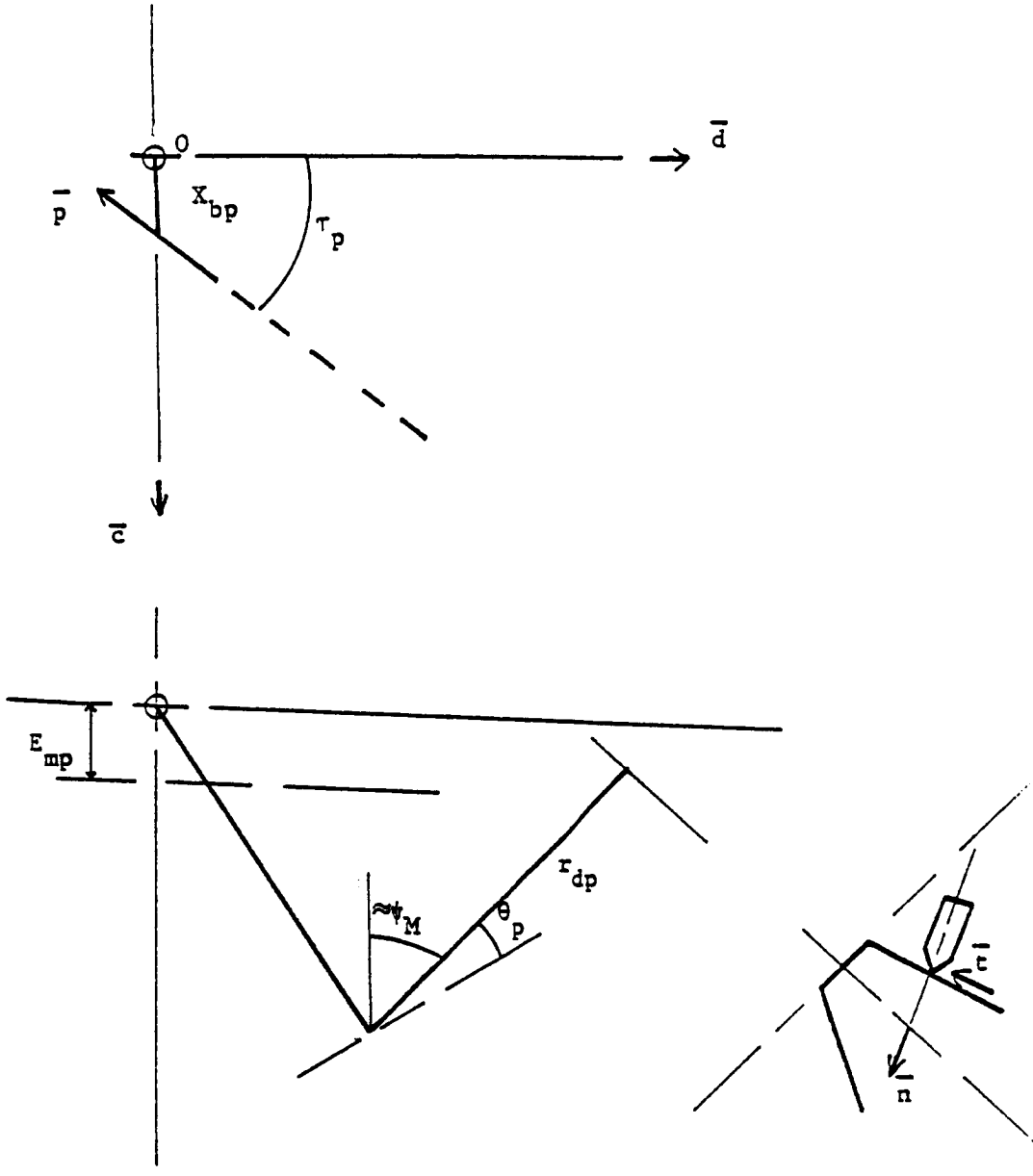

Fig. 2-15. Position Vectors in Machine Plane (Pinion)

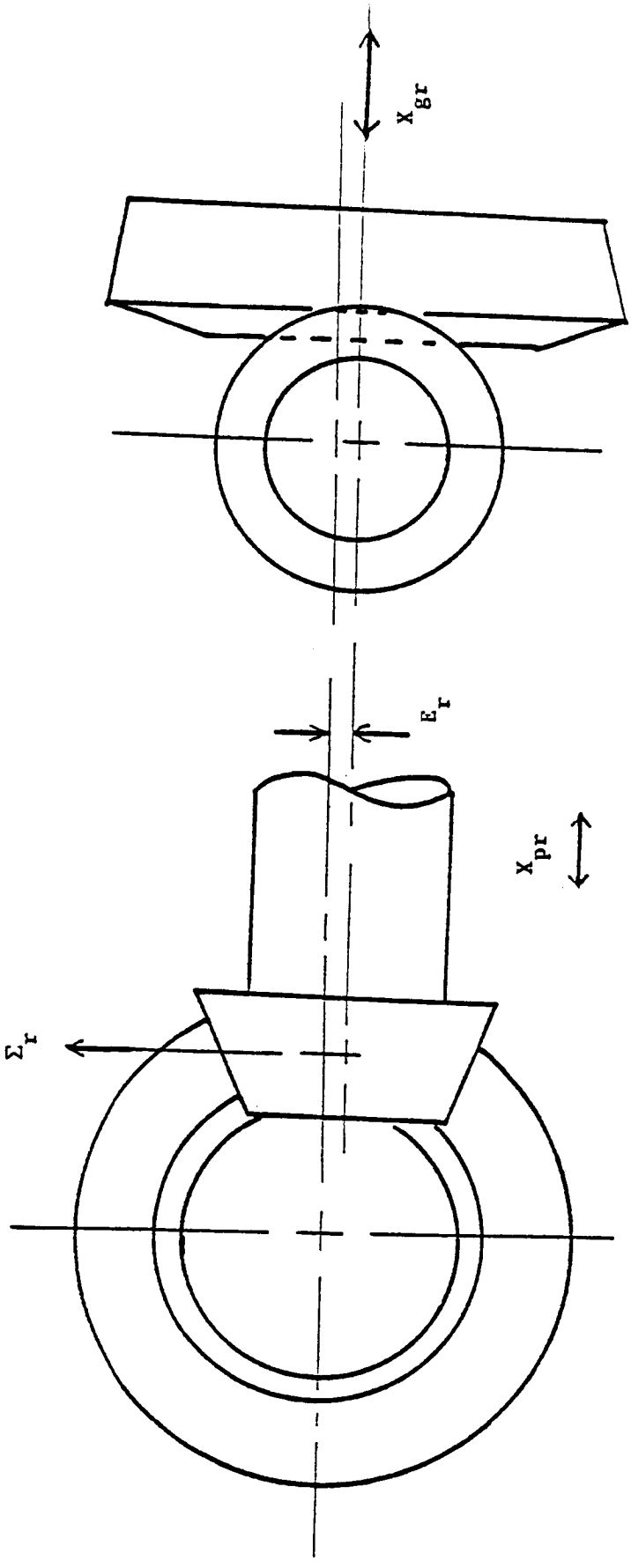

Fig. 2-16. Types of Misalignment in Bevel Gears

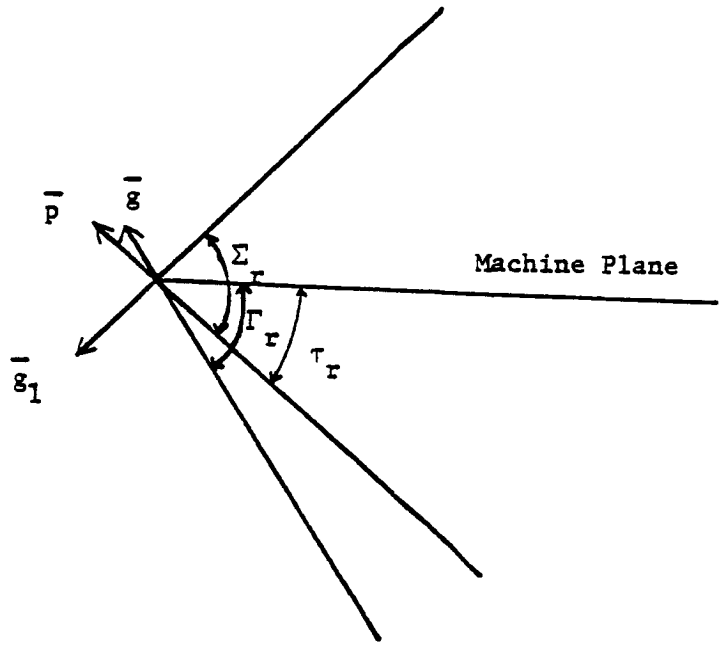

Fig. 2-17. Relation Vectors Between Running Position And Manufacturing Position

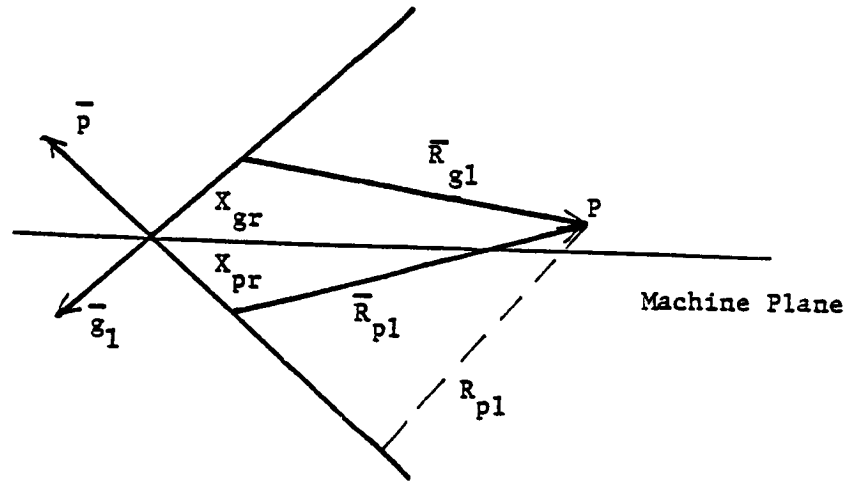

Fig. 2-18. Position Vectors in Running Position Relative to Pinion Axis

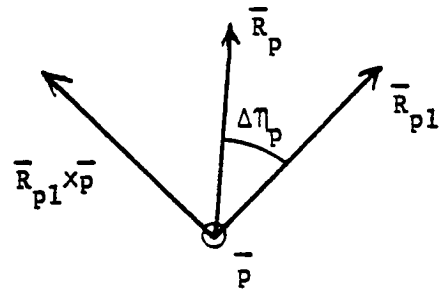

Fig. 2-19. The Angle Between $\bar{R}_{p1}$ and $\bar{R}_p$.

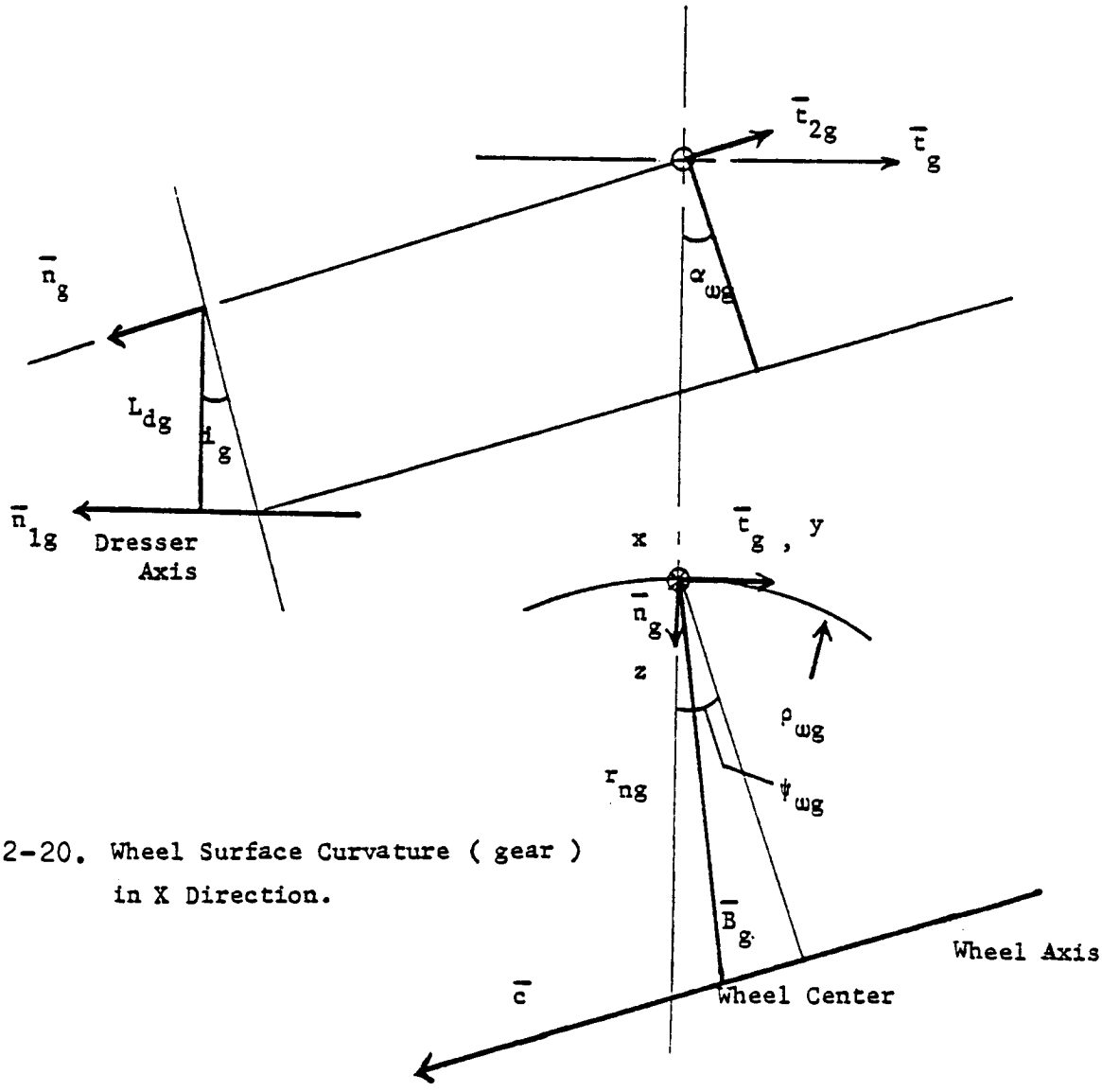

Fig. 2-20. Wheel Surface Curvature (gear) in X Direction.

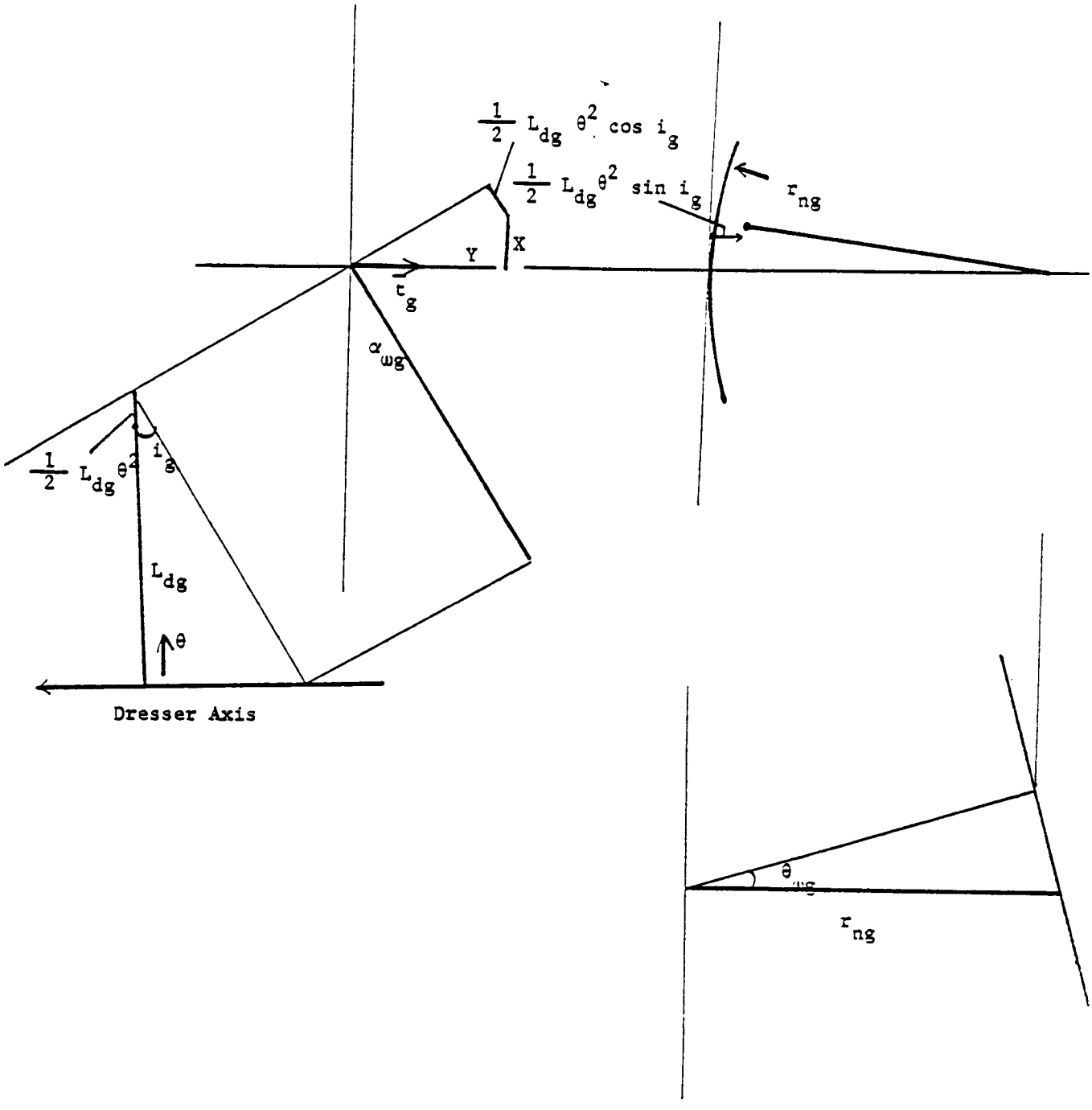

Fig. 2-21. Wheel Surface Curvature (Pinion) in Y Direction

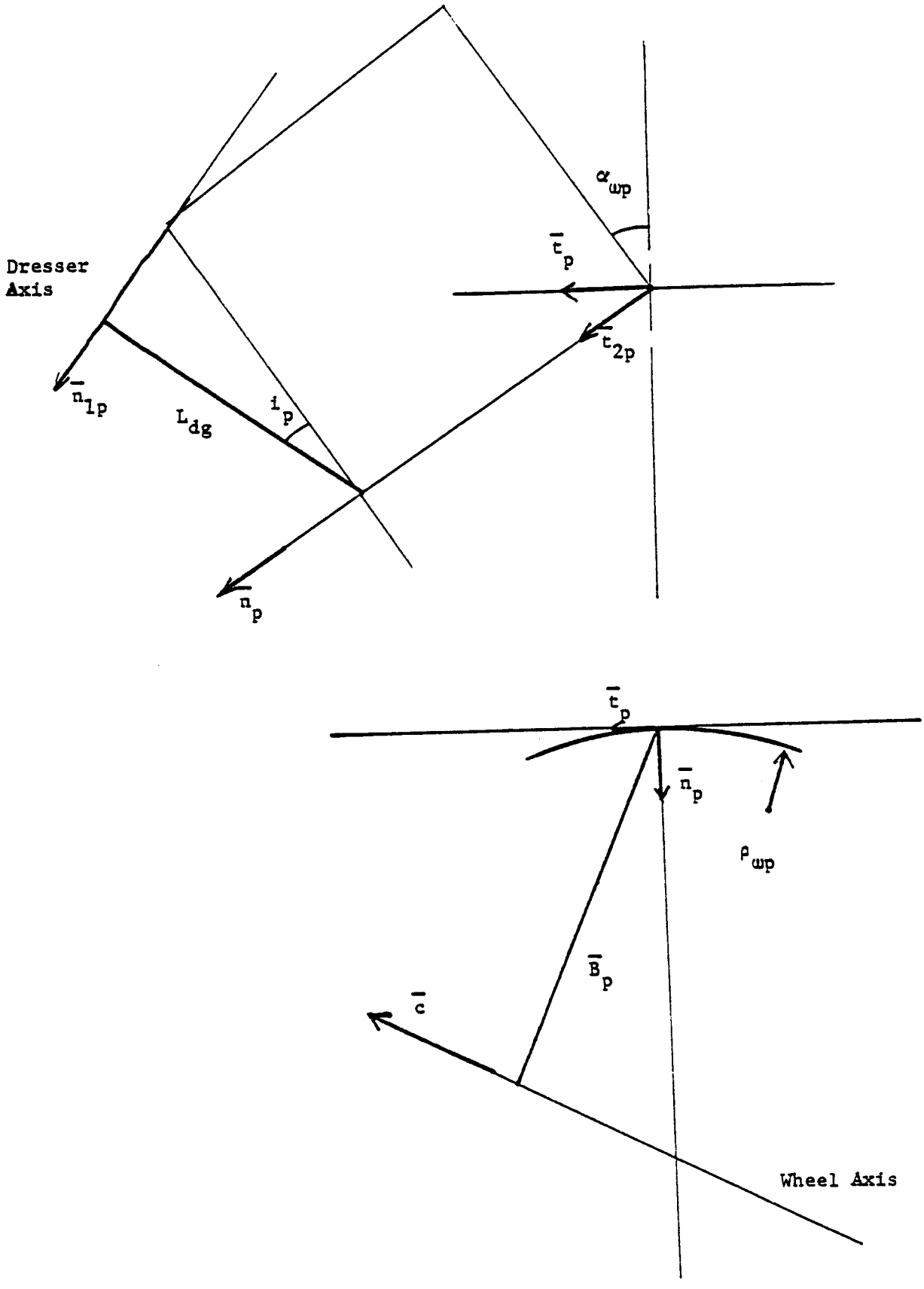

Fig. 2-22. Wheel Surface (Pinion)

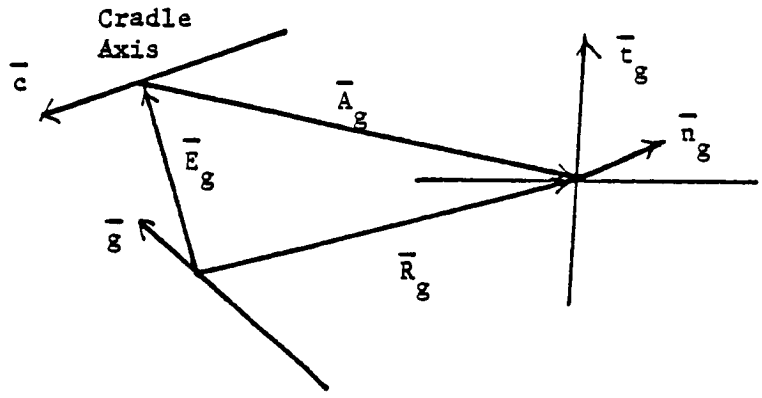

Fig. 2-23. Position Vectors (Considering Gear Stationary)

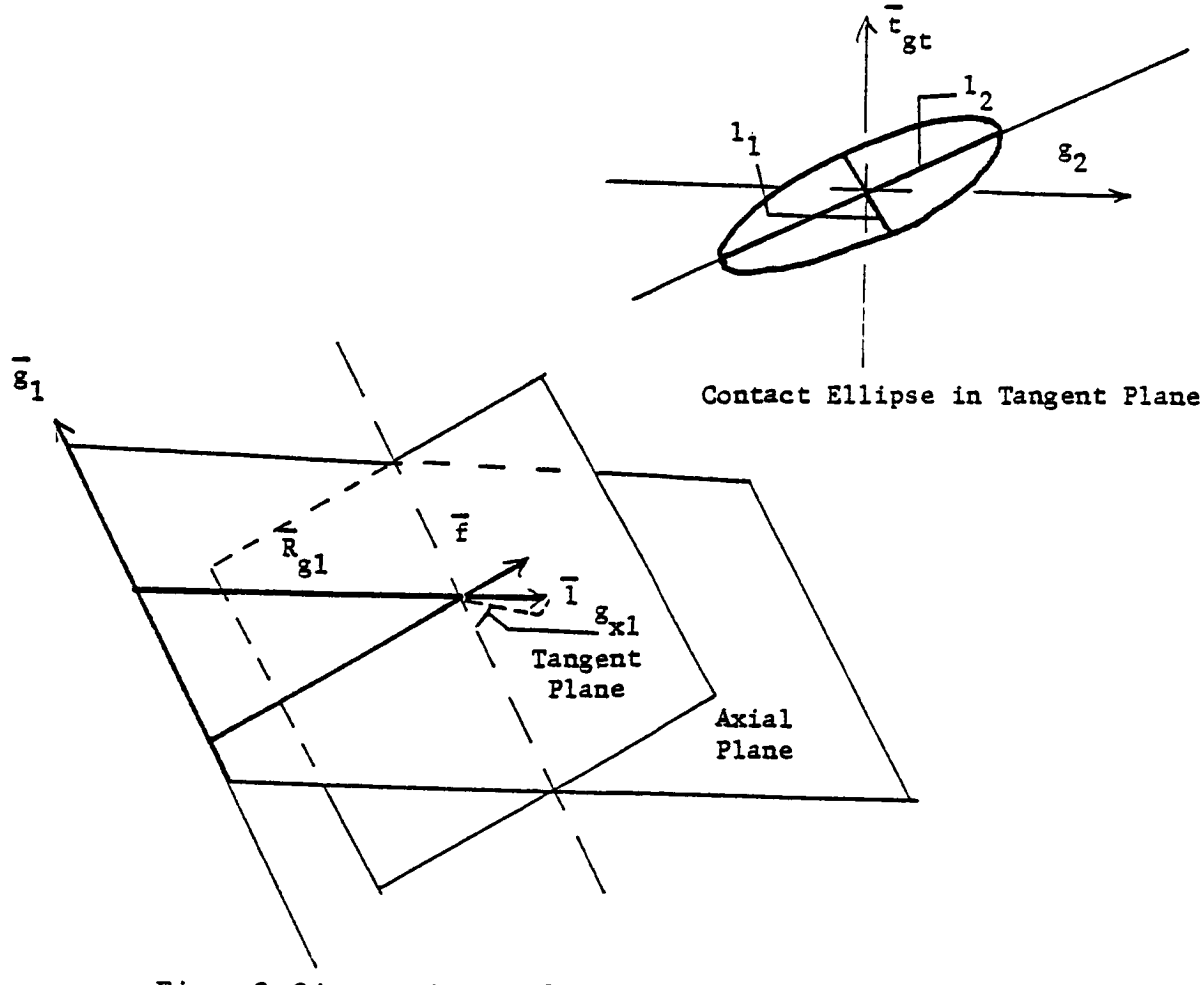

Fig. 2-24. Contact Ellipse Geometry

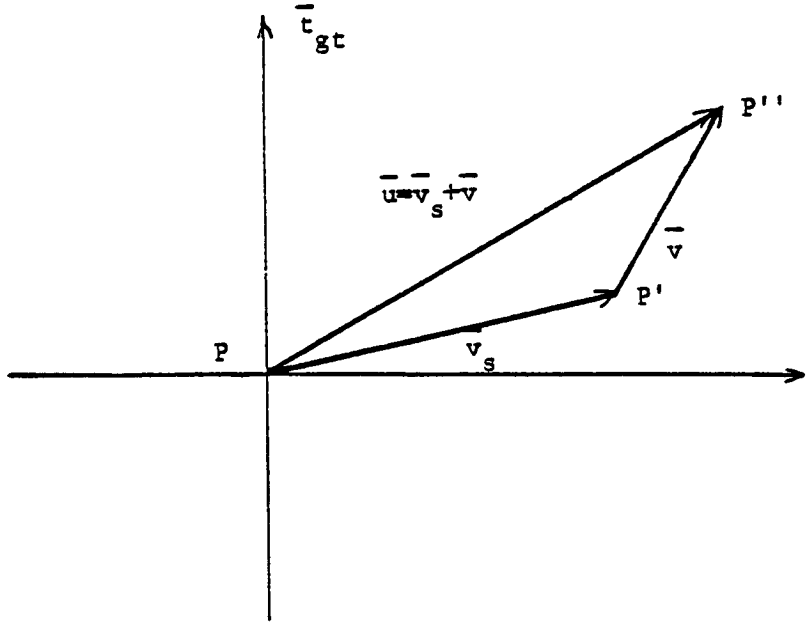

Fig. 2-25. Surface Velocity

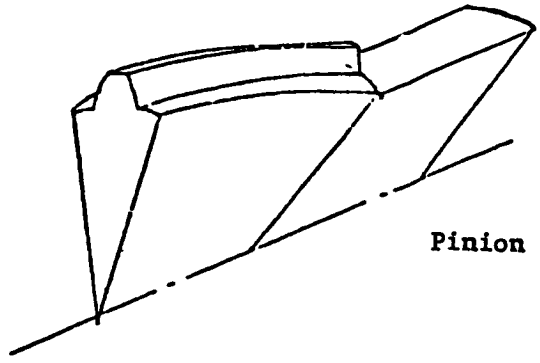

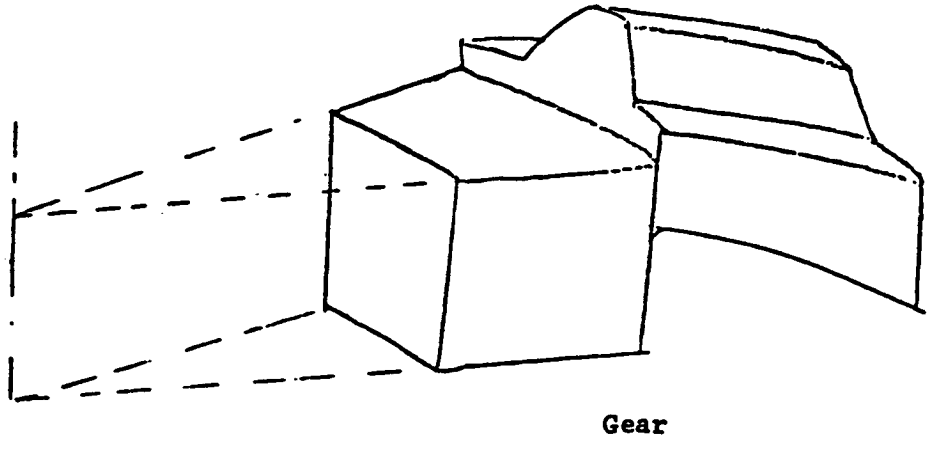

Fig. 2-26. Typical Tooth Profile

Fig. 2-27. Tooth Profile Plotted by Calculated Points

PTION: VW,X,Y,Z-VIEW POSITION DZ,M,N-DSPLY ZONES AZ,M,N-ADD ZONES
,TH-ROTATE HC-HRDCPY NB-NBR.ON/OFF EX-EXIT

EYE POSITION 81 2 114.4 500.0

HC

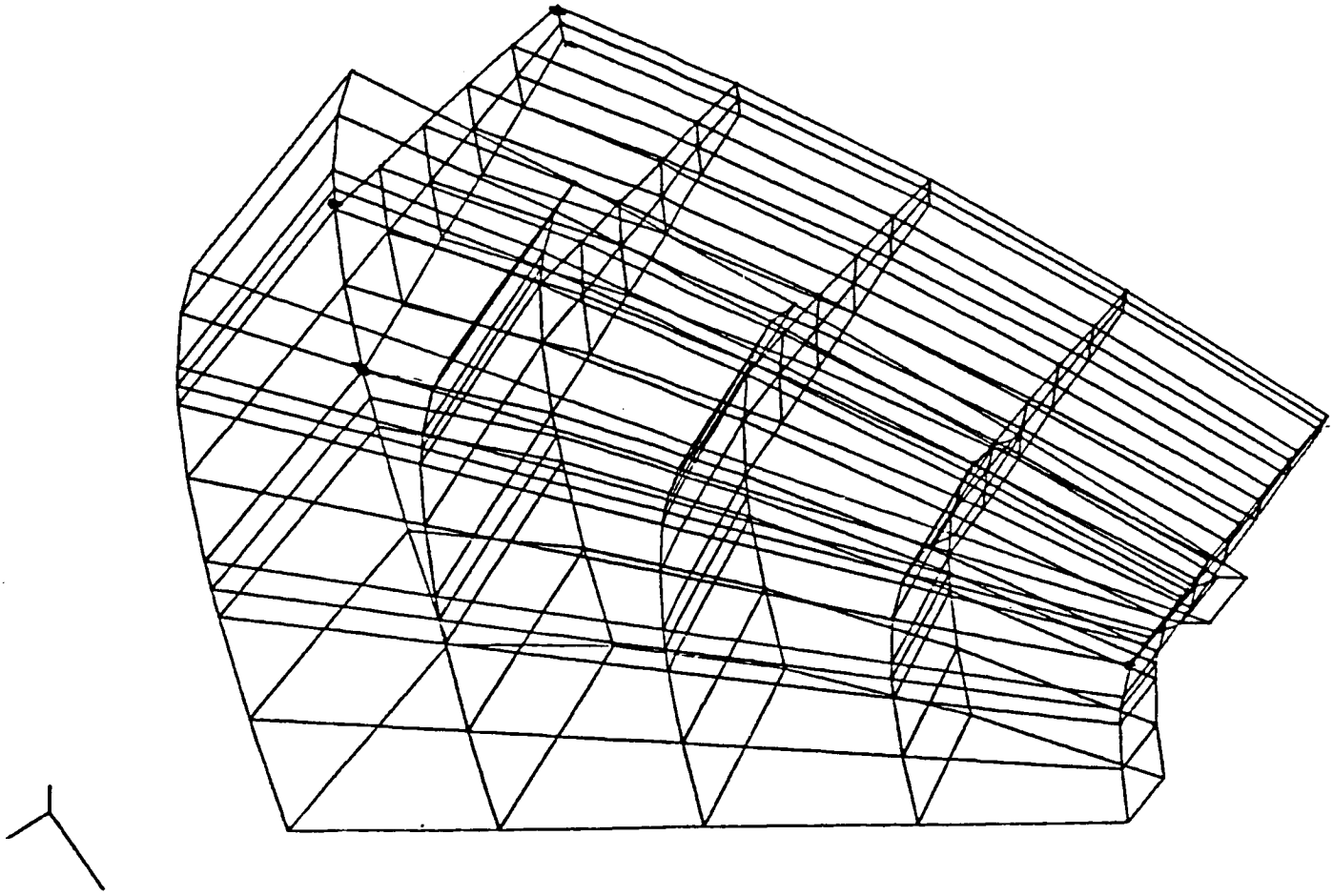

Fig. 2-28. The FEM Model For a Single Tooth

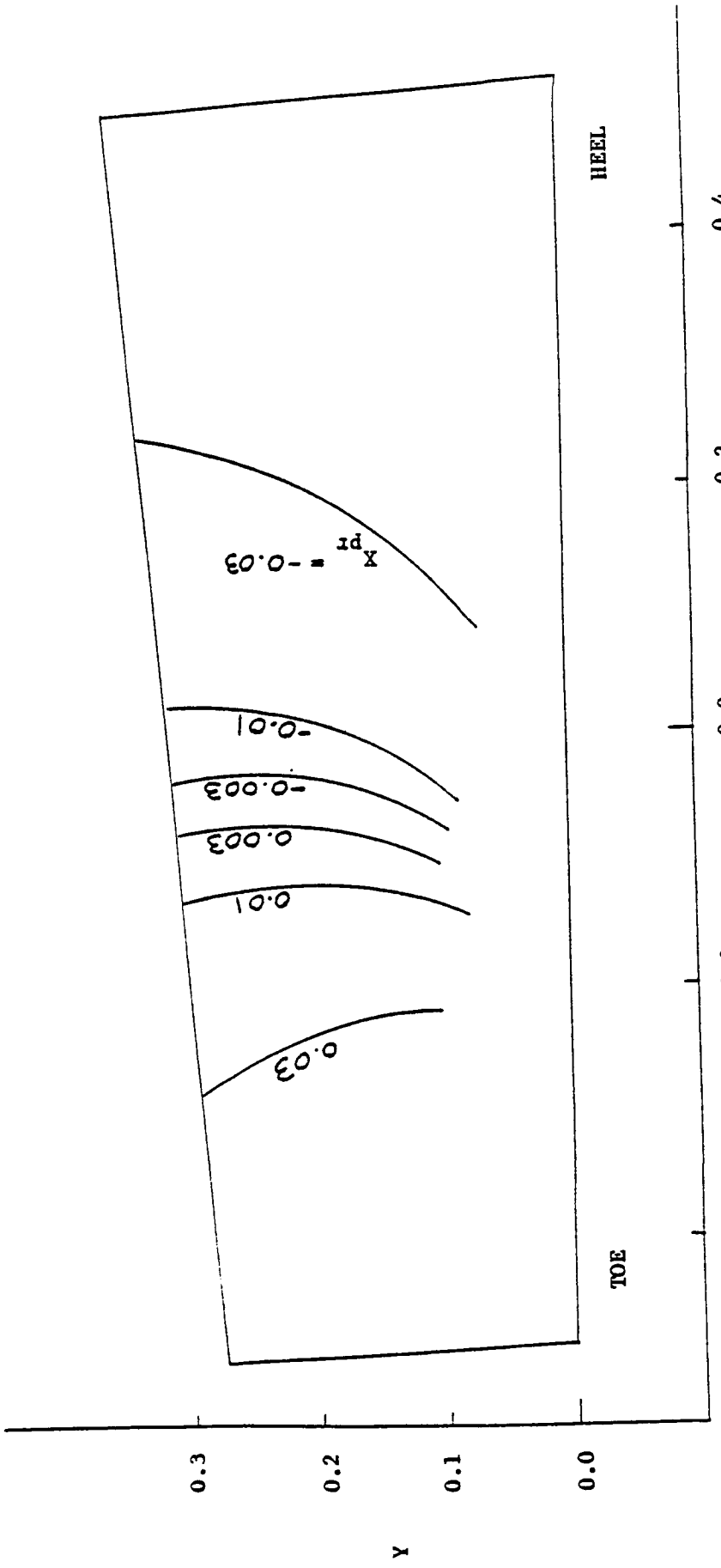

Fig. 2-29. The Path of Contact on Drive Side Affected by Pinion Apex Withdraw (in).

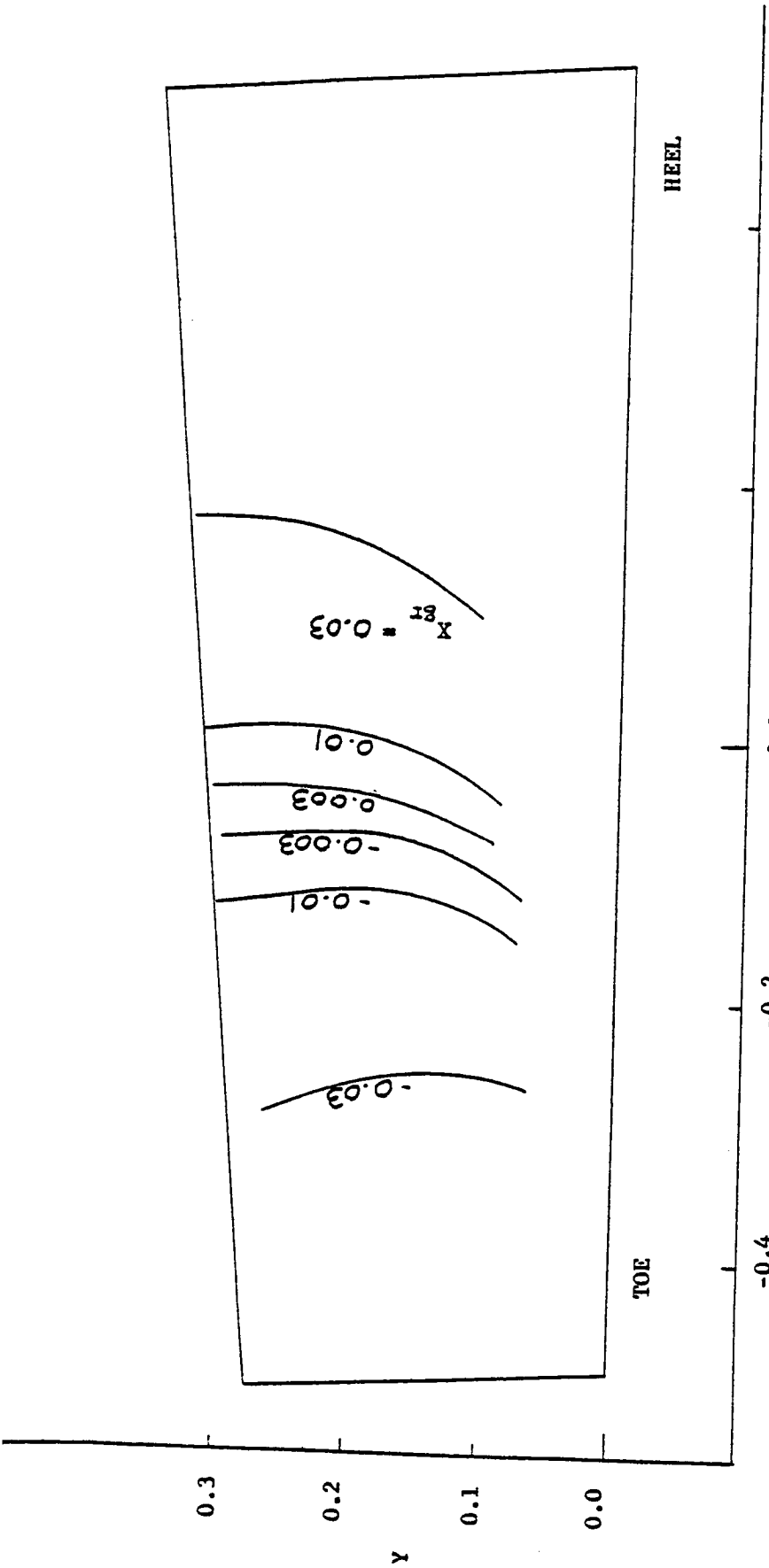

Fig. 2-30. The Path of Contact on Drive Side Affected by Gear Apex Withdraw (in).

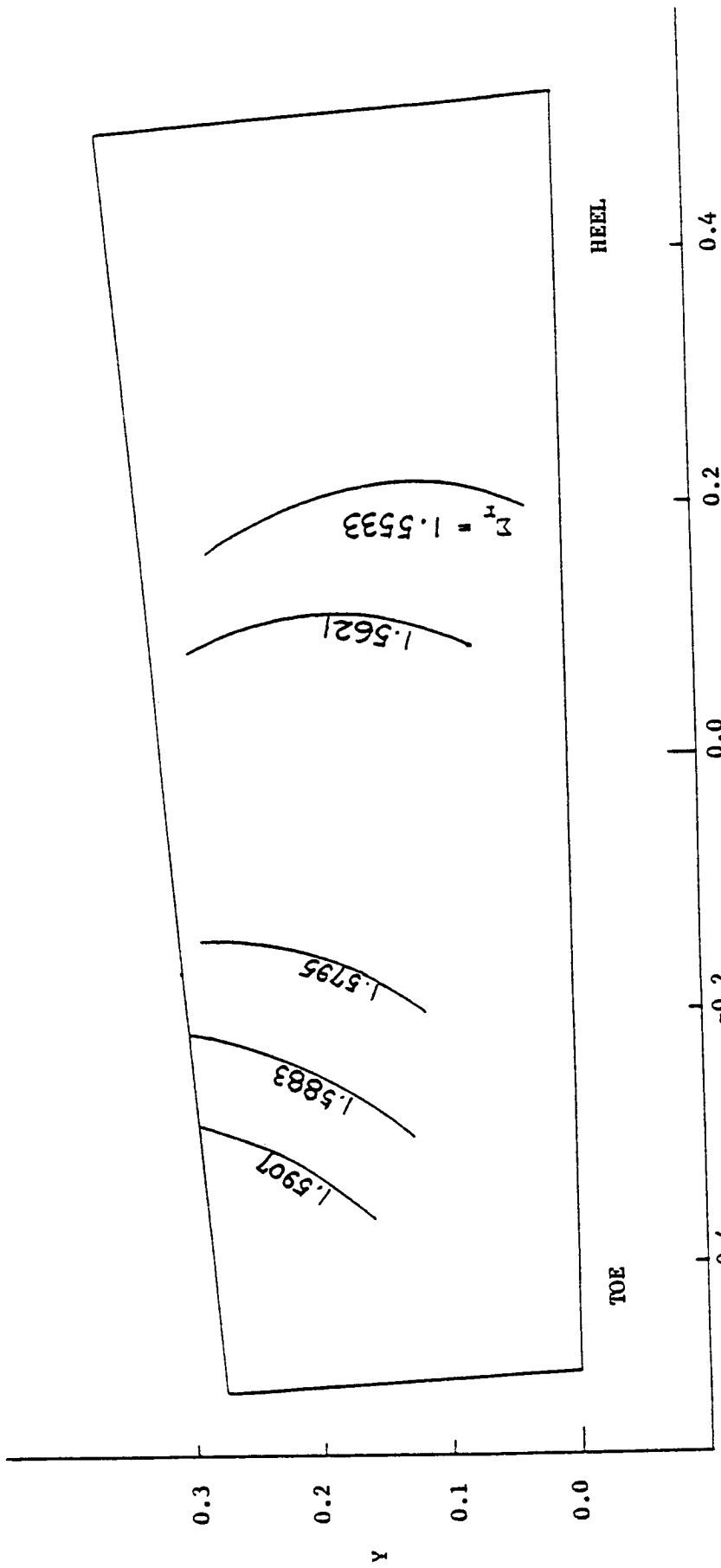

Fig. 2-31. The Path of Contact on Drive Side Affected by Shaft Angle Error

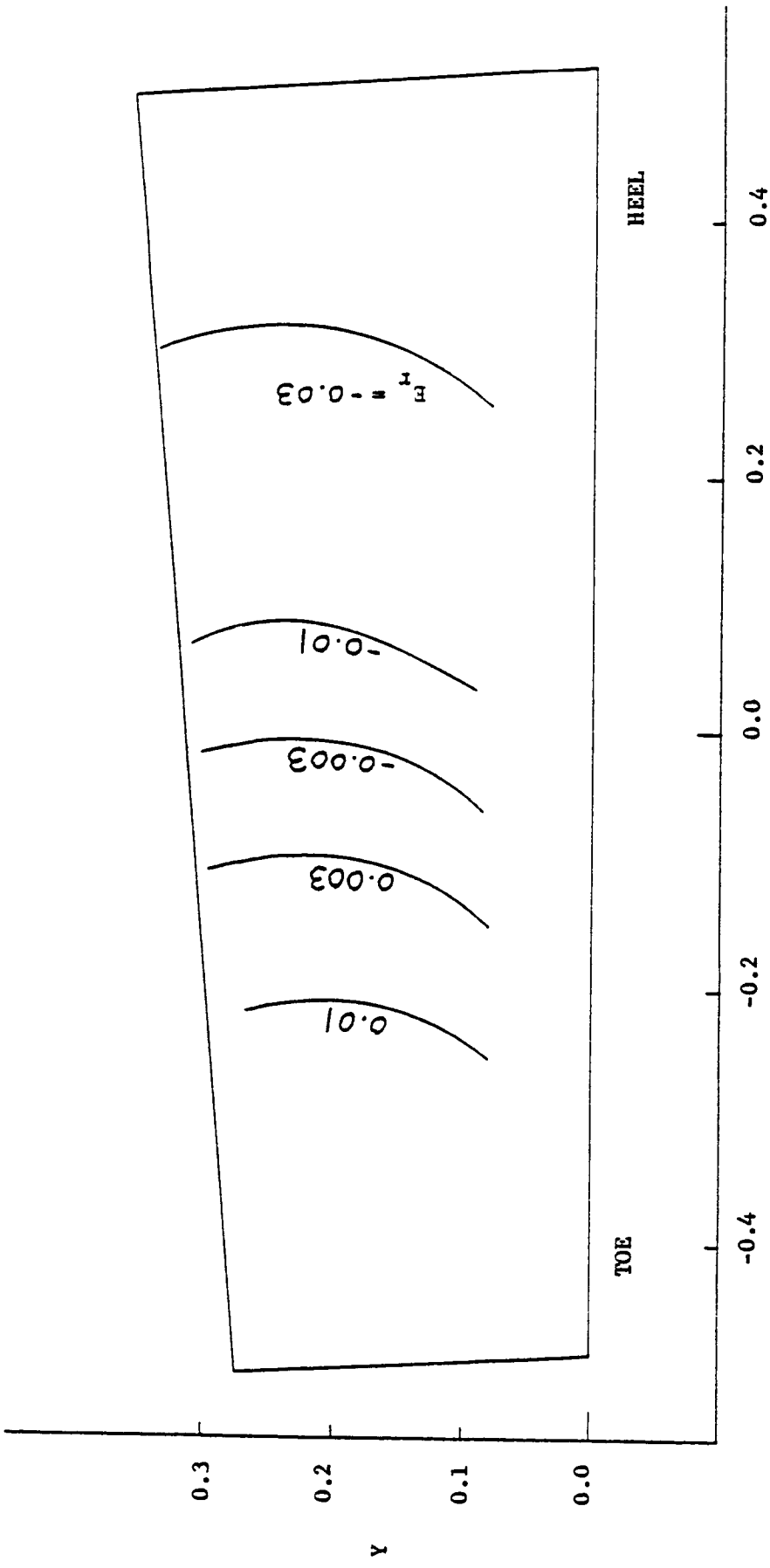

Fig. 2-32. The Path of Contact on Drive Side Affected By Offset (in)

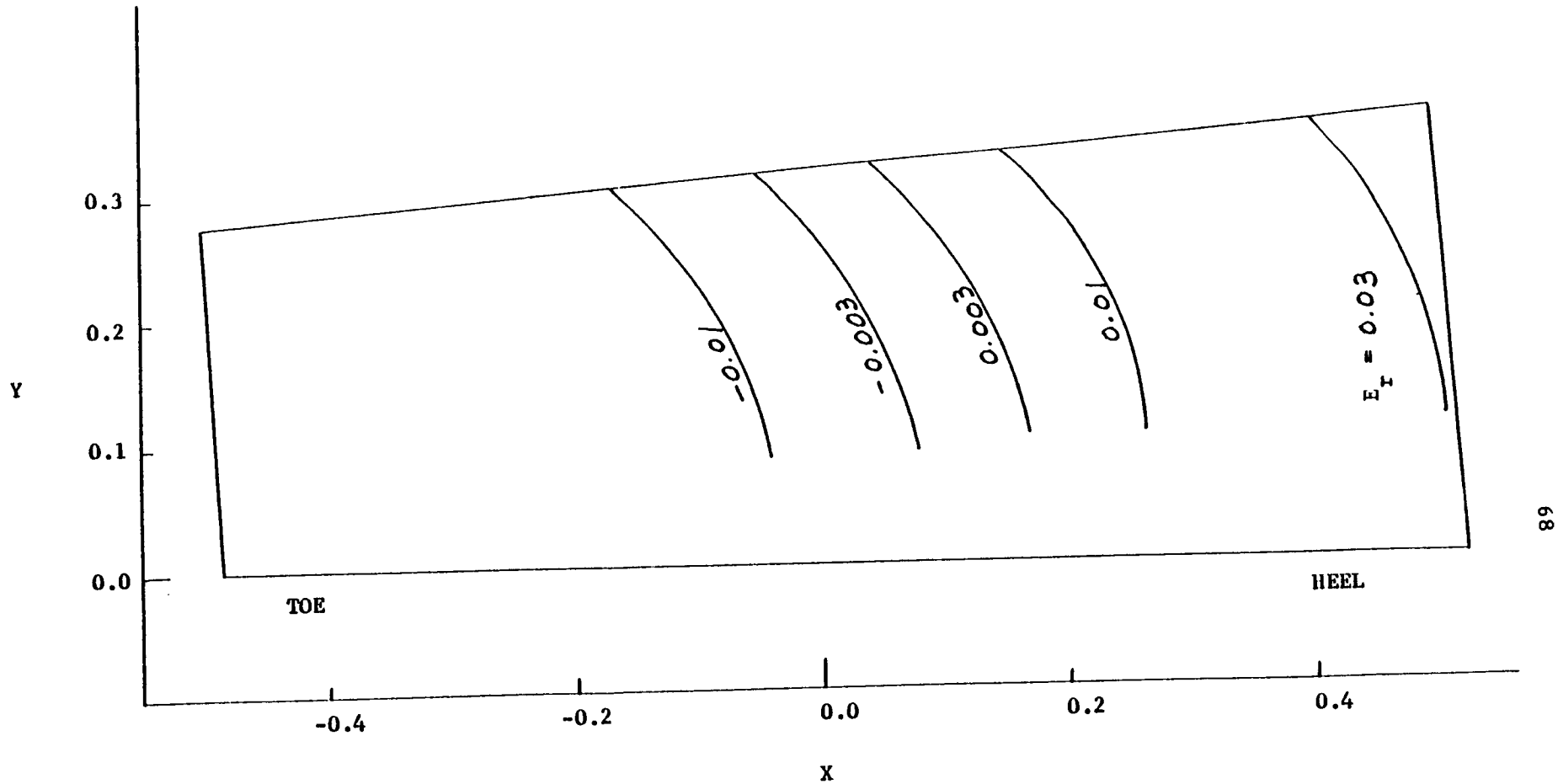

Fig. 2-33. The Path of Contact on Coast Side as Affected by Offset (in)

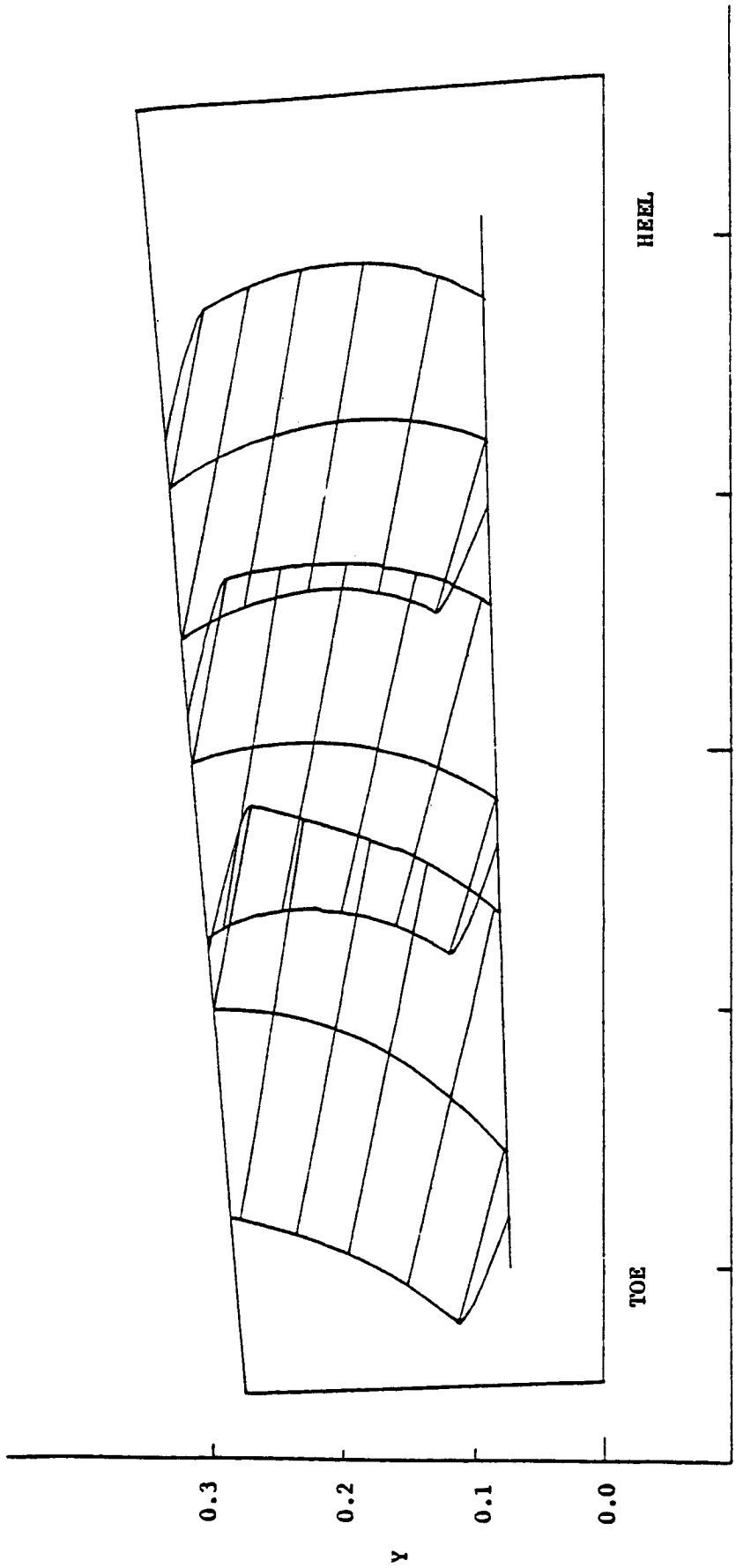

Fig. 2-34. Contact Patterns for Central Contact , Toe Contact and Heel Contact (drive side)

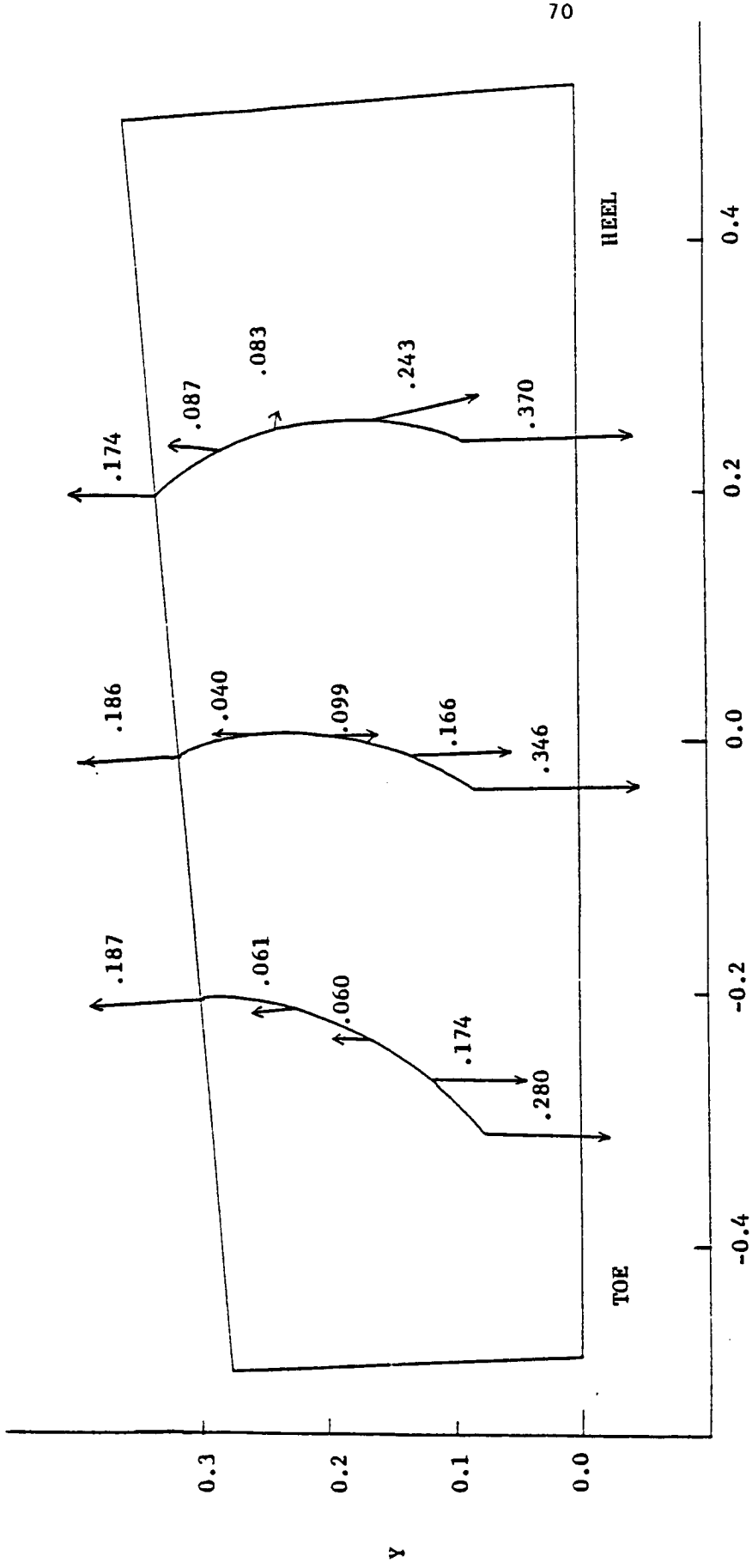

Fig. 2-35. Sliding Velocity For Unit Pinion Rotational Velocity (in/sec)

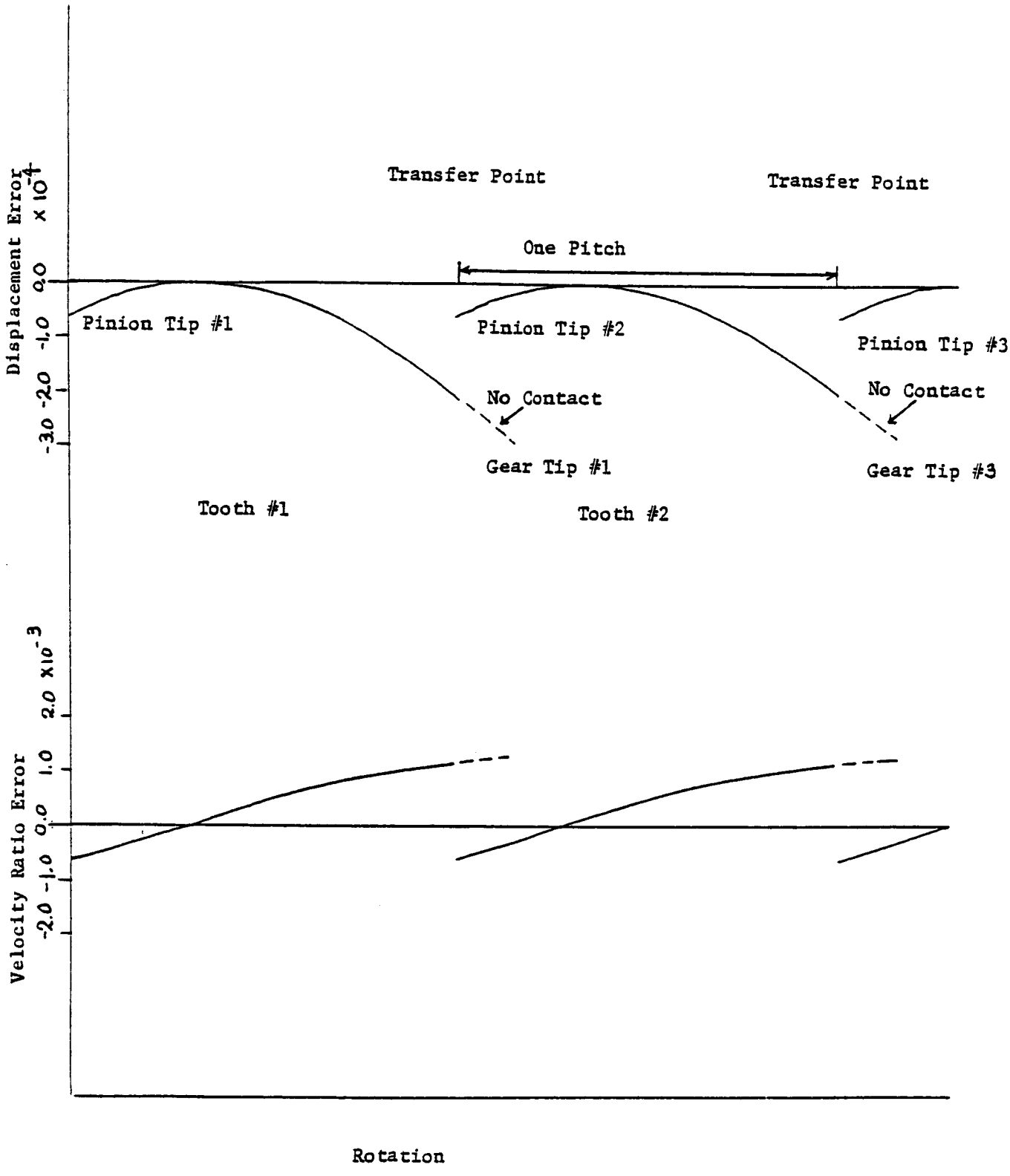

Fig. 2-36. Motion Graphs (drive side) For Successive Tooth Meshes

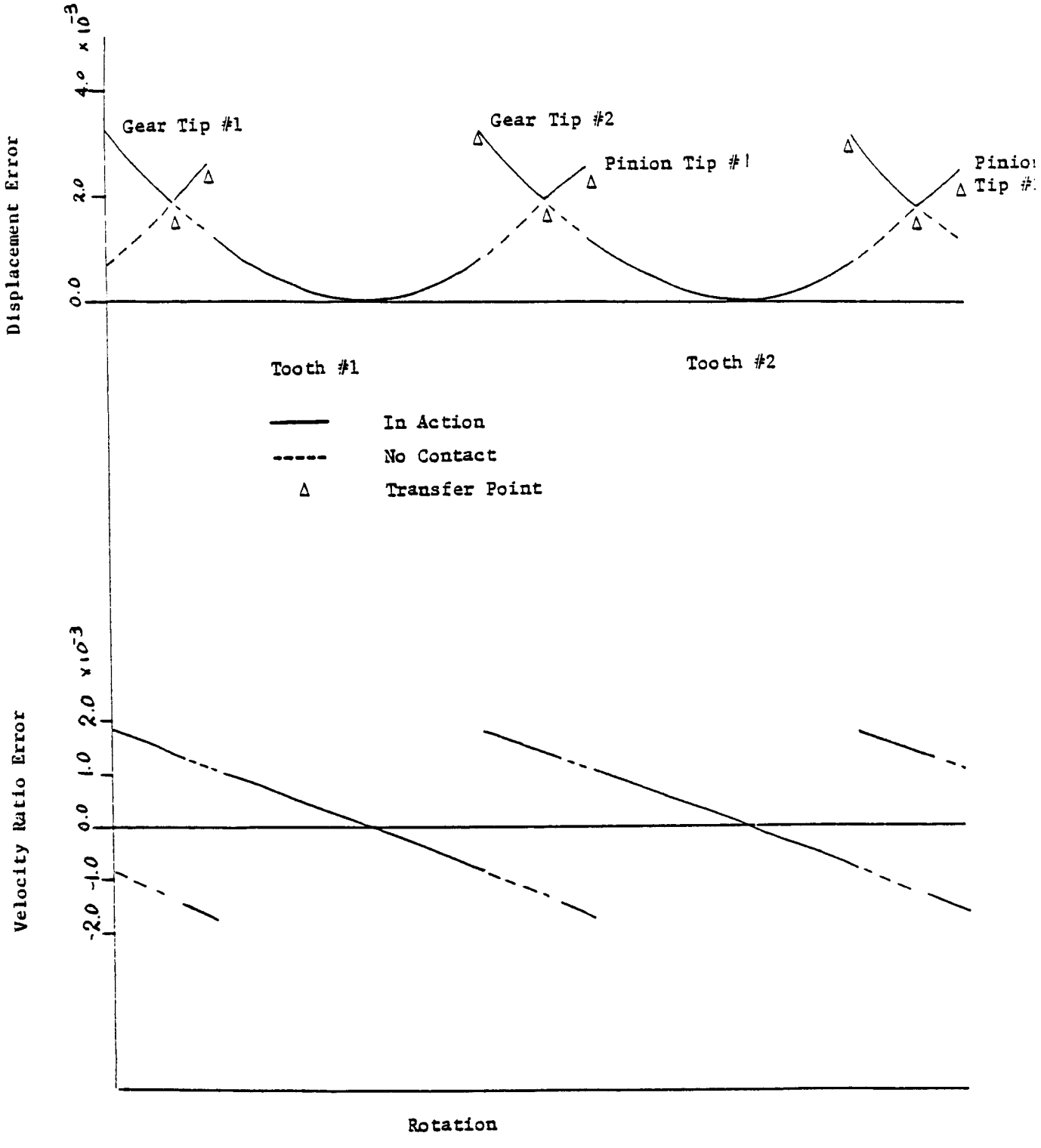

Fig. 2-37. Motion Graphs (coast side) for successive Tooth Meshes

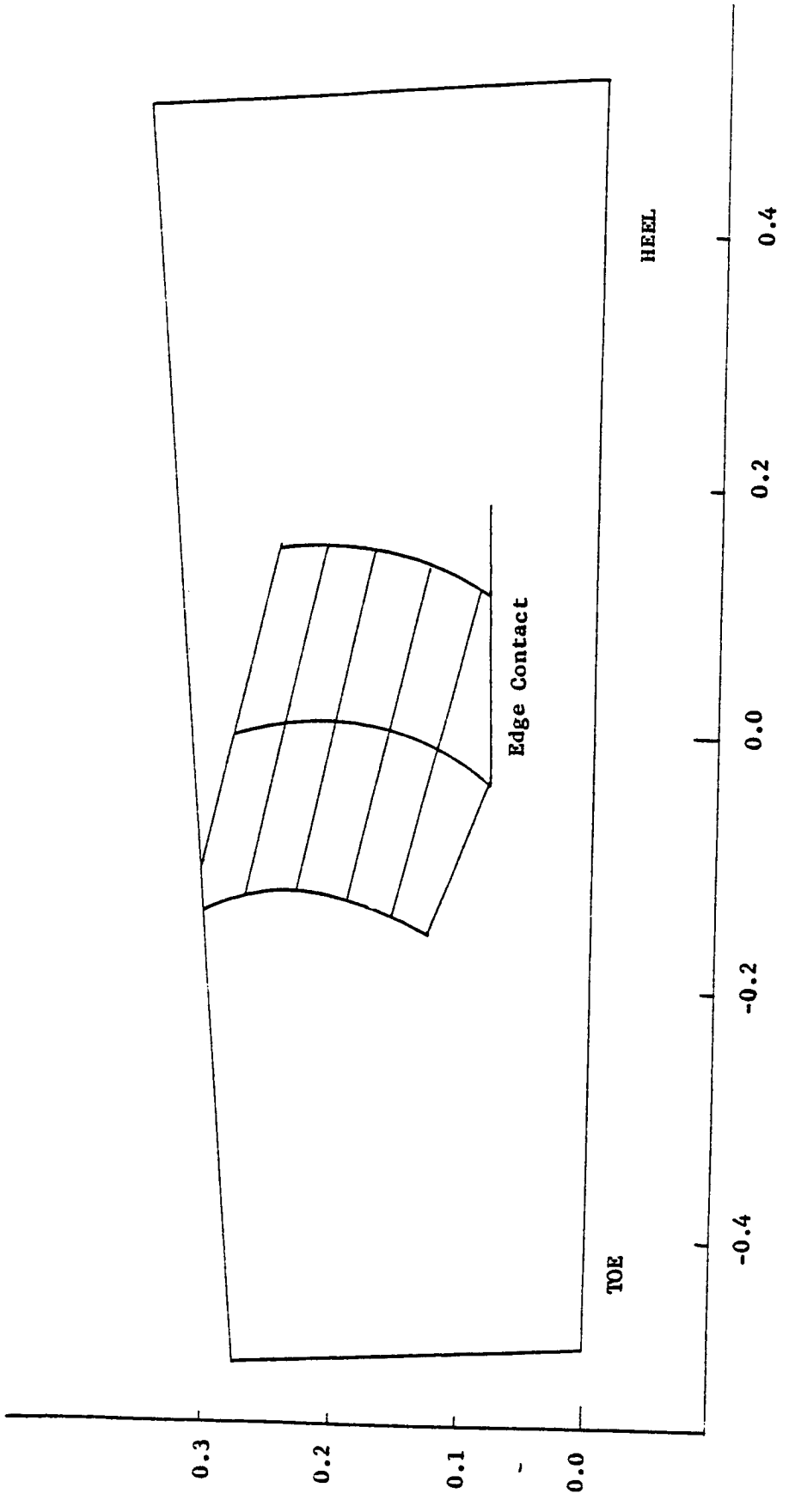

Fig. 2-38. Actual Contact Pattern (drive side)

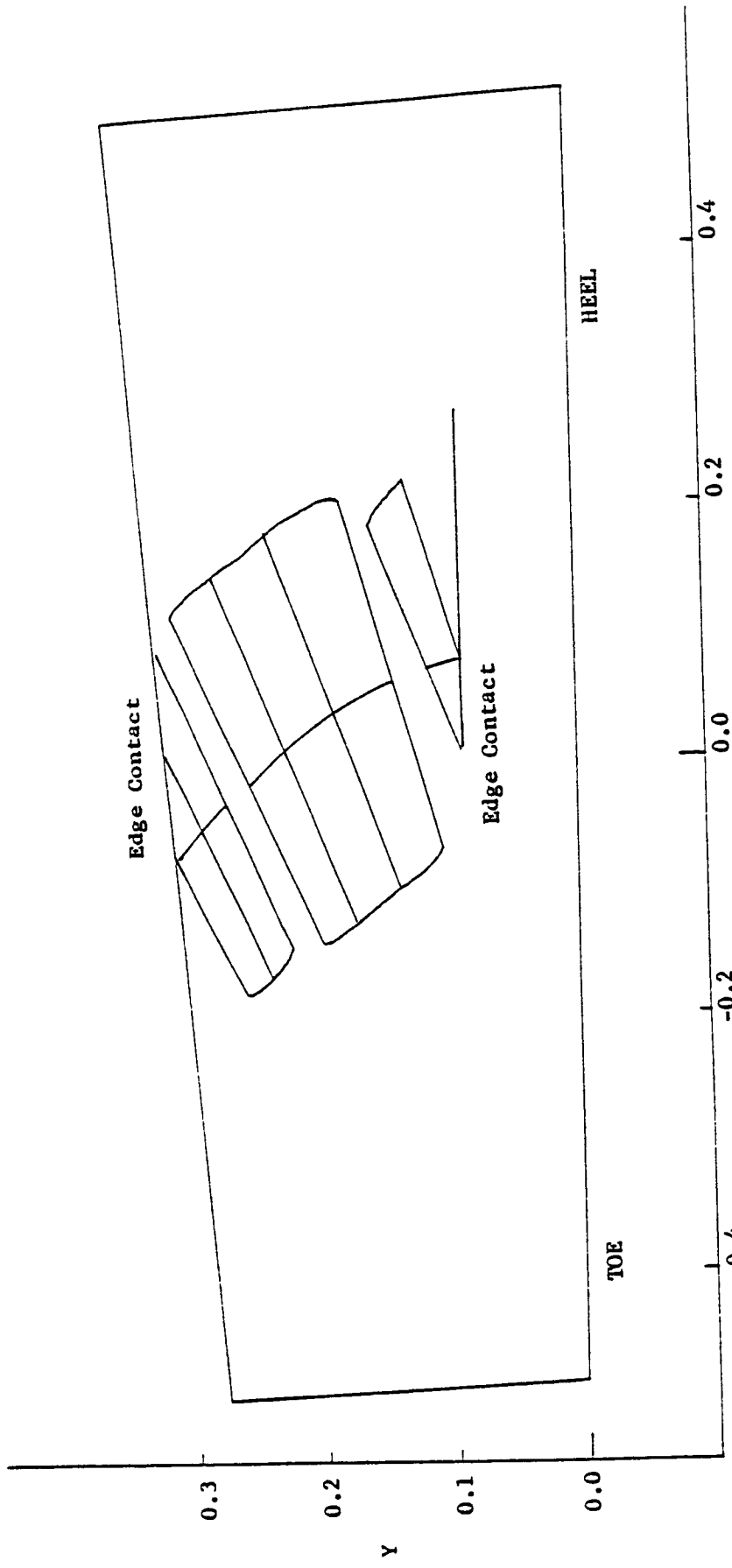

Fig. 2-39. Actual Contact Pattern (coast side)

CHAPTER III

DYNAMICS OF SPIRAL BEVEL GEARS

3.1 Introduction

One of the main uncertainties in gear failure analysis is the load imposed on the gear teeth at high speeds where the inertia forces of the gear wheel and shaft become significant. The dynamic response of the operating system plays an important role in gear design because the movement of the gear body will shift the contact bearing to an undesirable position as a result of the misalignment of shaft. The dynamic load in gearing has received continuous attention in the past, and many studies have been reported (1-9). As far as the dynamic response of bevel gears is concerned, most of the studies have been conducted experimentally in the laboratory. One of the recent measurements is by Terauchi and Fujii (10) in which the dynamic load of gear teeth of straight bevel gears is obtained by using a power circulating gear testing machine. There is a lack of analytical study of the vibration of spiral bevel gears. For instance, some industrial practice still depends upon Buckingham's formulae or upon empirical factors for designing spiral bevel gears.

Analytical studies of spiral bevel gears are extremely complex because: 1. the tooth profile of spiral bevel gears is generated by the cutting machine, and it is difficult to describe the tooth surface,which is much more complicated than that of spur and helical gears; 2. the tooth contact patterns of spiral bevel gears vary with the assembly errors caused by

the apex error, shaft alignment, etc.; 3. being different from spur gears, the spiral bevel gears have also lateral vibration in addition to rotational vibration. In this report, efforts are made to explore the effects of all these factors on the dynamic behavior of the spiral bevel gears.

3.2 Formulation

The main objective in this section is to formulate a dynamic model and equations of motion to simulate, in the steady state, the periodic motion of both the pinion and the gear as well as the tooth load during a typical cycle, in which a pair of teeth traverses through the zone of action from point A to point C as shown in Fig. 3-1.

In developing the equations of motion, the pinion and the gear were assumed to be rigid bodies each having six degrees of freedom. The supporting bearing was assumed flexible with known spring stiffness. At the contact of each pair of teeth in the zone of action, the teeth were assumed to be connected by a linear spring which is oriented normal to the contact point and has a stiffness to be determined separately by a finite element model.

The equations of motion of a rigid body in three dimension are (see Fig. 3-2):

$$\Sigma \bar{F} = m \bar{a}$$
$$\Sigma \bar{M}_G = \dot{\bar{H}}_G \qquad (3.1)$$

where $\bar{F}$: external force vector

m : mass

$\bar{a}$: acceleration vector of the mass center

$\bar{M}_G$: vector of external moment about the gravity center

$\dot{\bar{H}}_G$: vector of rate of change of angular momentum about the mass center

The following derivation is described separately for pinion and gear.

3.2.1 Pinion

Let the moving coordinate axes x'_p, y'_p, z'_p be the principal axes of the inertia of the body so that the axis of the rotation of the body will direct along one of these axes, which is named the dominant axis. The pinion shaft is not fixed in the moving coordinate, but rotates about the dominant axis y'_p at an average velocity ω_p which is the operational rotation velocity of the shaft. XYZ axes are fixed coordinates in space (see Fig. 3-1). In the case of the pinion, the dominant axis is along the Y axis, hence the angular momentum of the pinion about the mass center is

$$\bar{H}_{Gp} = I_{x'p}\dot{\theta}_{x'p}\bar{i}'_p + I_{y'p}(\dot{\theta}_{y'p} + \omega_p)\bar{j}'_p + I_{z'p}\dot{\theta}_{z'p}\bar{k}'_p \tag{3.2}$$

and the rate of change of $\bar{H}_G$ in the moving coordinate

$$\dot{\bar{H}}_{Gp} = I_{x'p}\ddot{\theta}_{x'p}\bar{i}'_p + I_{y'p}\ddot{\theta}_{y'p}\bar{j}'_p + I_{z'p}\ddot{\theta}_{z'p}\bar{k}'_p \tag{3.3}$$

$$+ \bar{\Omega}_p \times (I_{x'p}\dot{\theta}_{x'p}\bar{i}'_p + I_{y'p}(\dot{\theta}_{y'p} + \omega_p)\bar{j}'_p + I_{z'p}\dot{\theta}_{z'p}\bar{k}'_p)$$

$$\bar{\Omega}_p = (\dot{\theta}_{x'p}\bar{i}'_p + \dot{\theta}_{y'p}\bar{j}'_p + \dot{\theta}_{z'p}\bar{k}'_p) \tag{3.4}$$

$$\dot{\bar{H}}_{Gp} = [I_{x'p}\ddot{\theta}_{x'p} - I_{y'p}\omega_p\dot{\theta}_{z'p} + (I_{z'p} - I_{y'p})\dot{\theta}_{y'p}\dot{\theta}_{z'p}]\ \bar{i}'_p$$

$$+\left[I_{y'p}\ddot{\theta}_{y'p} + (I_{x'p} - I_{z'p})\dot{\theta}_{x'p}\dot{\theta}_{z'p}\right] \quad \bar{j}'_p \qquad (3.5)$$

$$+\left[I_{z'p}\ddot{\theta}_{z'p} + I_{y'p}\omega_p\dot{\theta}_{x'p} + (I_{y'p}-I_{x'p})\dot{\theta}_{x'p}\dot{\theta}_{y'p}\right] \quad \bar{k}'_p$$

$\dot{\theta}_{y'p}$ is the rotation velocity variation from ω_p. The true rotation velocity along the dominant axis is $\dot{\theta}_{y'p} + \omega_p$. Assuming $\dot{\theta}_{y'p}$ is much less than ω_p and the magnitude of $\dot{\theta}_{x'p}$, $\dot{\theta}_{y'p}$ and $\dot{\theta}_{z'p}$ is of the same order, and neglecting the higher order terms, one obtains a linearized equation

$$\dot{\bar{H}}_{Gp} = \left[I_{x'p}\ddot{\theta}_{x'p} - I_{y'p}\omega_p\dot{\theta}_{z'p}\right] \quad \bar{i}'_p$$

$$+\left[I_{y'p}\ddot{\theta}_{y'p}\right] \quad \bar{j}'_p \qquad (3.6)$$

$$+\left[I_{z'p}\ddot{\theta}_{z'p} + I_{y'p}\omega_p\dot{\theta}_{x'p}\right] \quad \bar{k}'_p$$

so the governing equations become

$$\sum_{i=1}^{M} \bar{F}_{rpi} + \sum_{i=1}^{N} \bar{F}_{cpi} = m_p(\ddot{x}'_{cp}\bar{i}'_p + \ddot{y}'_{cp}\bar{j}'_p + \ddot{z}'_{cp}\bar{k}'_p) \qquad (3.7)$$

$$\sum_{i=1}^{M} \bar{\gamma}_{rpi} \times \bar{F}_{rpi} + \sum_{i=1}^{N} \bar{\gamma}_{cpi} \times \bar{F}_{cpi} + \text{Input Torque}$$

$$= \left[I_{x'p}\ddot{\theta}_{x'p} - I_{y'p}\omega_p\dot{\theta}_{z'p}\right] \quad \bar{i}'_p \qquad (3.8)$$

$$+\left[I_{y'p}\ddot{\theta}_{y'p}\right] \qquad \bar{j}'_p$$

$$+\left[I_{z'p}\ddot{\theta}_{z'p} + I_{y'p}\omega_p\dot{\theta}_{x'p}\right] \qquad \bar{k}'_p \tag{3.8}$$

where M is number of bearing reaction force, N is number of contact force, and $\ddot{x}'_{cp}$, $\ddot{y}'_{cp}$, and $\ddot{z}'_{cp}$ are the components of the absolute acceleration of the pinion mass center in the x', y' and z' direction.

3.2.2 Gear

These results are similar to the equations for the pinion, except that the dominant axis in the case of the gear is X axis and the operational rotation velocity is ω_g, the equations of motion for the gear are:

$$\sum_{i=1}^{M} \bar{F}_{rgi} + \sum_{i=1}^{N} \bar{F}_{cgi} = m_g(\ddot{x}'_{cg}\bar{i}'_g + \ddot{y}'_{cg}\bar{j}'_g + \ddot{z}'_{cg}\bar{k}'_g) \tag{3.9}$$

$$\sum_{i=1}^{M} \bar{\gamma}_{rgi} \times \bar{F}_{rgi} + \sum_{i=1}^{N} \bar{\gamma}_{cgi} \times \bar{F}_{cgi} + \text{Output Torque}$$

$$=\left[I_{x'g}\ddot{\theta}_{x'g}\right] \qquad \bar{i}'_g$$

$$+\left[I_{y'g}\ddot{\theta}_{y'g} + I_{x'g}\omega_g\dot{\theta}_{z'g}\right] \qquad \bar{j}'_g \tag{3.10}$$

$$+\left[I_{z'g}\ddot{\theta}_{z'g} - I_{x'g}\omega_g\dot{\theta}_{y'g}\right] \qquad \bar{k}'_g$$

Some preliminary work must be completed before the twelve equations in the system can be solved. These are: 1) expressing the force terms $\bar{F}_{ri}$ and $\bar{F}_{ci}$ in terms of the displacement unknowns in the fixed coordinate; 2) expressing the displacement unknowns in the fixed coordinate by the displacement unknowns in x'y'z' system in which the equations are solved.

Because the contact force is assumed to always be in the normal direction of the contact point on the tooth surface, the scalar quantity of the contact force can be used effectively in the derivation if the direction vector of the contact point is known. For simplification, the matrix notation is used, and some basic column matrices are introduced:

$$\{D'\}_g = (x'_g,\ y'_g,\ z'_g,\ \theta_{x'g},\ \theta_{y'g}\ \ \theta_{z'g})^T \tag{3.11}$$

$$\{D'\}_p = (x'_p,\ y'_p,\ z'_p,\ \theta_{x'p},\ \theta_{y'p},\ \theta_{z'p})^T \tag{3.12}$$

which are the displacement unknowns in the moving coordinate system, while

$$\{D\}_g = (x_g, y_g, z_g, \theta_{xg},\ \theta_{yg}, \theta_{zg})^T \tag{3.13}$$

$$\{D\}_p = (x_p, y_p, z_p, \theta_{xp}, \theta_{yp}, \theta_{zp})^T \tag{3.14}$$

are the displacement components in the fixed coordinate.

From the configuration of the gear system, the displacement components at the contact point i in the normal direction (G_n) can be

expressed in terms of the rigid body displacements as:

$$\{G_{ni}\}_g = [DG_i]_g \{D\}_g \tag{3.15}$$

$$\{G_{ni}\}_p = [DG_i]_p \{D\}_p \tag{3.16}$$

and the bearing reaction force at bearing j can also be expressed in terms of rigid body displacements by:

$$\{F_{rj}\}_g = -[DK_j]_g \{D\}_g \tag{3.17}$$

$$\{F_{rj}\}_p = -[DK_j]_p \{D\}_p \tag{3.18}$$

where i and j are from one to the number of contact forces and number of bearings, respectively. The displacements at contact point i due to elastic deformation along the direction of contact normal are:

$$\{\delta_{nci}\}_g = [DC_{ij}]_g \{F_{cj}\}_g \tag{3.19}$$

$$\{\delta_{nci}\}_p = [DC_{ij}]_p \{F_{cj}\}_p \tag{3.20}$$

where i, j are from one to the total number of contact points. The unit outward normal vector at contact point i, is denoted $\bar{n}ci$. The positive value of F_{ci} is taken so that contact force is acting along

the same direction as the outward pointing normal vector. Since only the scalar quantity of the contact force is considered in the equation, the relation $\{F_{ci}\}_g = \{F_{ci}\}_p$ is always true at each contact point.

The total displacements in the normal direction, which include both the rigid body and the elastic deformations, will be the same for the two contacting bodies. This relation gives:

$$\bar{n}_{cig} \cdot (\{\delta_i\}_g + \{G_i\}_g) = - \bar{n}_{cip} \cdot (\{\delta_i\}_p + \{G_i\}_p) \tag{3.21}$$

$$\{\delta_{nci}\}_g + \{G_{ni}\}_g = - \{\delta_{nci}\}_p - \{G_{ni}\}_p \tag{3.22}$$

$$[DC_{ji}]_g \{F_{ci}\}_g + \{G_{ni}\}_g = - [DC_{ji}]_p \{F_{ci}\}_p - \{G_{ni}\}_p$$

$$\{F_{ci}\}_g = - ([DC_{ji}]_g + [DC_{ji}]_p)^{-1} (\{G_{ni}\}_g + \{G_{ni}\}_p) \tag{3.23}$$

and

$$\{F_{ci}\}_g = - ([DC_{ji}]_g + [DC_{ji}]_p)^{-1} ([DG_i]_g \{D\}_g + [DG_i]_p \{D\}_p) \tag{3.24}$$

which is the equation relating the contact force and the rigid body displacement unknowns. The displacements in different coordinate systems can be transferred from one to another by means of the following relations (10),

$$\begin{Bmatrix} x' \\ y' \\ z' \end{Bmatrix} = [\theta^u] \begin{Bmatrix} x'' \\ y'' \\ z'' \end{Bmatrix} \tag{3.25}$$

$$\begin{Bmatrix} x'' \\ y'' \\ z'' \end{Bmatrix} = [\theta^k] \begin{Bmatrix} x \\ y \\ z \end{Bmatrix} \tag{3.26}$$

$$\begin{Bmatrix} x' \\ y' \\ z' \end{Bmatrix} = [\theta^u]\,[\theta^k] \begin{Bmatrix} x \\ y \\ z \end{Bmatrix} \tag{3.27}$$

where $[\theta^u]$ is the transformation matrix for rotation in x'y'z' coordinate, $[\theta^k]$ is the transformation matrix for rotation in xyz coordinate.

Incorporating all the above force and displacement relations into the equations of motion for the pinion and gear and then rearranging the matrices, one can obtain the final form of the twelve equations.

$$[m] \begin{Bmatrix} \{\ddot{D}'\}_g \\ \{\ddot{D}'\}_p \end{Bmatrix} + [c] \begin{Bmatrix} \{\dot{D}'\}_g \\ \{\dot{D}'\}_p \end{Bmatrix} + [k] \begin{Bmatrix} \{D'\}_g \\ \{D'\}_p \end{Bmatrix} = \{R\} \tag{3.28}$$

The details of matrix [m], [c] and [k] are derived in Appendix C.

After examining the equations of motion, it was found that the fourth equation governing the rotational motion along the dominant axis

of the gear, and the eleventh equation governing the rotational motion along the dominant axis of the pinion can be reduced to a single equation. The reduced equation is similar to that describing the vibratory system of two masses connected by a spring. In this equation, it is convenient to convert the rotational motion into a motion along an artificial line of action. Like the line of action in spur gears, the artificial line of action in spiral bevel gears is defined as the effective component of $\bar{\gamma} \times \bar{n}$ to produce the torque along the dominant axis, where $\bar{\gamma}$ is a position vector from the mass center to the contact point, and $\bar{n}$ is a unit normal vector at the contact point.

The 4th and 11th equations of motion are rewritten here as

$$I_{x'g}\ddot{\theta}_{x'g} = (\Sigma\ \bar{\gamma}_{cgi} \times \bar{F}_{cgi})_{x'g} + (\text{Output Torque})_{x'g} \tag{3.29}$$

$$I_{y'p}\ddot{\theta}_{y'p} = (\Sigma\ \bar{\gamma}_{cpi} \times \bar{F}_{cpi})_{y'p} + (\text{Input Torque})_{y'p} \tag{3.30}$$

The following new variables are introduced:

$$\theta_g = RBG \cdot \theta_{x'g} \tag{3.31}$$

$$\theta_p = RBP \cdot \theta_{y'p} \tag{3.32}$$

Letting FMA denote the magnitude of the contact force and T_c be the static force, the equations become

$$(\Sigma\ \overline{\gamma}_{cgi} \times \overline{F}_{cgi})_{x'g} = FMA \cdot RBG \tag{3.33}$$

$$(\Sigma\ \overline{\gamma}_{cpi} \times \overline{F}_{cpi})_{y'p} = - FMA \cdot RBP \tag{3.34}$$

$$(\text{Output Torque})_{x'g} = - T_c \cdot RBG \tag{3.35}$$

$$(\text{Input Torque})_{y'p} = T_c \cdot RBP \tag{3.36}$$

RBG and RBP are treated as the radii of the effective base circle of spiral bevel gears. Eqs. (3.29) and (3.30) become

$$\frac{I_{x'g}}{RBG} \ddot{\theta}_g = RBG \cdot FMA - T_c \cdot RBG \tag{3.37}$$

$$\frac{I_{y'p}}{RBP} \ddot{\theta}_p = - RBP \cdot FMA + T_c \cdot RBP \tag{3.38}$$

Defining

$$J_{xg} = \frac{I_{x'g}}{RBG^2} \tag{3.39}$$

and

$$J_{yp} = \frac{I_{y'p}}{RBP^2} \tag{3.40}$$

one obtains

$$J_{xg} \ddot{\theta}_g = FMA - T_c \tag{3.41}$$

$$J_{yp} \ddot{\theta}_p = - FMA + T_c \tag{3.42}$$

Introducing an equivalent mass J and a relative displacement θ_{pg}

$$J = \frac{J_{xg} \cdot J_{yp}}{J_{xg} + J_{yp}} \tag{3.43}$$

$$\theta_{pg} = \theta_p - \theta_g \tag{3.44}$$

the reduced equation, including damping terms, becomes

$$J \ddot{\theta}_{pg} + C \dot{\theta}_{pg} + FMA = T_c \tag{3.45}$$

After the relationship between the 11 displacement unknowns and the magnitude of the contact force is rewritten, the system can be reduced to 11 second order differential equations with state dependent coefficients. These equations were solved numerically by the Runge-Kutta method. The unknown initial conditions (11 displacements and 11 velocities) can be iterated by taking the previous calculated values at the end of each iteration. The criterion of the iteration is to force the equation to satisfy the periodic contact condition. The static displacements and zero velocities are taken as first guessed values.

To implement the above equations, the following state coefficients are needed:

(1) The tooth contact position as a function of the relative rigid body displacements of the two shafts,

(2) The direction of the normal vector at the contact point,

(3) The combined stiffness of the teeth at the contact point.

The teeth contact position and the direction of the normal vector at the contact point can be obtained from Chapter II. Because of the geometric complexity of spiral bevel gears, there is no satisfactory formula available to calculate the deformation of the tooth surface. A finite element program, to be described in Section 3.3, was used in this study to calculate the deformation due to a unit load applied at a given contact point of spiral bevel gears.

3.3 Tooth Deflection

For most gear applications, the contact ratio is greater than one, that is, there will be more than one pair of teeth in contact during some portion of the whole engagement. When the load is shared by two contacts, it cannot be assumed that the load is distributed equally among the pairs of teeth in contact because this is a statically indeterminate case. Therefore, one must consider the tooth deflection under the load for each pair in order to determine the load sharing characteristics among the pairs.

Because of the complexity of the spiral bevel gear geometry, there are no existing simplified methods for calculating the suitable tooth deflection. In order to investigate the system response, the gear shaft must also be included in the calculation of tooth deflection.

Some of the recent applications of finite elements in determining tooth deflection can be found in Refs. 9 and 12, where it was shown that more accurate results can be obtained by using the finite element method. Most of this work dealt with two dimensional problems and did not include the whole gear body. Fig. 3-4 shows a typical 8-node solid element grid pattern for a gear and a pinion with three adjacent teeth attached to the gear wheel and shaft. Fig. 3-5 shows the central tooth and its attached ring element of the gear. Fig. 3-6 shows parts of the gear shaft and the gear wheel. Fig. 3-7 shows the entire ring element with three adjacent teeth of the pinion. Fig. 3-8 shows the elements of the pinion shaft. The central tooth was subject to load to calculate the deflection. There are 941 nodes, 562 elements for the

gear model, and 1029 nodes, 584 elements for the pinion model. Using this grid as the input, one can readily compute the deflection δ under a load P applied at any grid point in the tooth surface. For this analysis, the MARC-CDC program was used, the boundaries were considered to be fixed for all the points connected to thrust bearing to eliminate rigid body displacement, and the boundaries nodes connected to the radial bearing was allowed to move in the direction of dominant axis.

The stiffness at grid point i is defined as

$$KS_{gi} = \frac{P}{\delta_{gi}} \tag{3.46}$$

$$KS_{pi} = \frac{P}{\delta_{pi}} \tag{3.47}$$

The stiffness (KS_g, KS_p) of the point other than the grid point in the tooth surface can be calculated by the interpolation method. The details are shown in Appendix D. The combined stiffness at contact point is expressed as

$$KS = \frac{KS_g \cdot KS_p}{KS_g + KS_p} \tag{3.48}$$

3.4 Results and Discussion

A series of solutions were obtained to simulate the dynamic response of a set of spiral bevel gears currently being tested at NASA-Lewis. The data for this gear set and the lubricant data are listed in Table 3.1. Effects studied include running speed, shaft misalignment, and system damping. These results are presented in this section. The dynamic response is expressed by a dynamic load factor defined as the ratio of the maximum dynamic load along the contact path to the average static load. This factor is plotted as a function of speed with different damping ratios and contact ratios.

3.4.1 Dynamic Load Variation

For a constant input torque, the load on the contact point of the two meshing teeth along the path of contact is not constant. This load variation is mainly caused by the following factors:

1. The variation of stiffness along the contact path.
2. The transition from a single pair of contacts to a double and from double to single.
3. The effective radius is not constant along the contact path.

Fig. 3-9 shows the variation of effective radius of pinion. Fig. 3-10 shows the variation and jump of stiffness for the transition of contacts.

The main excitation to the gear system comes from the periodical change in teeth stiffness due to the alternating engagement of single and double pairs of teeth. The frequency of this excitation force, expressed as a meshing frequency, depends on the operating speed.

Therefore, it dominates the resulting mode of vibration. Fig. 3-11 to Fig. 3-14 show dynamic load variation at four different speeds in the case of central contact, that is, when the contact path is located centrally between the toe and the heel of the tooth.

Since there are eleven degrees of freedom in the system, eleven resonating frequencies of the system should exist. In the low speed region where the excitation frequency from the change of stiffness is much lower than all resonating frequencies, the dynamic load response along the path of contact is somewhat like static load superimposed by an oscillatory load due to the resonating frequency of the system.

When the speed is near the resonance region (Fig. 3.11), the dynamic load response becomes very severe (Fig. 3-12 and Fig. 3-13). The maximum dynamic load is much higher than the static load, which is the case when overloading occurs. Sometimes the oscillation of dynamic load will make meshing teeth separate when the load becomes negative, and thus generates noise and surface fatigue.

As the speed increases beyond the zone of resonating frequencies, the dynamic load becomes smoother along the contact course, and the value is less than the static load (if the contact ratio is above one). The variation of dynamic load in this region is out of phase with the change of the teeth stiffness (Fig 3-14).

3.4.2 The Effect of Shaft Misalignment

When the assembly errors are introduced in the system, the contact bearing shifted to either end of the tooth surface (11).

Fig. 3-15 shows the typical paths of central contact, toe contact, and heel contact. Usually the central contact is desired because it can tolerate more possible running position errors and avoid edge contact. The dynamic load response of toe and heel contactsare shown in Fig. 3-16 and Fig. 3-17. The change of the contact bearing from the center to either edge will also change the contact ratio of the system because the tooth surface is not a perfect involute along the profilewise direction and is mismatched along the lengthwise direction. In the current example, the contact ratio for the toe contact is 1.26, central contact 1.16, and heel contact 1.0. In this case, if the contact bearing is moved farther toward the heel region, there would be no tooth contact between the time when the previous tooth finishes the contact and current tooth goes into the contact zone (discontinuity in tooth mesh). This situation would cause a very large impact force which would generate noise and severe damage to the tooth surface. The effect of the tooth contact ratio on dynamic response is shown later.

3.4.3 Contact Path Variation Due to Dynamic Response

In addition to showing the contact paths due to assembly errors in the system in Fig. 3-15, the real contact path, including the effects of both assembly errors and running position errors induced by the dynamic responses, is plotted in the same figure. When this real contact path is compared with that caused by the assembly errors and running position errors induced by the average static elastic deformations, the deviation is found to be surprisingly small. One explanation of this small difference might be that the displacements change due to the dynamic oscillation are small, and they do not produce

a large change in contact path compared to those caused by the static displacement only. The closeness between these two contact paths suggests that one can use the average static elastic deformation to calculate the contact path, which can then be used directly to solve for the dynamic load and lubrication behavior without having to solve the dynamic load and contact path simultaneously using an iterative technique. The elimination of this iterative procedure greatly reduces the computation time.

3.4.4 Effect of Speed

Once the physical conditions of a gear set are determined, the dynamic response depends on the operating speed. For a system with one degree of freedom, such as spur gears, the maximum dynamic load occurs when the meshing frequency, which depends on the operating speed, is near the system natural frequency. Some peaks in the dynamic load are caused by the varied meshing stiffness along the contact path, and they appear at meshing frequencies lower than the system natural frequency. The dynamic load factor, defined as the ratio of maximum dynamic load to the average static load, is plotted against the gear speed to illustrate the effect of speed in Fig. 3-18. Since there are eleven degrees of freedom in the spiral bevel gear system, more peaks in the dynamic load are expected.

It is seen that the highest dynamic load appears to occur near the natural frequencies which correspond to the mode associated with the largest displacements in the motion along the line of action. The frequencies marked ↑ in Fig. 3-18 shows the system natural frequency

C-2

causing a larger displacement in the motion along the line of action and the ones marked ↓ shows the system natural frequency with a small displacement in that motion. It is clearly shown that the dynamic load factor at the frequencies marked ↑ has a peak response, and the response at the natural frequencies marked ↓ is not necessarily a peak.

3.4.5 Effect of Contact Ratio

The contact ratio is defined as the ratio of the time required for one tooth to go through the whole contact zone to the time required for a periodic meshing cycle. It is believed that the load sharing characteristics caused by more than one tooth in contact will reduce the static load. The variations in the dynamic load factor due to the effect of changing contact ratio is shown in Figs. 3-19(a) to (c). It can be seen that the maximum dynamic load factor does not change much. However, the contact ratio's effect is significant in high speed regions, where the load is spread out between meshing teeth pairs. A typical dynamic load variation with a high contact ratio along the contact path is shown in Fig. 3-20.

3.4.6 Effect of Damping

Since the damping forces are usually not known in the gear system, three arbitrary values are chosen for the damping coefficients: 2627, 4378, and 6129 N sec/m (15, 25, and 35 lb.sec/in). These values are selected to give a range of non-dimensional damping ratios corresponding to those commonly used in spur gears (0.1-0.2). The non-dimensional damping ratios corresponding to the above damping coefficients are 0.087,

0.14 and 0.203. The dynamic response for these damping cases can be observed from Figs. 3-18, 3-19(a), and 3-21. It is expected that the larger the damping force is, the smaller the dynamic load factor will be in the resonance region. The large damping force will also level off the peak of dynamic load factor in the subresonance region, and there is no effect on the dynamic load factor due to the damping force in the superresonance region.

3.4.7 Effect of Bearing Stiffness

It is well known that the bearing stiffness plays an important part in the dynamic load response because it directly controls the static displacements which determine the contact path. A large stiffness for supporting bearings is sometimes desirable because it pushes all the resonant frequencies beyond the range of the operating speeds. In Fig. 3-22, the dynamic load factor is calculated for a system with "infinite" bearing stiffness. The contact ratio for this case is 1.16, and the damping ratios are 0.058 and 0.14. Since the bearing stiffnesses are infinite, only the rotational mode prevails. Three peaks are shown to exist in Fig. 3-22; two of these are the subharmonics. These results for infinite stiffness are compared with the results shown in Fig. 3-19(a) for a finite stiffness of 3.5×10^8 N/m (2×10^6 lb/in.). It is seen that the natural frequency of the rotational mode with an infinite stiffness is increased to 290 rad./sec. from the natural frequency of 200 rad./sec. for a finite stiffness of 3.5×10^8 N/m.

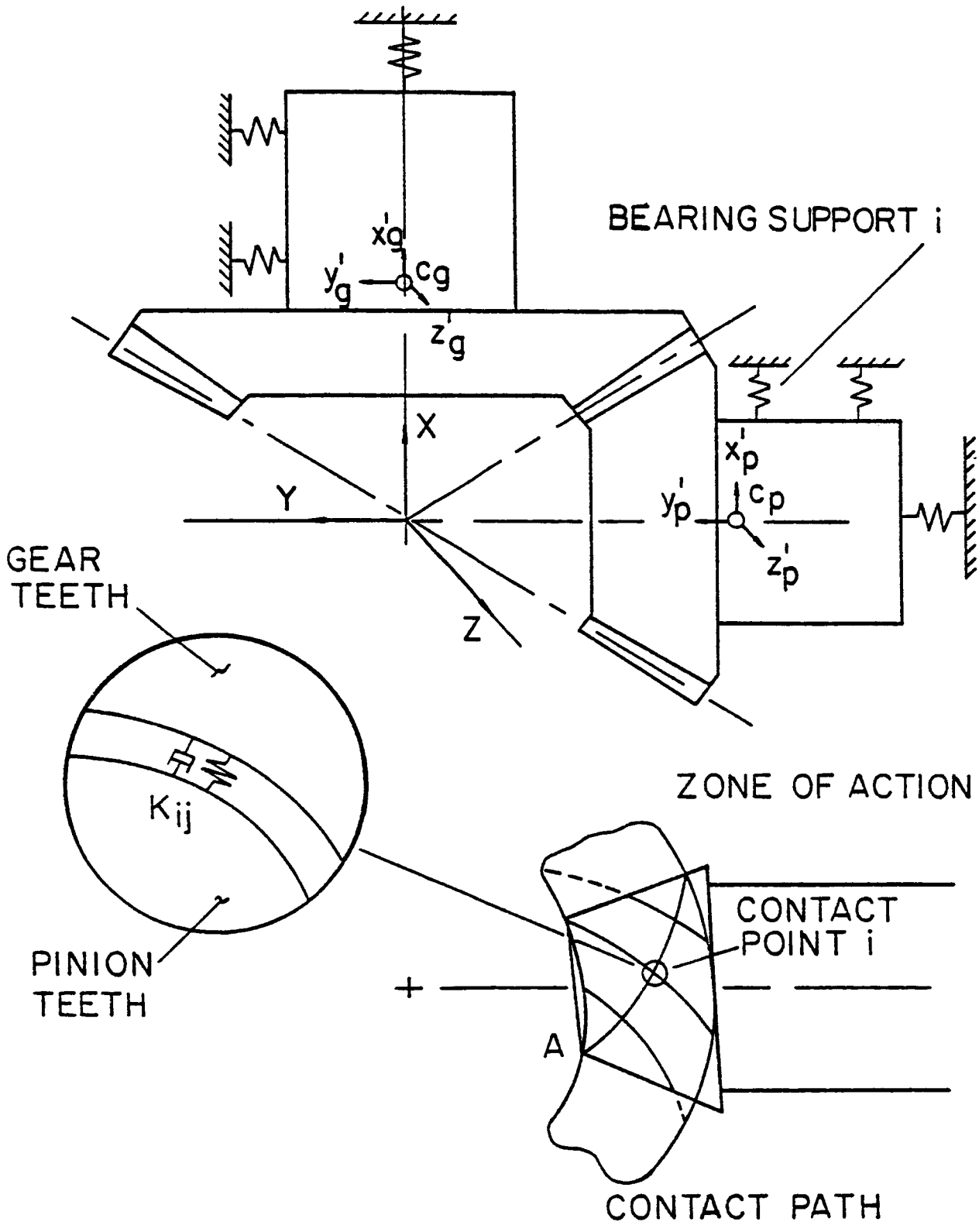

Fig. 3-1. Dynamic Modeling and Zone of Action of Bevel Gears.

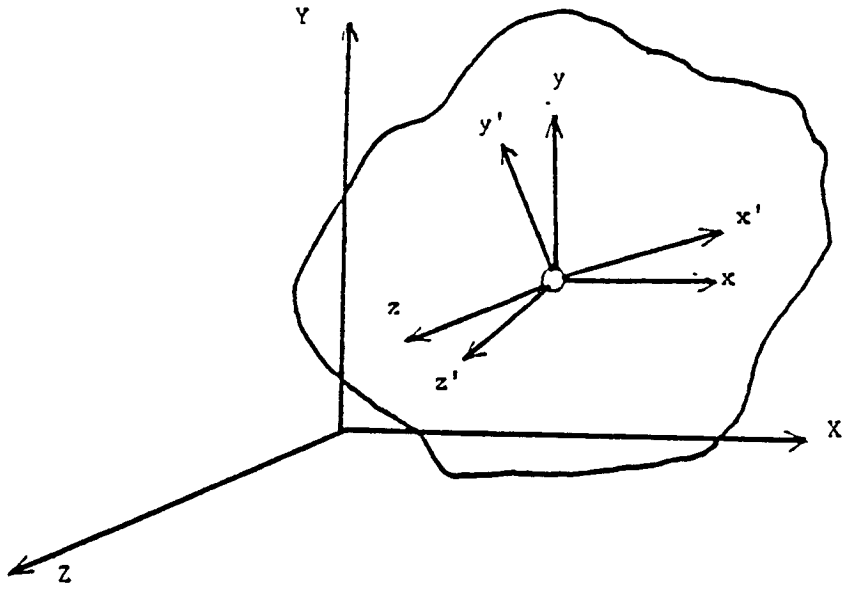

Fig. 3-2 Principal Coordinate in 3-D.

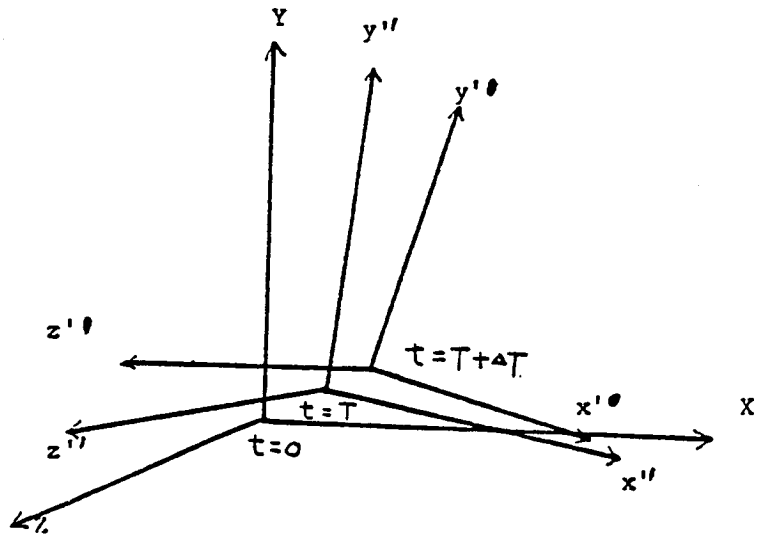

Fig. 3-3. Principal Coordinates at Different Time Intervals

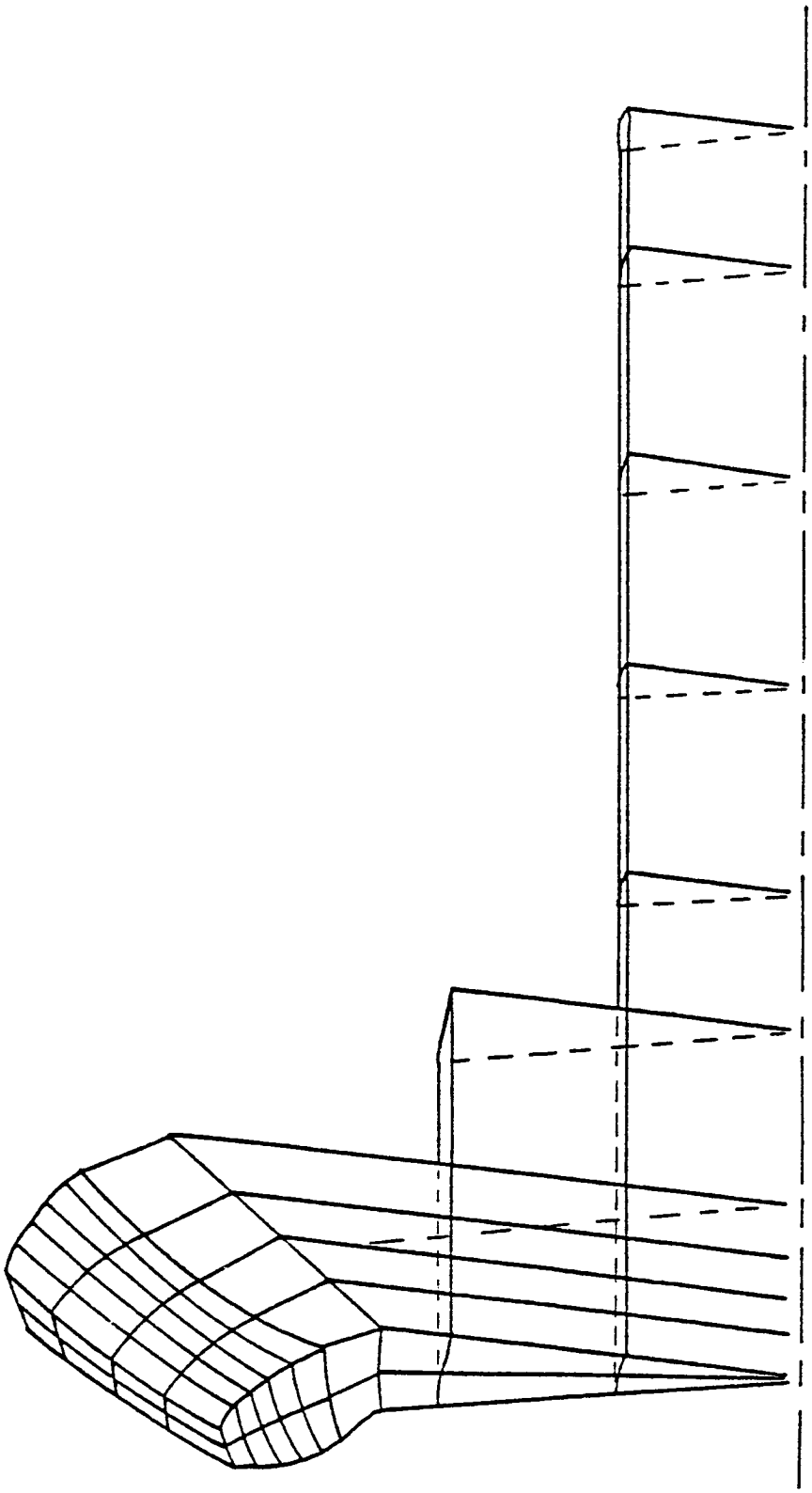

Fig. 3-4. A Typical Section of Elements of Gear

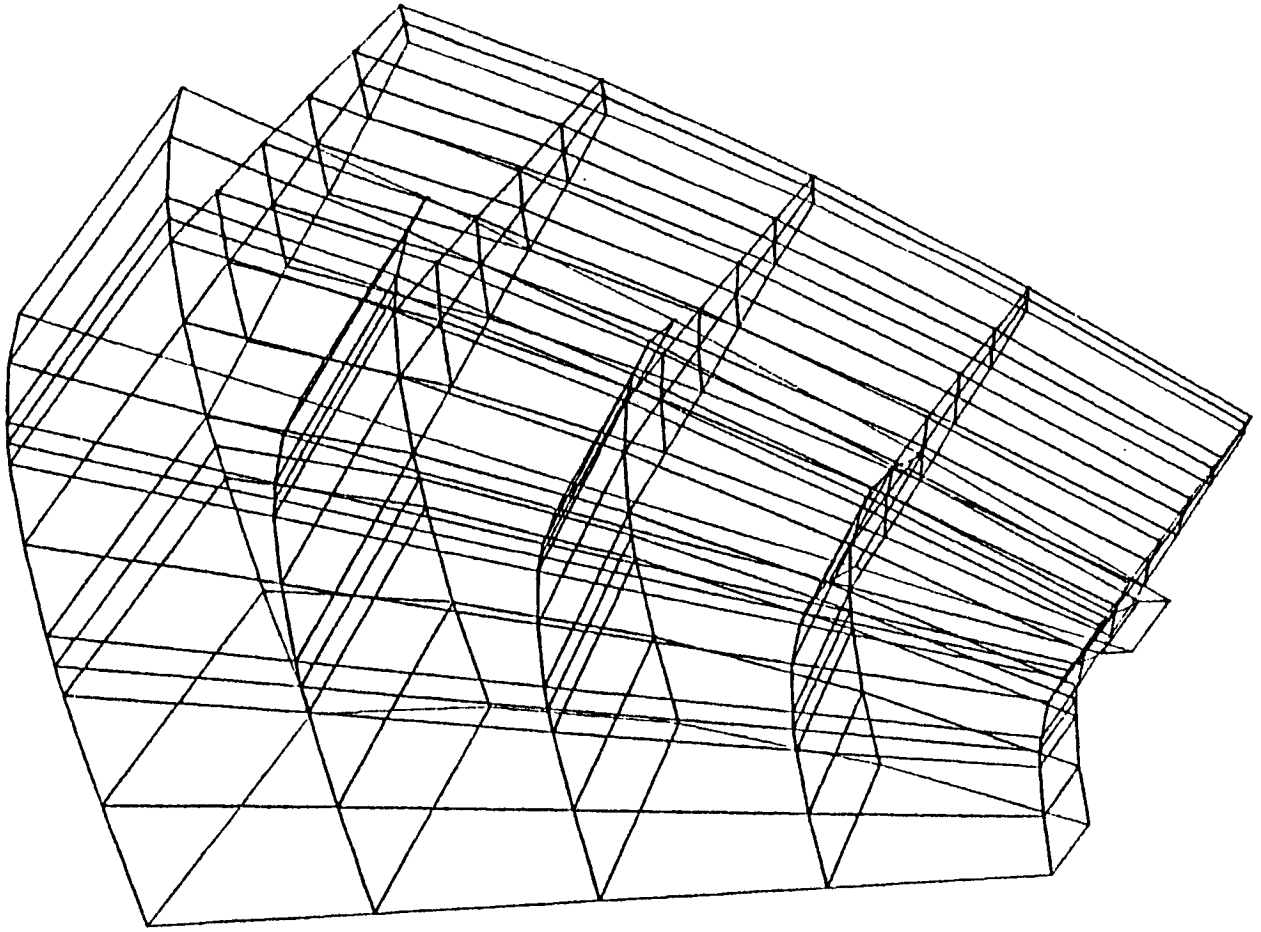

Fig. 3-5. Central Tooth Elements And Attached Rim Elements of Gear

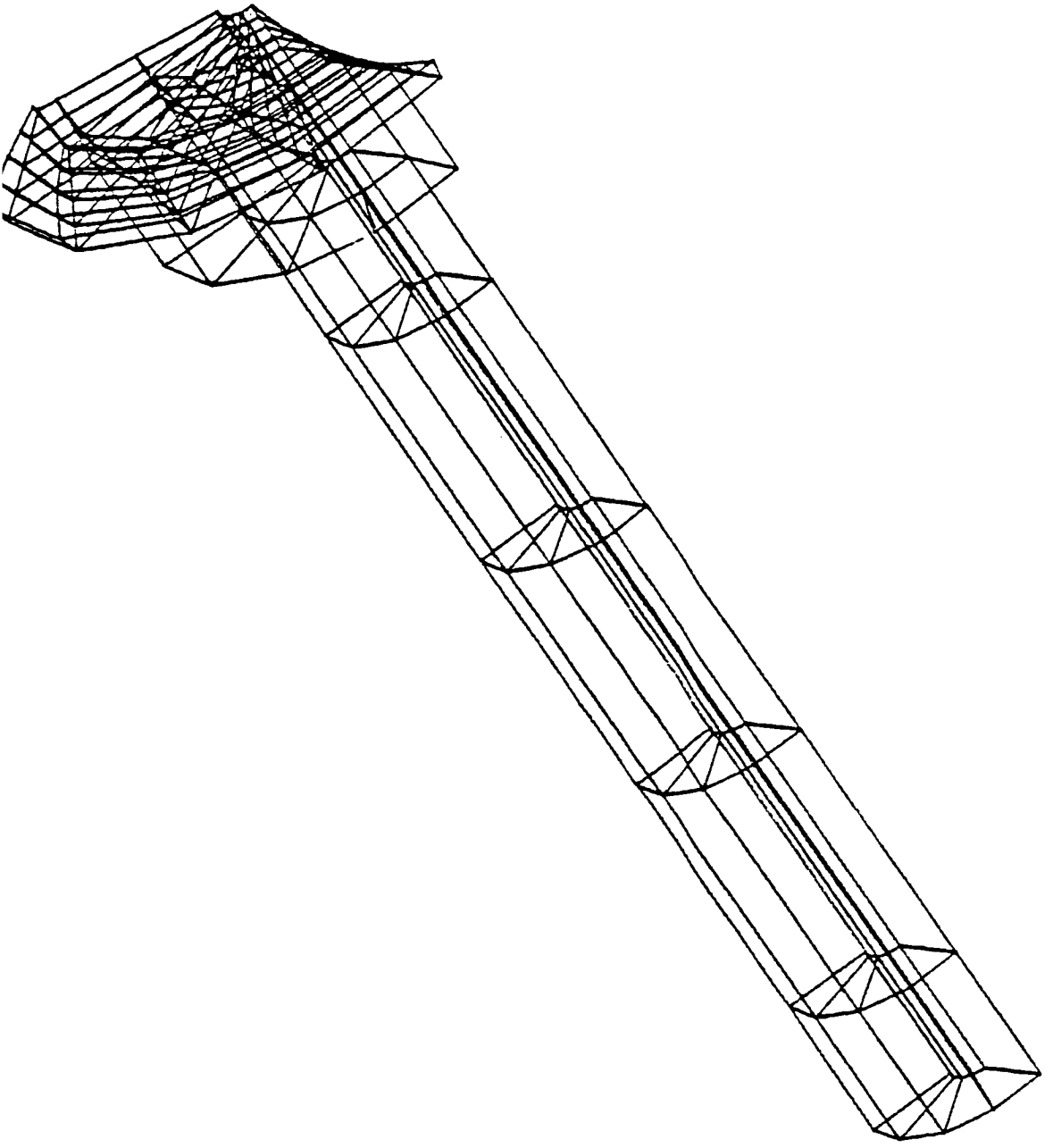

Fig. 3-6. Parts of Gear Shaft And Blank

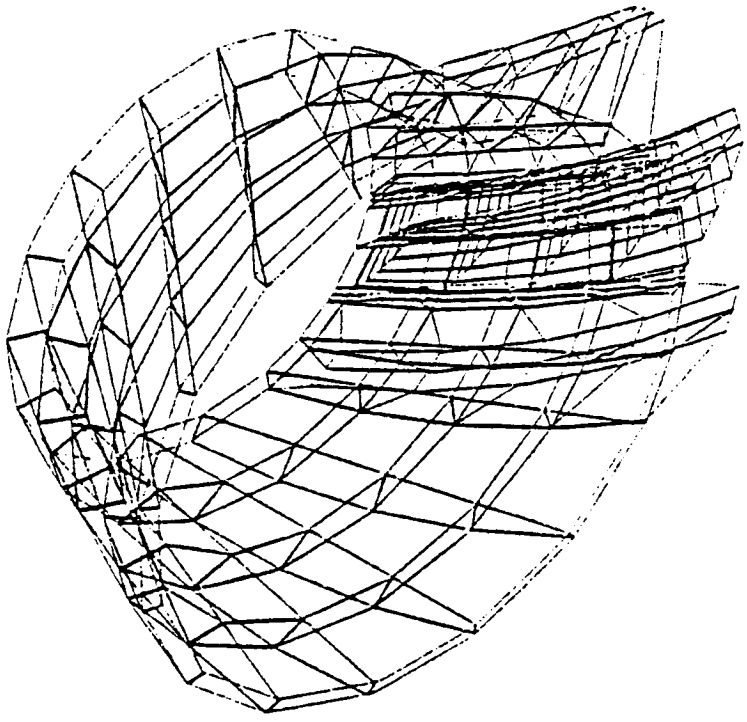

Fig. 3-7. The Elements of Rim And Three Adjacent Teeth of Pinion

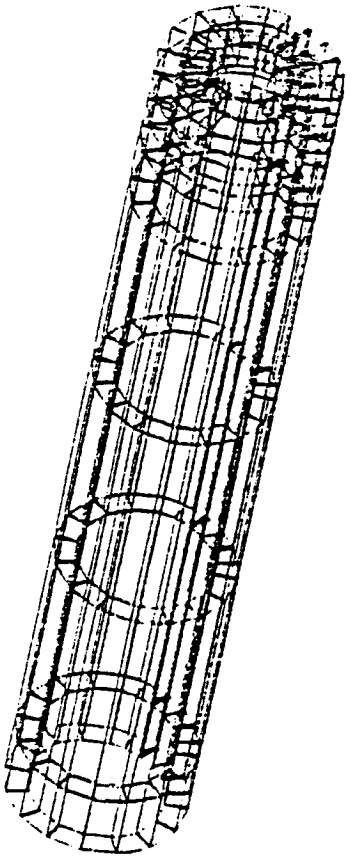

Fig. 3-8. The Elements of Pinion Shaft.

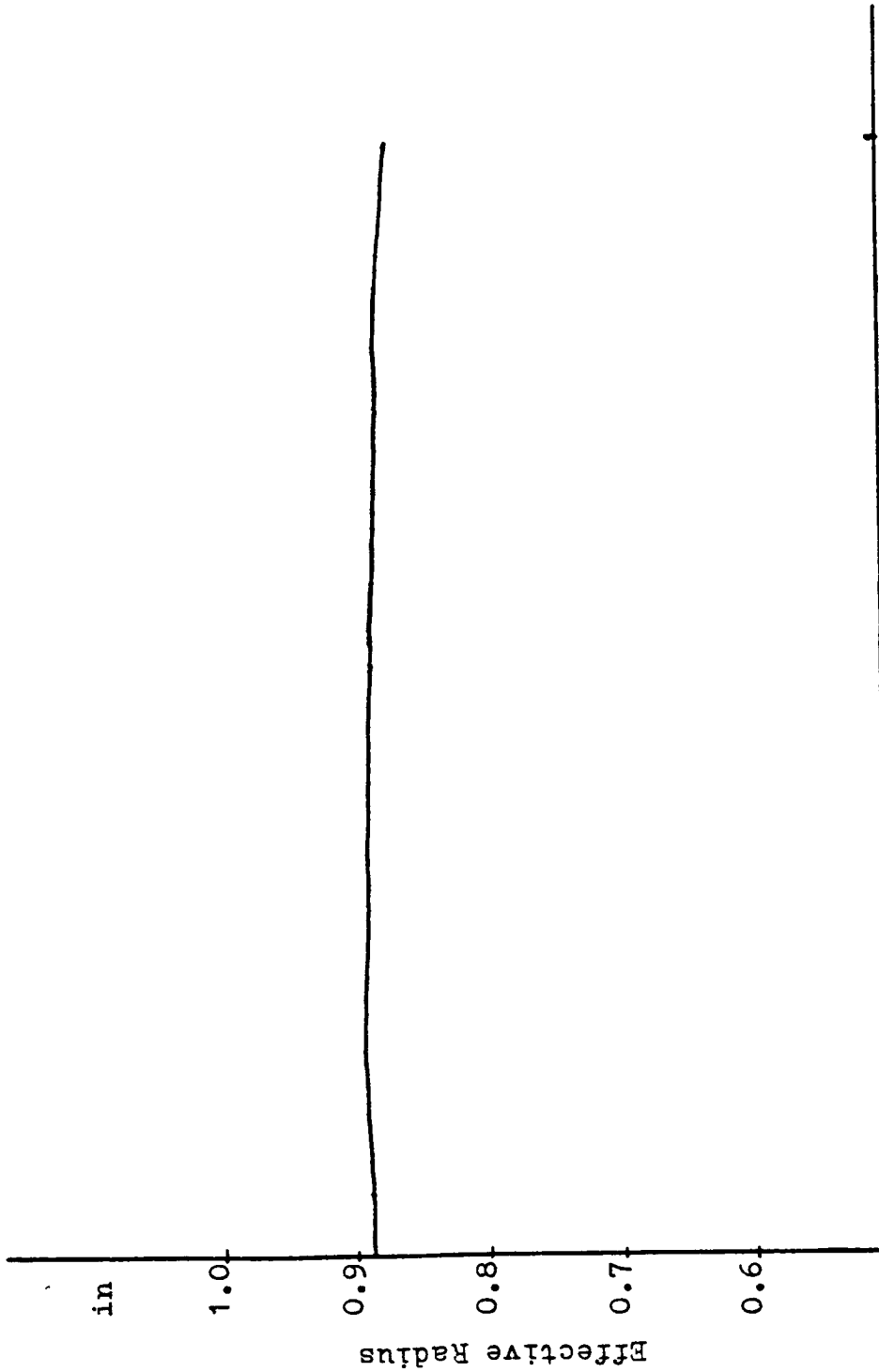

Fig. 3-9 variation of effective radius of pinion

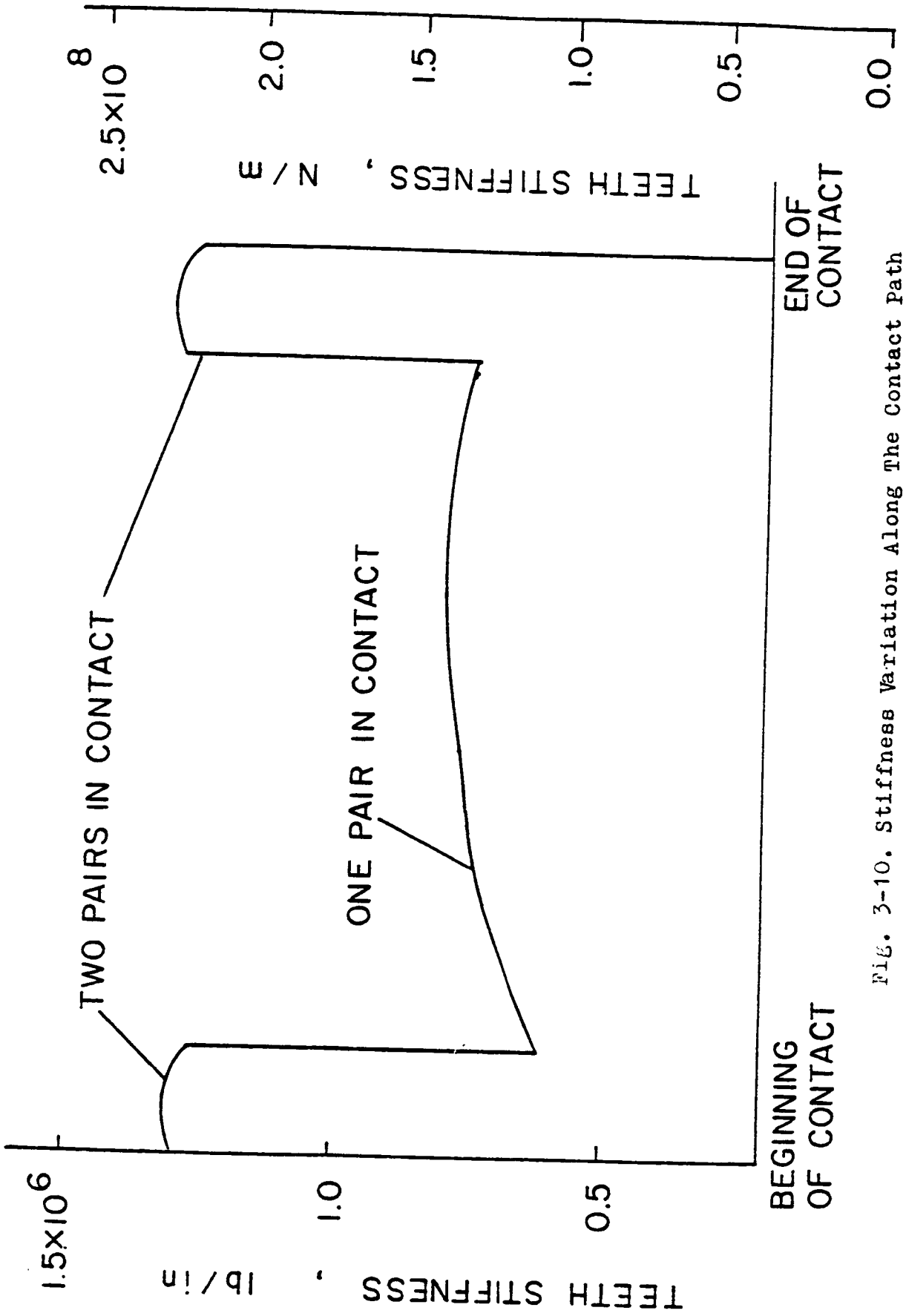

Fig. 3-10. Stiffness Variation Along The Contact Path

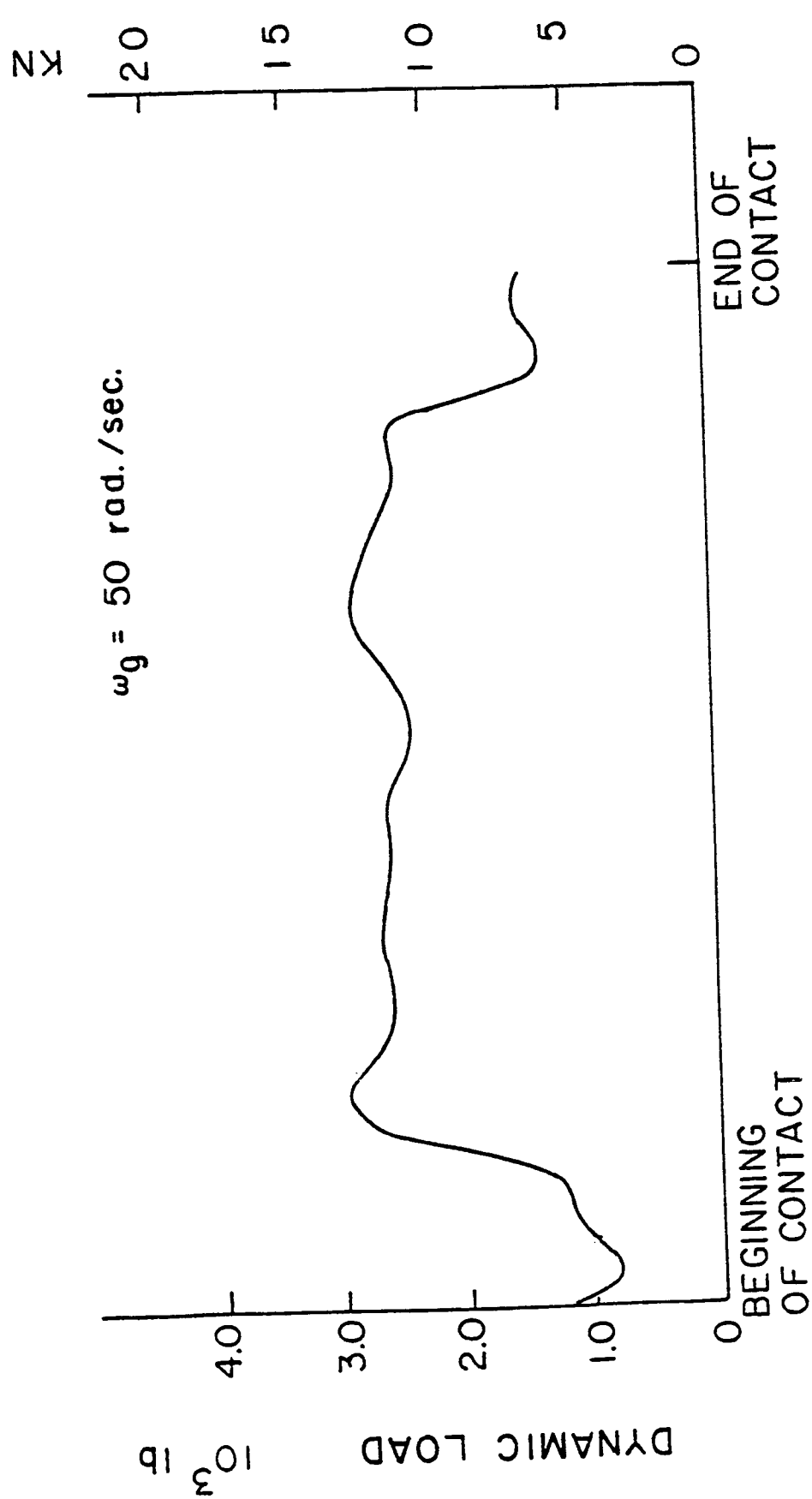

Fig. 3-11. Dynamic Load Variation Along The Contact Path at Gear Speed 50 rad/sec For Central Contact

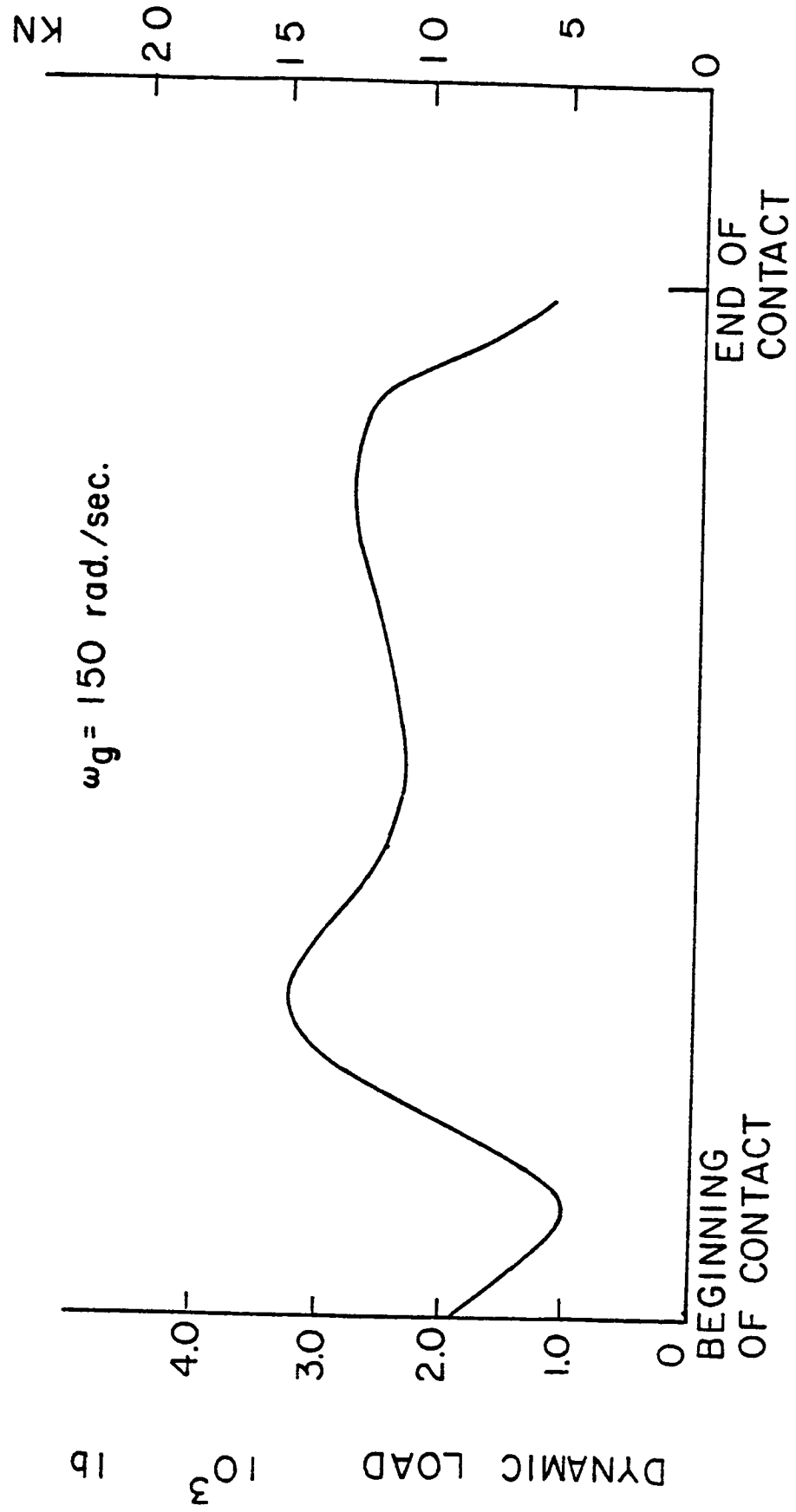

Fig. 3-12. Dynamic Load Variation Along The Contact Path at Gear Speed 150 rad/sec For Central Contact

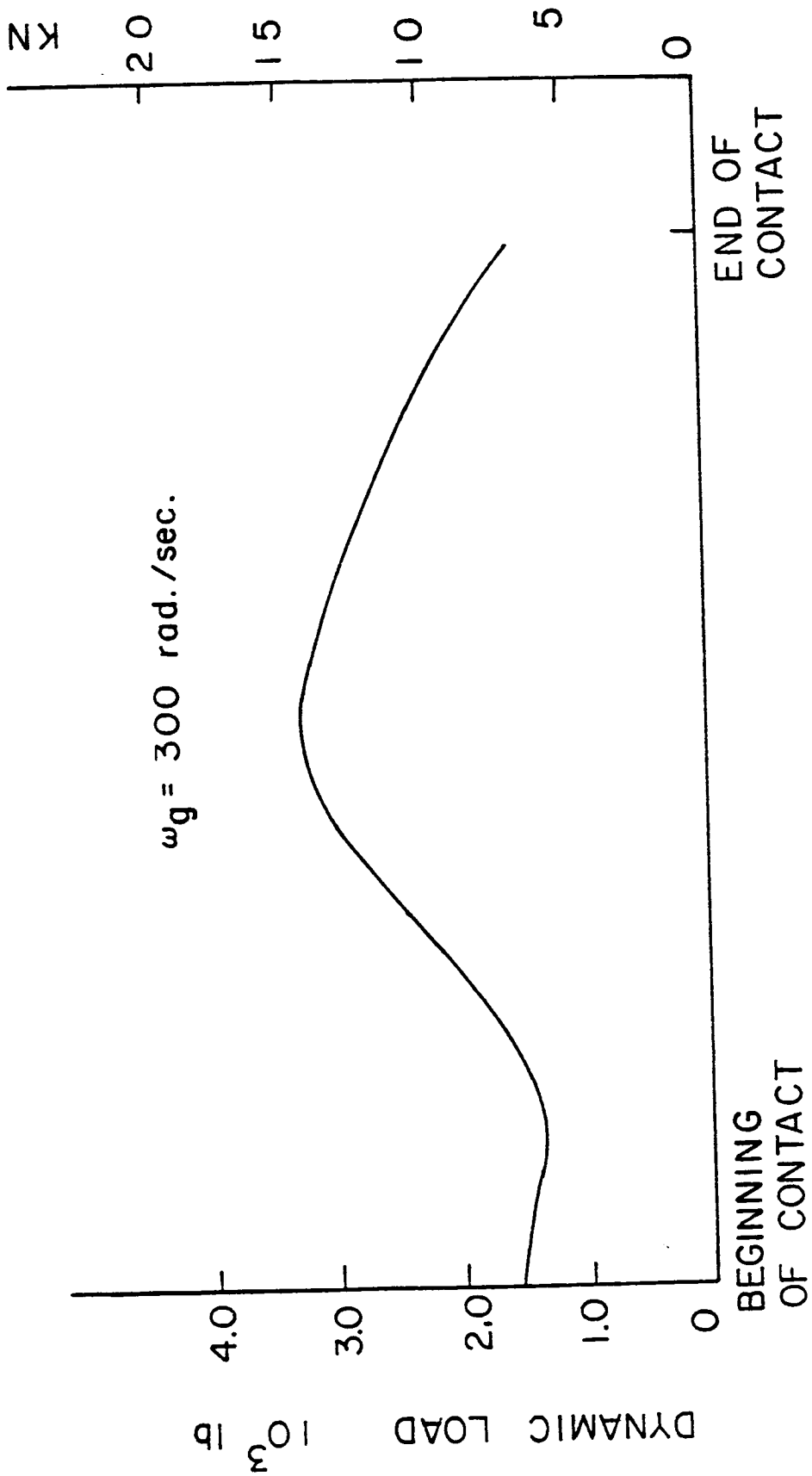

Fig. 3-13. Dynamic Load Variation Along The Contact Path at Gear Speed 300 rad/sec For Central Contact.

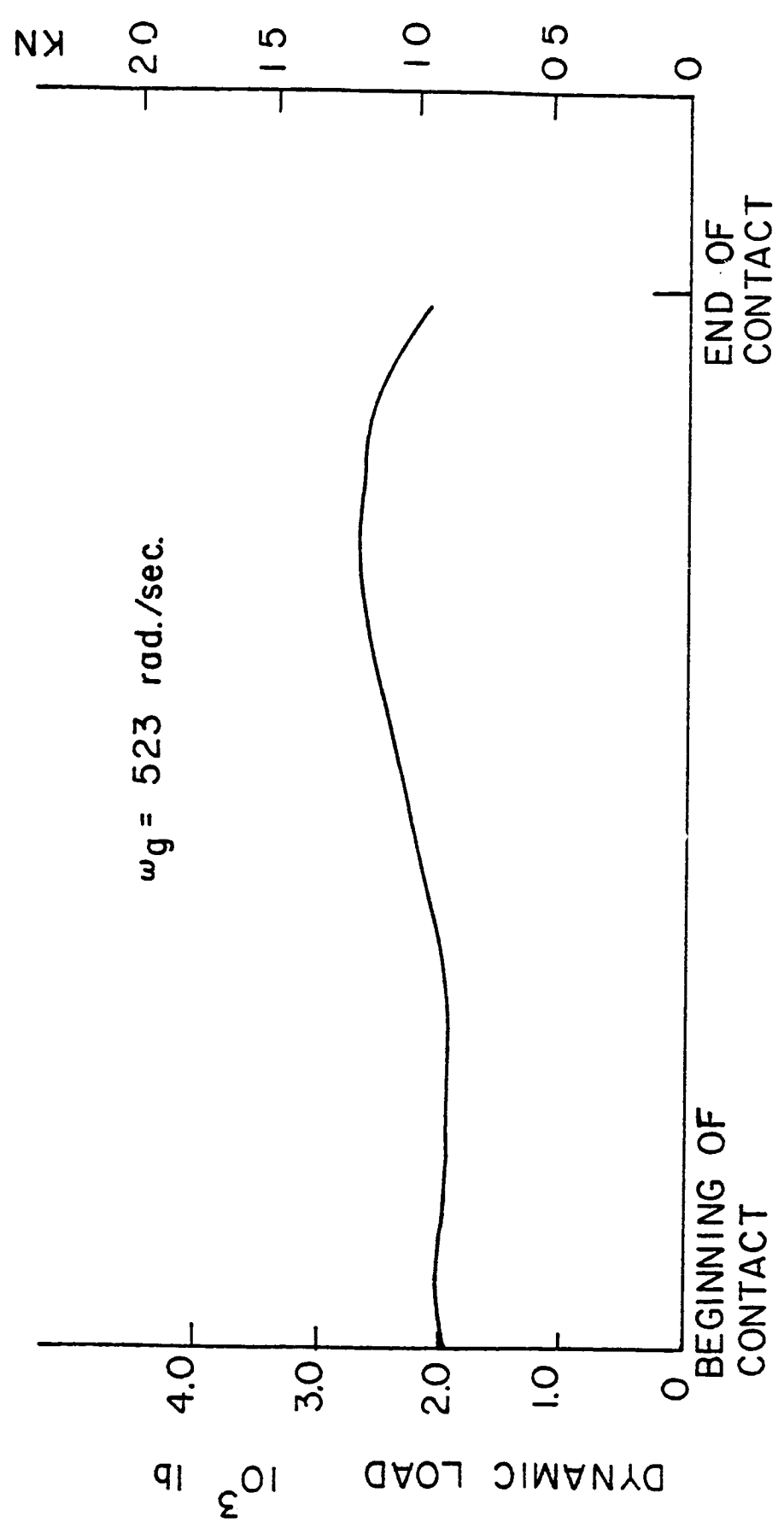

Fig. 3-14. Dynamic Load Variation Along The Contact Path at Gear Speed 523 rad/sec For Central Contact.

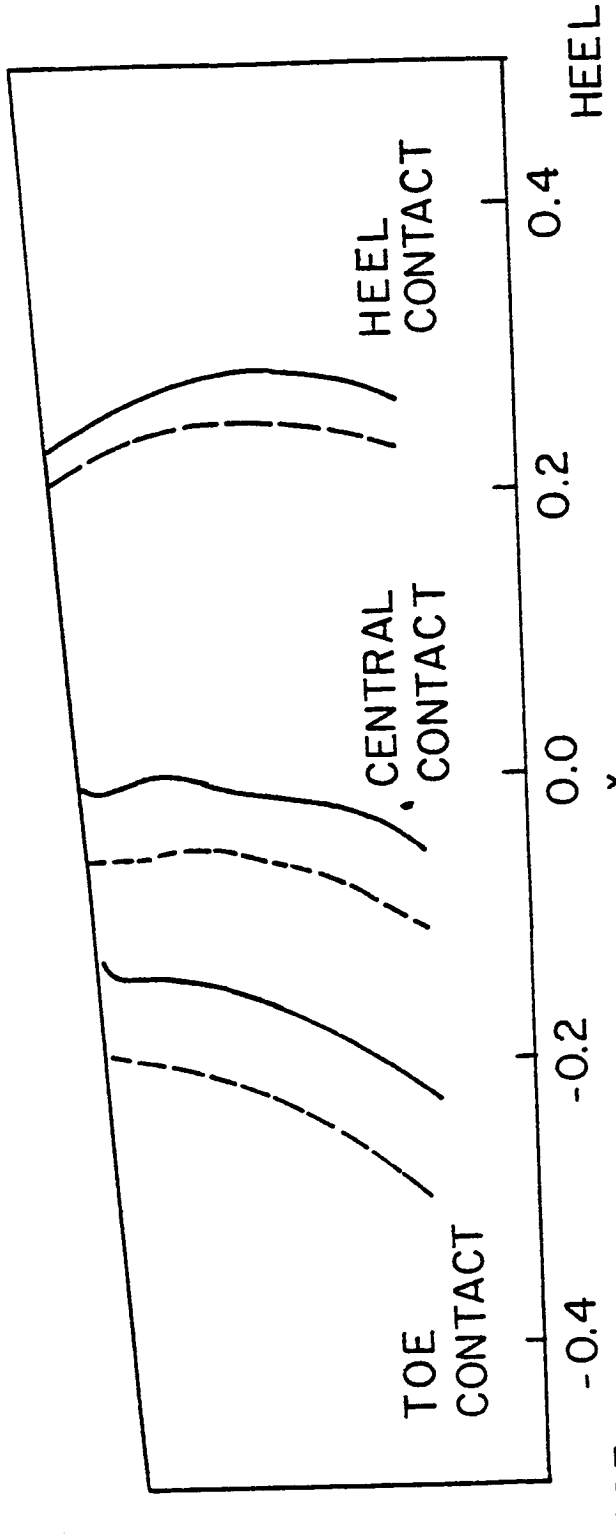

Fig. 3-15. Typical Contact Path of Central, Toe And Heel Contact
Dash Line For Contact Path Without Elastic Deformation;Solid Line for Contact Path With Elastic Deformation

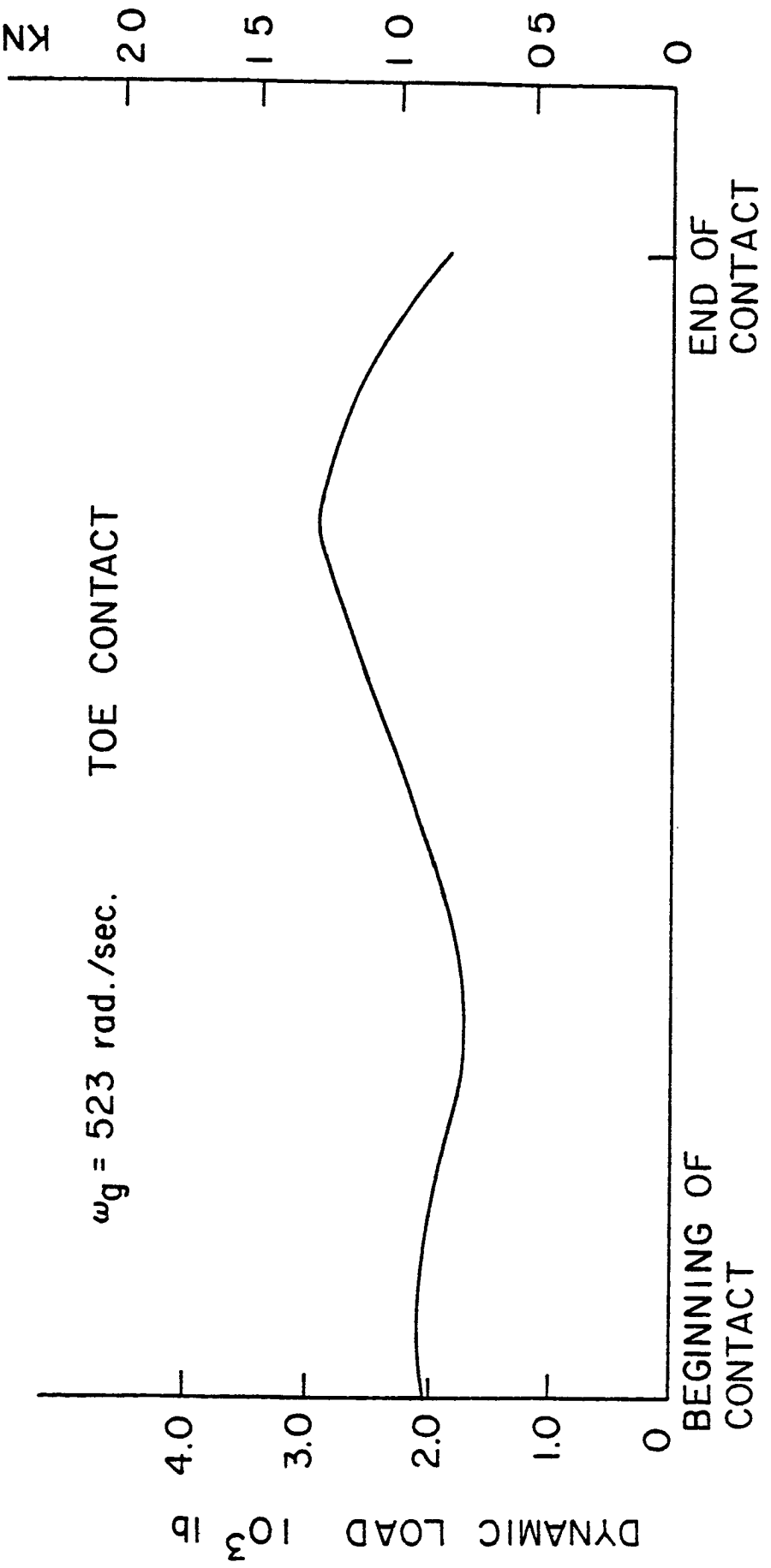

Fig. 3-16. Dynamic Load Variation Along Contact Path at Gear Speed 523 rad/sec For Toe Contact

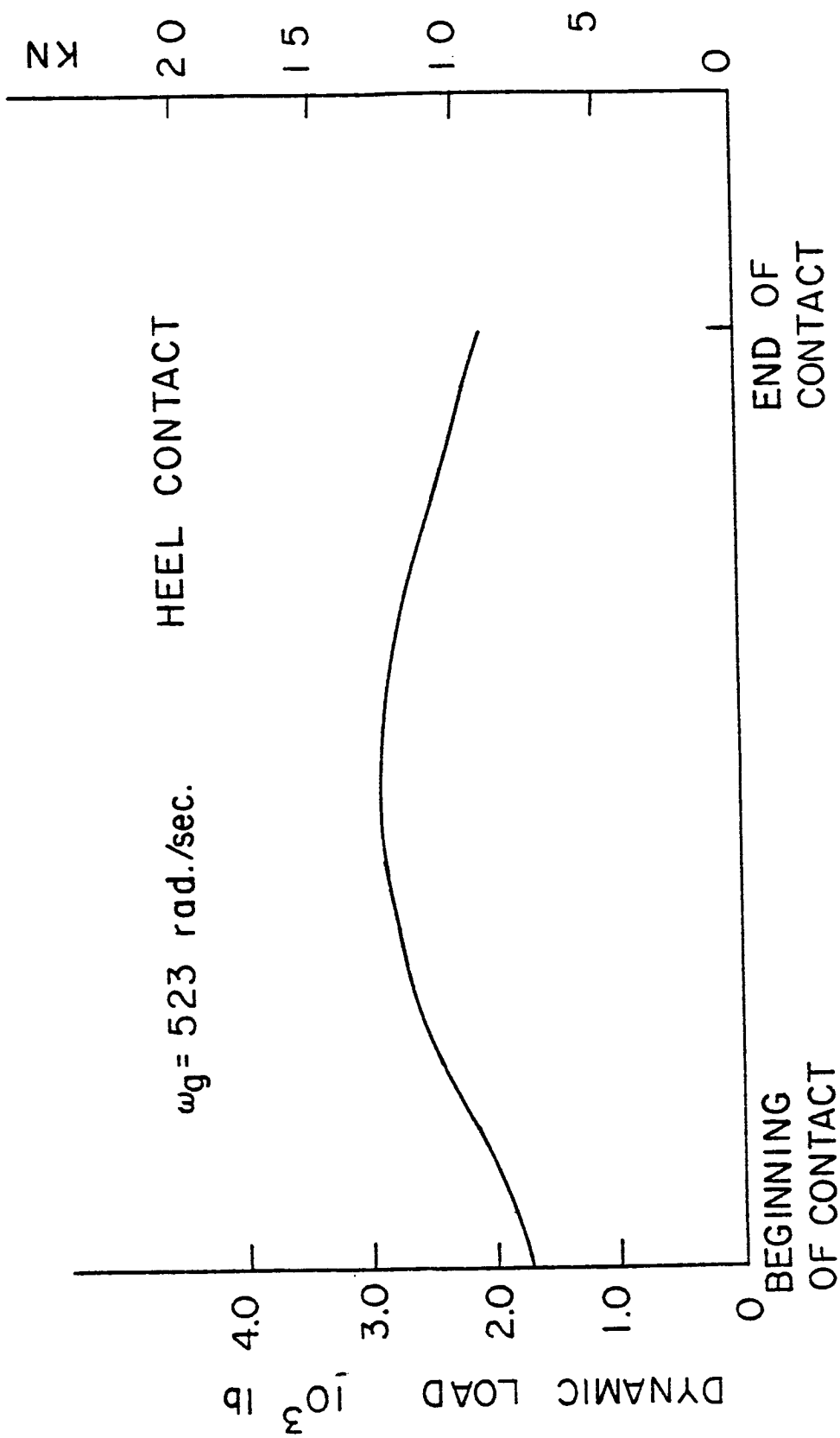

Fig. 3-17. Dynamic Load Variation Along The Contact Path at Gear Speed 523 rad/sec For Heel Contact

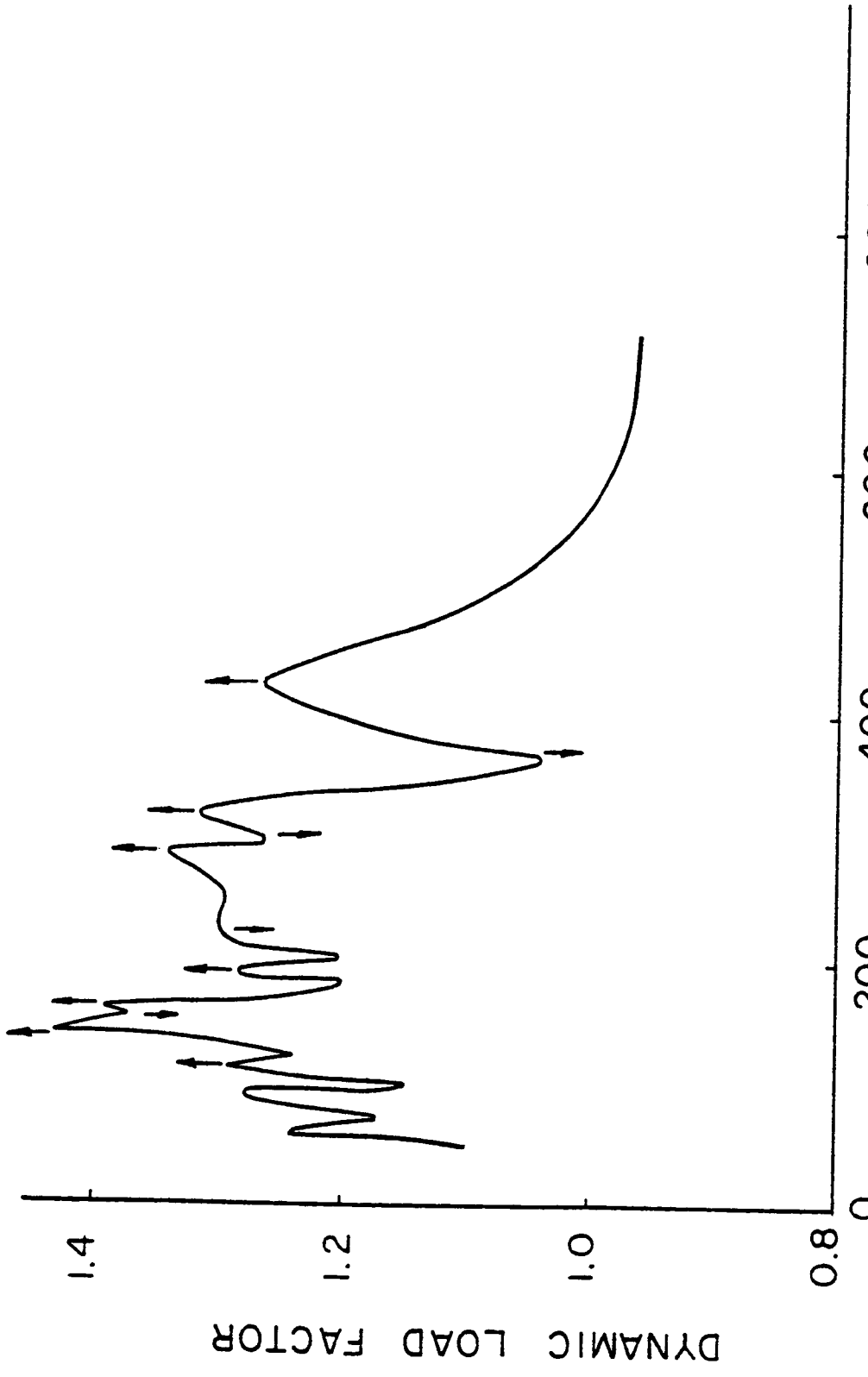

Fig. 3-18. Dynamic Load Factor is Plotted Against Gear Speed With All Damping Coefficients = 15 lbf • s/in Contact Ratio = 1.16

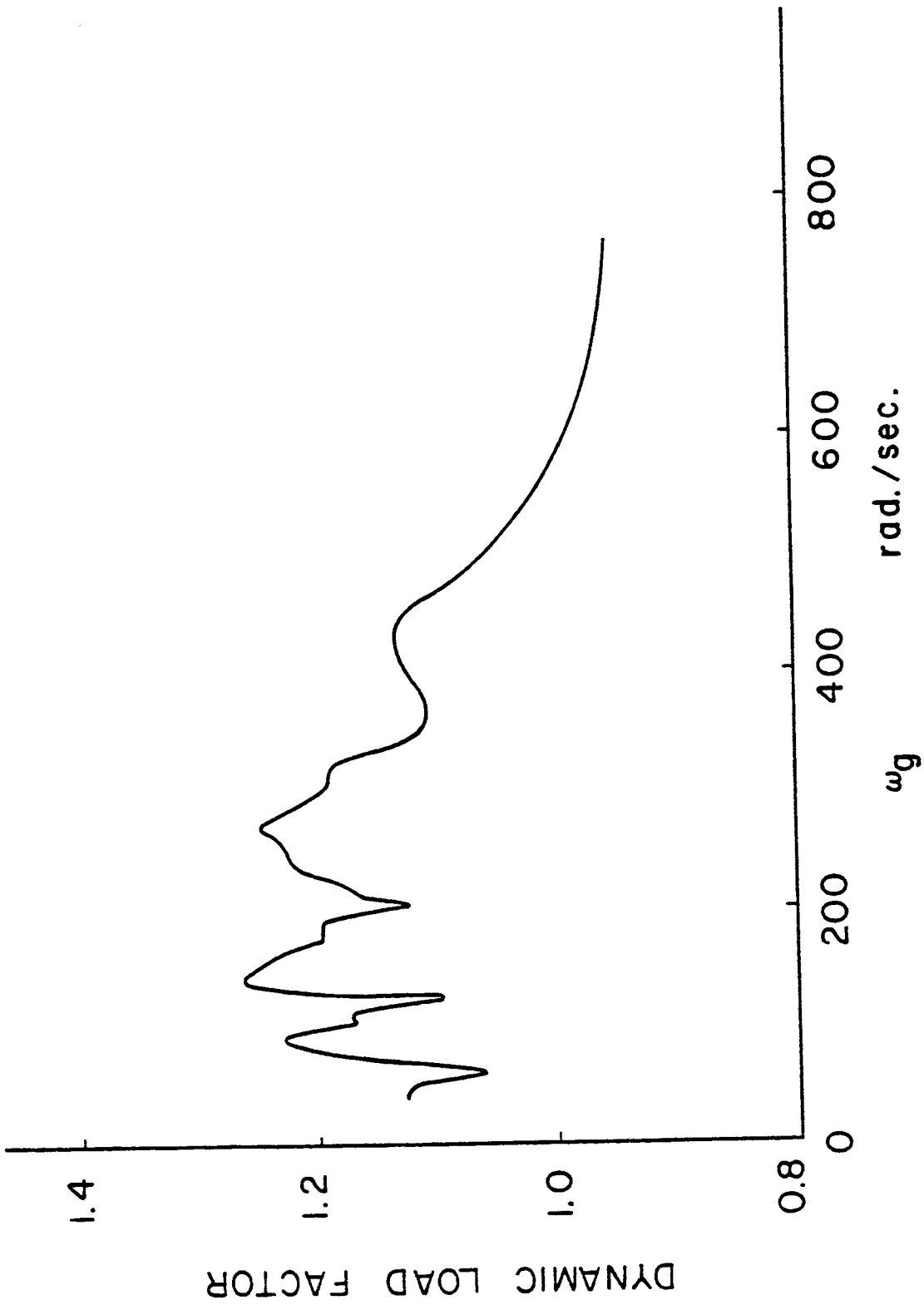

Fig. 3-19. (a) Dynamic Load Factor is Plotted Against Gear Speed With Contact Ratio = 1.16

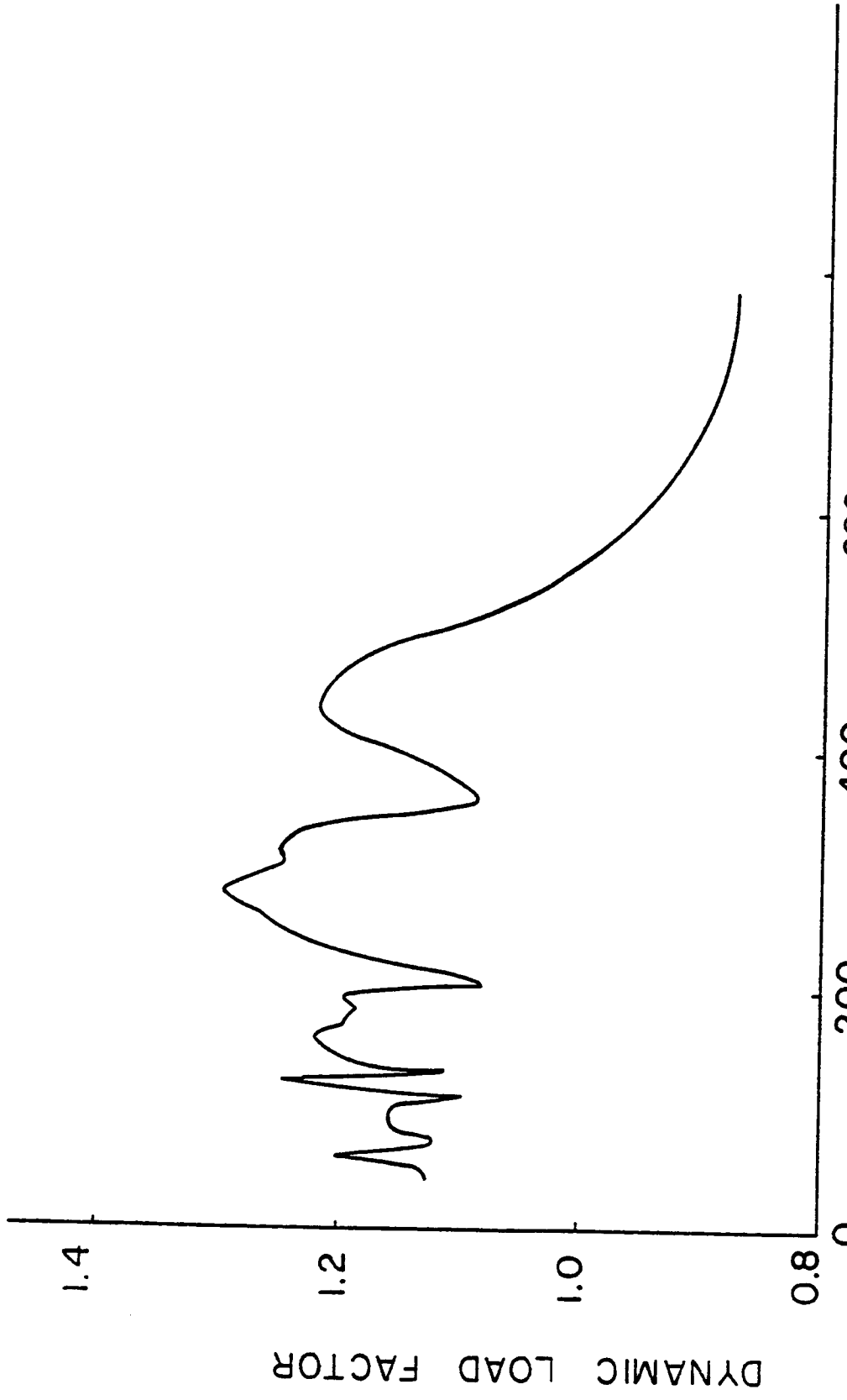

Fig. 3-19. (b) Dynamic Load Factor is Plotted Against Gear Speed With Contact Ratio = 1.33

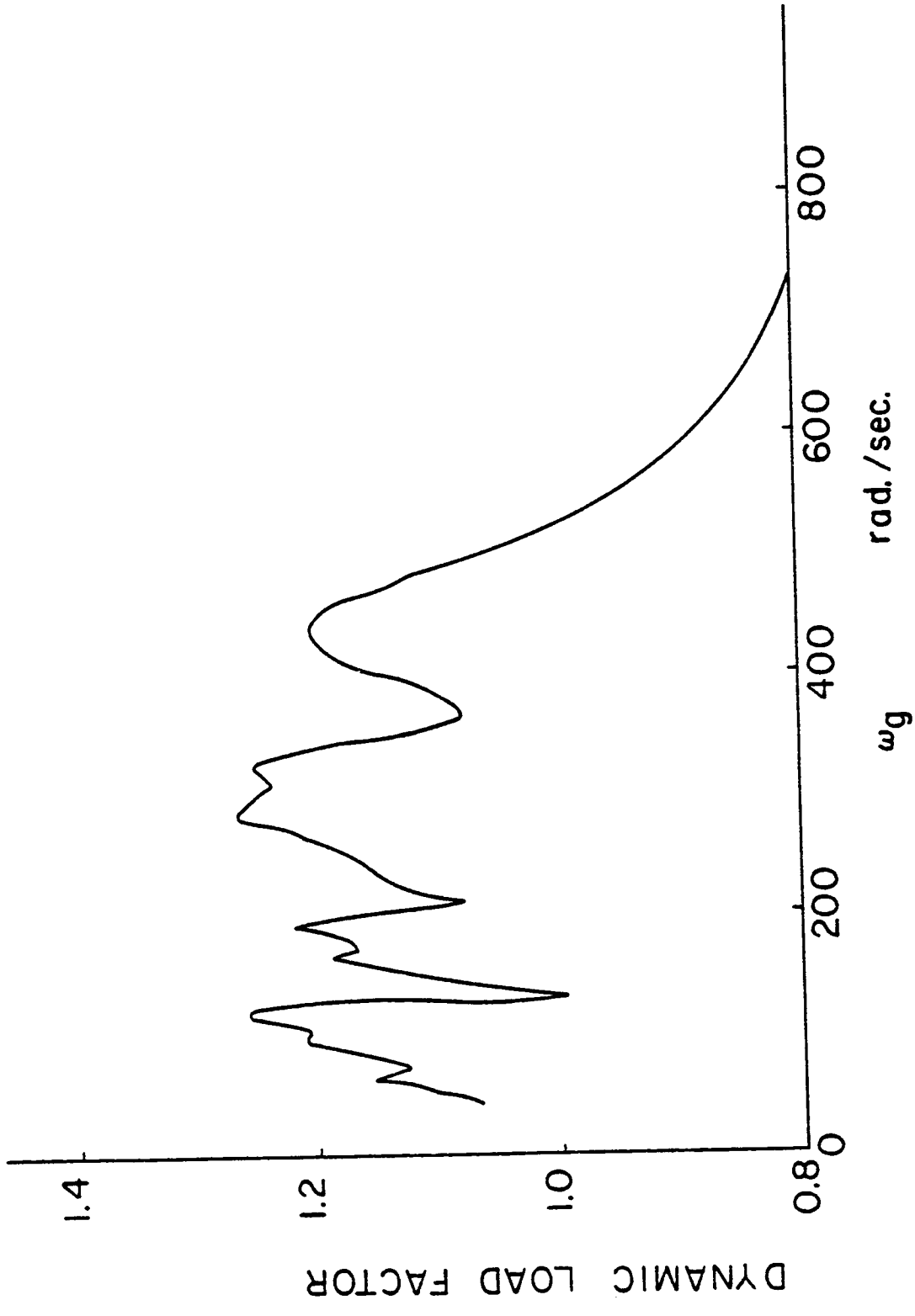

Fig. 3-19. (c) Dynamic Load Factor is Plotted Against Gear Speed With Contact Ratio = 1.72

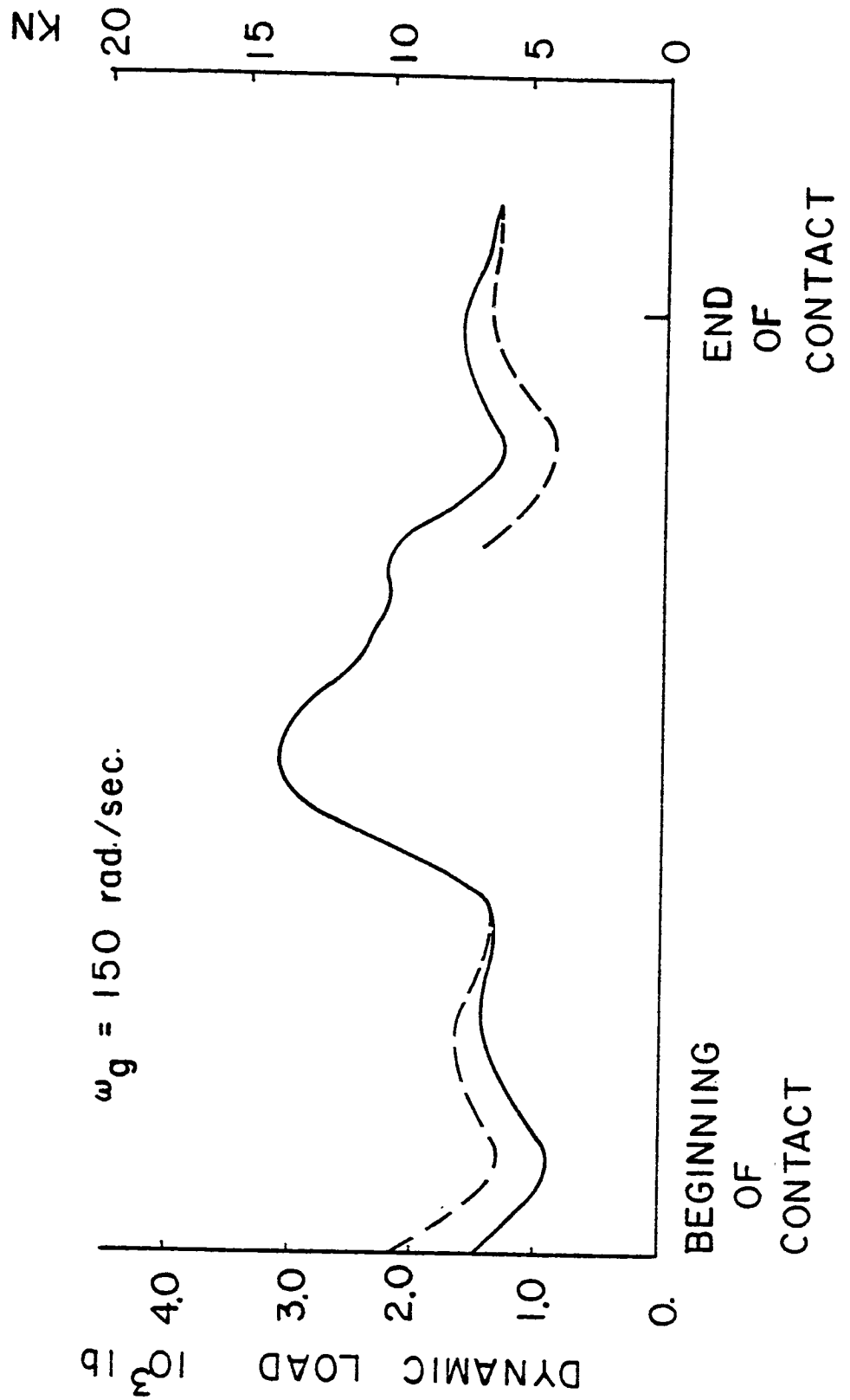

Fig. 3-20. Dynamic Load Variation With Contact Ratio = 1.72.

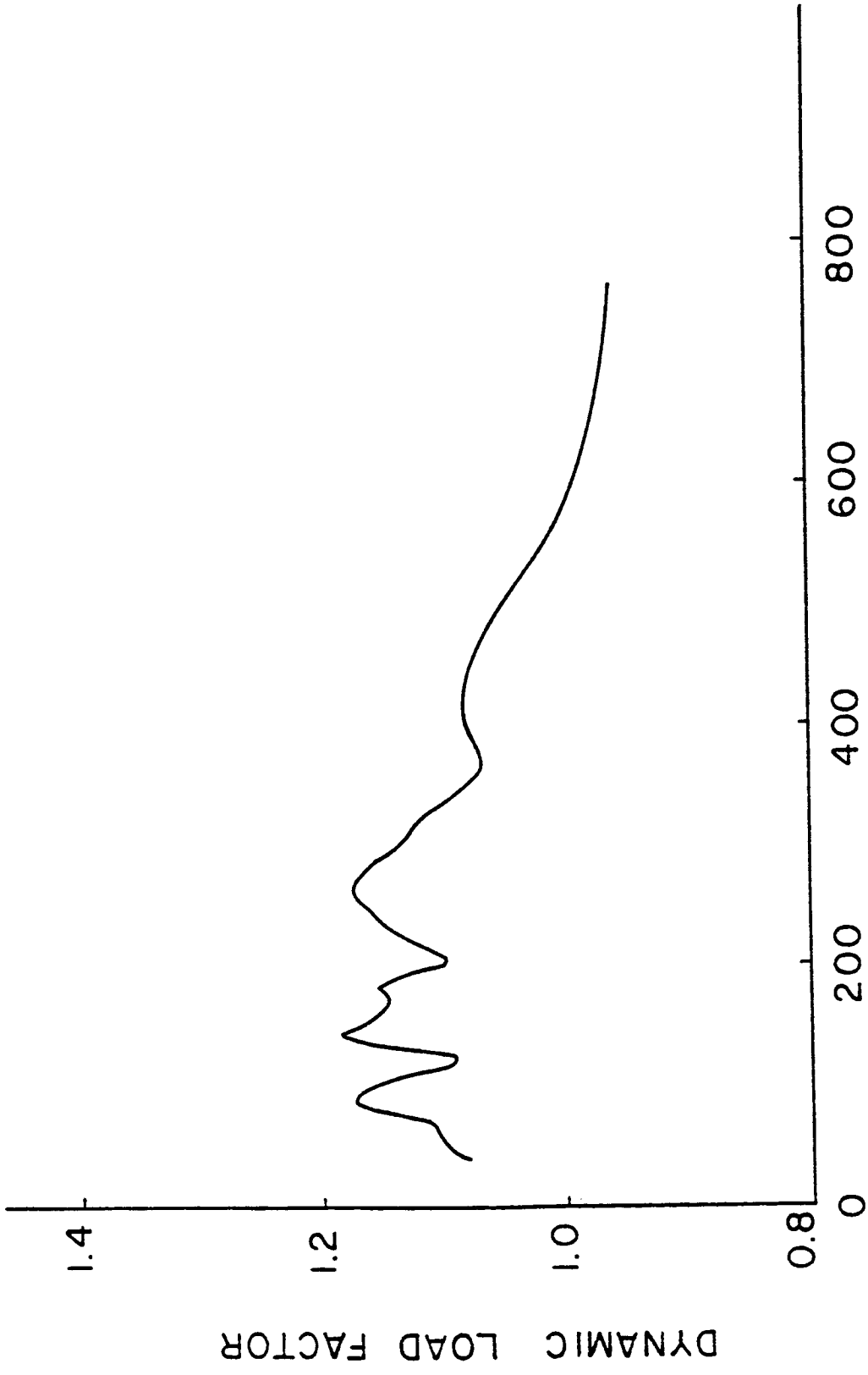

Fig. 3-21. Dynamic Load Factor is Plotted Against Gear Speed With All Damping Coefficients = 35 lbf • s/in and Contact Ratio = 1.16

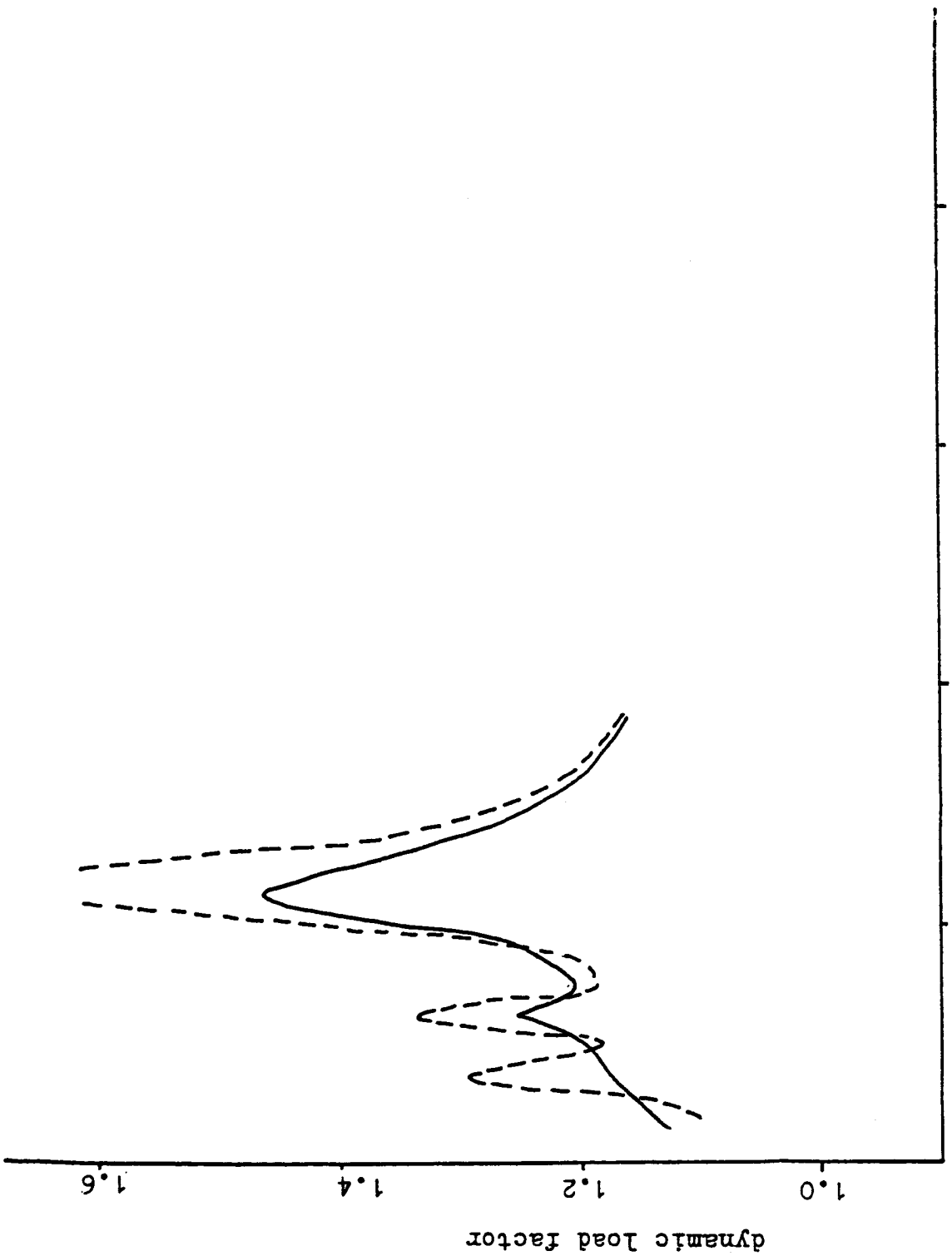

Fig. 3-22 Dynamic load factor is plotted against gear speed for rotational mode only with contact ratio=1.16 and different damping ratios (solid line 0.14 and dash line 0.058)

CHAPTER IV

LUBRICATION OF SPIRAL BEVEL GEARS

4.1 Introduction

One of the most important failure modes in lubricated machine elements is scuffing, which is where local wear occurs between the contacting elements when the lubricant fails to separate them and the protective thin surface film breaks down due to the high temperature. In gearing systems this failure is affected mainly by gear geometry, speed, load, and lubrication. For many years, the methods used to predict the surface capacity of gear systems depended on empirical formulas based on field experience. A major drawback in the application of the empirical methods is that they do not consider the effects of lubrication, which has been found to be of great importance in scuffing prediction. In recent years, the fully developed theory in elastohydrodynamic lubrication was successfully applied to spur and helical gears (9,52). Because of the geometric complexity of spiral bevel gears, an analysis covering all the possible factors to evaluate the risk of scuffing in lubricated spiral bevel gear drives has yet to be developed.

In this chapter, an analysis of the temperature and film thickness for spiral bevel gear teeth is performed. The bulk temperature is calculated by using the 3-D finite element method combined with a prescribed heat input. For the heavily loaded system, the limiting shear stress

depending on temperature and pressure is used to calculate the total heat generated over the whole contact ellipse. The average and maximum flash temperature in this contact ellipse is obtained by making a finite number of stripes. Each stripe is oriented along the direction of sliding velocity. It is assumed that the temperature profile along any stripe is the same as that of an infinitely long band heat source (in the direction perpendicular to sliding) whose width is equal to the stripe length and has the same heat flux profile along the stripe. The heat flux partition coefficient is calculated by assuming that the total heat is generated in the mid-plane of the lubricant film, and that there is no temperature jump in this plane. Hamrock-Dowson's equation is used to predict the film thickness between matching teeth. All quantities mentioned above, which include bulk temperature, flash temperature, traction coefficient and film thickness, are interdependent. They are solved as a system by an iterative method.

4.2 Flash Temperature

During meshing,each tooth face will show a temperature increase (flash temperature) due to the frictional heat developed at the surface as the contact area moves along the tooth face. This temperature rise is restricted to the instantaneous contact area and will disappear very rapidly as soon as the area of tooth face is out of contact. Usually, this temperature is very high and it is an important factor in gear scuffing.

The first successful prediction of flash temperature, done by Blok (13,14), was based on the heat conduction analysis of a semi-infinite body with a uniformly distributed moving heat source. J. C. Jaeger in 1942 (15) dealt with the problem of a moving source of heat with variable heat source and variable velocity. J. F. Archard (16) introduced a simple harmonic mean to obtain the interface temperature. A refined solution including a local heat partition coefficient between a pair of disks was derived by Cameron, et al. (17). More recently, Francis (18) made a further refinement in Blok's calculation by considering a variable heat flux in the contact.

The calculation of flash temperature is based on the assumption that the heat source passes over the surface of a semi-infinite solid. For spiral bevel gears, the area of sliding contact is formed by elastic deformation of curved tooth surfaces where, according to the classic equation of Hertz (19), the area of contact is elliptical. Archard (16) has shown that,when the dimensionless parameter $vR/a > \sim 10.0$ (where a is the thermal diffusivity, v is the sliding velocity and R is the nominal length), the heat flow in the direction perpendicular to sliding

may be neglected. The temperature distribution within a heat source of finite area can be determined by dividing the whole contact area into differential stripes parallel to the sliding direction. The temperature profile along any stripe is the same as that of an infinitely long band heat source (in the direction perpendicular to sliding) of width equal to the stripe length and having the same heat flux profile along the stripe.

The situation is illustrated in Fig. 4-1, which shows the contact heat flux distribution in an elliptical contact area with an angle α between direction of the velocity of heat flux (sliding velocity) and semi-minor axis of this area. Letting the equation $(X/AMAX)^2 + (Y/BMAX)^2 = 1$ describe this elliptic contact, the length ℓ of a stripe containing point (x,y) in the contact is

$$YA = BMAX^2 \tan^2 \theta + AMAX \tag{4.1}$$

$$YB = \tan \theta \; BMAX^2 \; x_i - y_i \; BMAX^2 \tan^2 \theta \tag{4.2}$$

$$YC = BMAX^2 \tan^2 \theta \; y_i^2 - 2 \tan \theta \; BMAX^2 \; x_i y_i + BMAX^2 \; x_i^2 - AMAX^2 \; BMAX^2 \tag{4.3}$$

$$y_1^{+,-} = \frac{- YB \pm \sqrt{YB^2 - YA \; YC}}{YA} \tag{4.4}$$

$$x_i^{+,-} = \tan \theta \; (y_i^{+,-} - y_i) + x_i \tag{4.5}$$

$$2\ell = \sqrt{(y_i^+ - y_i^-)^2 + (x_i^+ - x_i^-)^2} \tag{4.6}$$

The center of this stripe is

$$x_{io} = 0.5\ (x_i^+ + x_i^-) \tag{4.7}$$

$$y_{io} = 0.5\ (y_i^+ + y_i^-) \tag{4.8}$$

The dimensionless parameter u is defined as

$$u = \pm \sqrt{(x - x_{io})^2 + (y - y_{io})^2} \Big/ \ell \tag{4.9}$$

If (x,y) is in the forward position of this stripe (upstream of the sliding velocity), u is positive; otherwise, u is negative. The temperature at this point can be obtained by using the equation developed by Jaeger (15) for the temperature distribution along a stripe for a larger value of $v\ell/a$.

$$T(x,y) = \frac{2q}{k}\left[\frac{a(\ell-u)}{\pi v}\right]^{1/2} \tag{4.10}$$

where k is the thermal conductivity and q is a constant heat flux (the reason for using a constant heat flux will be shown later) Cameron, et al. (17) showed that, for a uniform source, the temperature profile is given almost exactly for $10 < v\ell/a < \infty$ by multiplying the asymptotic ($v\ell/a \sim \infty$) factor $1 + (2\ell/\ell-u)^{0.5}[0.65\ (a/v\ell) + 0.44\ (a/v\ell)^{3/2}]$, and the temperature profile becomes

$$T(x,y) = \frac{2q}{k}\left[\frac{a(\ell-u)}{\pi v}\right]^{0.5}\left\{1+\left[\frac{2\ell}{\ell-u}\right]^{0.5}[0.65(a/v\ell) + 0.44(a/v\ell)^{3/2}]\right\} \tag{4.11}$$

This factor will increase the maximum temperature and moves it toward the center of the stripes as $v\ell/a$ decreases. Even if $v\ell/a < 10$, which occurs in the outer stripes of the contact ellipse, the equation can still be used because (1) the correction factor will hold approximately for $v\ell/a < 10.0$, and (2) the outer stripes are only a small fraction of the area of the heat source. Thus, there will be a minimal effect on the temperature in the whole contact area.

Heat is generated by viscous shearing of the lubricant between the sliding surfaces. This heat is carried away either by the lubricant through convection or by the gear blanks through conduction. The relative importance between these two modes of heat transfer in EHD contact was examined by Trachman (20). He concluded that the heat carried away by heat convection can be neglected in comparison to the heat diffused to the gear body, except at very high speeds which exceed those of gears in current practice. Let the subscripts 1 and 2 denote the pinion and the gear, respectively. The heat generated in the contact area is divided betwen the pinion and the gear by the ratio $\alpha/(1-\alpha)$, where α is the heat partition coefficient. Therefore, within the contact, the temperature distribution in the pinion and the gear are

$$T_1(x,y) = \alpha\frac{2q}{k_1}\left[\frac{a_1(\ell_1-u_1)}{\pi v_1}\right]^{0.5}\left\{1+\left[\frac{2\ell_1}{\ell_1-u_1}\right]^{0.5}[0.65(a_1/v_1\ell_1) + 0.44\ a_1/v_1\ell_1)^{3/2}]\right\} \tag{4.12}$$

$$T_2(x,y) = (1-\alpha)\frac{2q}{k_2}\left[\frac{a_2(\ell_2-u_2)}{\pi v_2}\right]^{0.5}\left\{1+\left[\frac{2\ell_2}{\ell_2-u_2}\right]^{0.5}[0.65(a_2/v_2\ell_2) + 0.44(a_2/v_2\ell_2)^{3/2}]\right\} \quad (4.13)$$

The lubricant local velocity profile and temperature profile for the very high sliding velocity case were estimated by Plint (21) and later confirmed by Trachman's analysis (20). For sliding contacts, their results showed a sharp S-shape velocity profile across the film with a large velocity gradient at the mid-plane. The temperature is at it's maximum at the mid-plane and decreases almost linearly to both surfaces. Since shearing of the lubricant occurs mainly in the mid-plane, most of the heat is also generated in this layer. This results in a triangular temperature distribution across the film.

According to Francis' analysis (18), if the bulk surface temperatures for the pinion and the gear, T_{B1} and T_{B2}, are different (see Fig. 4-2), then the interfacial temperature can be expressed

$$(\alpha+\Delta\alpha)\left[T_1+\frac{Z_m q}{k_o}\right]+T_{B1} = T_{mid}(x,y)$$

$$= (1-\alpha-\Delta\alpha)\left[T_2+\frac{(h-Z_m)q}{k_o}\right]+T_{B2} \quad (4.14)$$

where $\Delta\alpha$ is the unknown function of (x,y) which expresses the local deviation from heat flux distribution αq and $(1-\alpha)q$, Z_m is the distance from pinion surface to the layers at which all the shear

is concentrated ($Z_m = \frac{h}{z}$), k_o is the oil thermal conductivity, and $T_{mid}(x,y)$ is the temperature at the shear plane. Then

$$(\alpha + \Delta\alpha)\left[T_1 + \frac{hq}{2k_0}\right] + T_{B1} = (1 - \alpha - \Delta\alpha)\left[T_2 + \frac{hq}{2k_o}\right] + T_{B2} \qquad (4.15)$$

$$\Delta + \Delta\alpha = \frac{T_2 + hq/2k_o + T_{B2} - T_{B1}}{T_1 + T_2 + hq/k_o} \qquad (4.16)$$

$$T_{mid}(x,y) = \frac{T_2(x,y) + hq/2k_o + T_{B2} - T_{B1}}{T_1(x,y) + T_2(x,y) + hq/k_o}\left[T_1(x,y) + \frac{hq}{2k_o}\right] + T_{B1} \qquad (4.17)$$

The heat partition coefficient α must now be determined to calculate the flash temperature of pinion and gear. The analytical expression for α in terms of local conditions is difficult. The best approximation of α will be the value that satisfies the condition for which the temperature fields of the two surfaces are identical over the contact ellipse. Thus, an analytical approximation can be written by equating the mean temperature of the two surfaces, as done by Jaeger (15)

$$\alpha\left[T_{1,ave} + \frac{Qh}{2k_o}\right] + T_{B1} = (1 - \alpha)\left[T_{2,ave} + \frac{Qh}{2k_o}\right] + T_{B2} \qquad (4.18)$$

where

$$T_{1,ave} = \frac{\iint T_1(x,y)dxdy}{\pi \text{ AMAX BMAX}} \tag{4.19}$$

$$T_{2,ave} = \frac{\iint T_2(x,y)dxdy}{\pi \text{ AMAX BMAX}} \tag{4.20}$$

Q is the total heat flux over the whole contact ellipse. Once the α is determined, the flash temperatures become

$$T_{1,f}(x,y) = \alpha T_1(x,y) + T_{B1} \tag{4.21}$$

$$T_{2,f}(x,y) = (1-\alpha)\ T_2(x,y) + T_{B2} \tag{4.22}$$

4.3 Bulk Temperature

The method mentioned in Section 4.2 is for calculating, with known heat flux, the flash temperature rise above the surface temperature which was assumed known beforehand. The existing criteria for scuffing of heavily loaded gears is that the total surface temperature rises to a critical value at which the oil film collapses, the protective surface layer breaks and metal to metal contact occurs. Uncertainty in the bulk surface temperature makes any scuffing prediction useless even if an accurate calculation of flash temperature can be calculated.

Before the gear system starts to operate, all elements are at the ambient temperature. Once the gear system starts to operate, the temperature builds up as the gears are running due to frictional heat. After a sufficient period, the gear surface temperatures reach a steady state at which the heat flux flowing into the body is equal to that flowing out of the body. At each revolution, the tooth is subject to the same heating flux. Since the time period for each contact point in the contact zone is only a small fraction of the entire period of revolution, the local temperature jump (flash temperature) has completely decayed before it enters into the contact zone at the next revolution. Thus, it is justified to use an average heat input over the revolution to calculate the steady-state temperature rise of the body.

The heat input is due to the heat generated at the instantaneous contact ellipse, and the amount depends on the load and the viscous shearing of the lubricant. The heat flux flowing out of the body is due to the heat convection to the surrounding air and lubricant. The relative importance of the heat transfer coefficient at different surface areas was discussed by Patir (22) and Townsend and Akin (23) in spur gear

systems. They also revealed the significant effect on temperature distribution by the lubrication method. In this study, the oil jet impingement depth is assumed to cover the whole area of contact side, which can be obtained by using the proper pressurized oil jet. Estimated values of the heat transfer coefficients are used on the other surface areas to calculate the bulk temperature.

A three-dimensional finite element program is used to calculate the temperature coefficient. The mesh of the system includes the gear shaft, gear body and the contact tooth with one adjacent tooth on both sides. The eight-node element is used. This model is the same as that used for the deflection coefficient except that the boundary conditions are different. In the temperature analysis, all the surfaces are subject to heat convection with different heat transfer coefficients except for the surface in the inner cylinder of the shaft, which is assumed to have no heat convection. The inner cylinder of the gear, created for the modeling, is very small in radius, therefore heat transfer can be neglected for these surfaces. Since the air in the inner cylinder of the pinion shaft is enclosed, there is no heat loss or gain in the steady state, and the heat convection at this surface can also be neglected. The heat transfer coefficient h_j is assigned to the contacting tooth face which is oil jet cooled. The topland and bottomland of the tooth and the other side of the tooth surface, which are not cooled by the oil jet, will have a heat transfer coefficient h_t for air or air/oil mist. Since only three teeth are made in the model, there is a surface region A covering the surfaces where the teeth are taken off and the bottomland between those teeth. The heat transfer coefficient at this region A is

given a value of h_j, which is the same as that of the surface coefficient cooled by the oil jet. The reason is that there is an oil jet cooled surface on each tooth and most of the heat will flow out of the tooth through this surface ($h_j >> h_t$). All the other convective surfaces of the gear system are given a coefficient h_s (Fig. 4.3). The theoretical estimated values of h_s and h_j can be found in (Refs. 24 and 25). However, the estimated values of h_s, h_j and h_t based on the experimental results are used in this study (23).

Thirty nodes are created on the contacting surface. The temperature distribution on this surface is represented by T_{JI} which is the temperature at the grid node J due to a unit heat flux at node I. By interpolation, the temperature at any contact point M due to a unit heat flux at the contact point N (T^C_{MN}) can be obtained in terms of T_{JI}. The details of this interpolation can be found in Appendix D. Once the contact path is located and the heat flux flowing into each body at each contact point has been calculated, the bulk temperature at the contact point M can be found as

$$T_{M,B} = \Sigma\ T^C_{MN}\ Q_N \qquad N = 1...KMAX \qquad (4.23)$$

where KMAX is the total number of contact points along the contact path.

4.4 Traction Coefficient

In analyzing lubrication related failure mode in EHD contacts, the heat generated by traction in the contact area is the main concern. In a conventional analysis, the rheology of the lubricant is ignored and the local shear stress in the contact area is assumed to be proportional to the local pressure and acts in the direction opposite to the local slip. However, recent research into the shear behavior of EHD makes it possible to examine the role of the fluid rheology.

The magnitude of the coefficient of friction in a highly loaded disk machine was examined by Misharin (26) at high rolling and sliding speeds. He also gave an approximated formula for the prediction of the friction coefficient based on his experimental data. But his formula did not give realistic results at a very high or very low value of the rolling or sliding speeds. Smith (27) presented a set of results that showed that the friction coefficient would increase to a maximum and then decrease as the sliding speed is increased. He pointed out that the decrease of the friction coefficient was due to thermal and non-Newtonian effects.

The thermal effect upon the viscosity of lubricant was examined by Crook (28,29) and by Cheng (30). Crook used a disk machine to study rolling friction and sliding friction. He observed that the plot of traction against slip always showed a same kind of characteristic pattern as that which was found by Smith (27) regardless of the variation of load and speed. He also attempted to predict the traction analytically by simplified friction theory based on the following assumptions: The film thickness in the contact area is uniform; the pressure distribution in the contact area is Hertzian; the heat carried away by convection through the lubrican

is neglected; and the temperature rise on the surface is neglected. His method can predict a traction coefficient consistent with experimental data in high sliding region. However, he could not explain the behavior in low sliding region. Cheng used a thermal EHD theory which included energy equation and was free of all the assumptions made by Crook. Cheng's results, compared with Crook's experimental data, still showed a big difference in friction coefficient in the low sliding region. Both works suggested that the thermal effect alone cannot account for the sharp reduction of the effective viscosity in the low sliding region.

A pioneering effort was made by Dyson (31). He studied various experimental data and found that the curve of traction coefficient, when plotted against sliding speed, can be divided into three regions (Fig. 4-4). Region I is the linear region which shows the characteristic behavior of a Newtonian fluid. Region II is the nonlinear region which shows nonlinear variation of the traction coefficient with the shear rate, and region III is the thermal region which is dominated by the thermal effect on the shear stress of the lubricant. The fluid behavior in region I is shown to be explainable on the basis of linear viscoelasticity. In region II, the viscosity will decrease when the material undergoes a steady continuous shear with large strain. Dyson (31) and Gruber and Litvitz (32) suggested that the nonlinear behavior of the traction curve is due to this effect. At a high pressure, the relationship between stress and strain for the fluid is nonlinear; several equations were developed to describe this nonlinear behavior. Bell, Kannel and Allen (33), Hirst and Moore (34) used a "sinh" relation, and Trachman and Cheng (35) used a hyperbolic model. Observing that the traction force never

seems to exceed one tenth of the normal load, Smith (36), Johnson and Cameron (37), and Plint (38) proposed that the lubricant film would fail to retain a very high shear stress at extremely large strain rate, and shears like a plastic solid.

More recent work on the rheological experiment was done by Johnson and Roberts (39). They observed that the liquid-solid transition was occurring in EHD contact and the transition point was dependent on temperature and pressure. The same observations were made by Johnson and Tevaarwerk (40) and Bair and Winer (41,42). Johnson and Tevaarwerk (43) then developed an elastic-perfect plastic solid model for the traction drive analysis. Based on their experimental results, most recently Bair and Winner (44) proposed the following model to predict the lubricant behavior over the whole range of visco-elastic-plastic change.

4.4.1 Bair-Winner Model

Bair and Winner fabricated an apparatus to measure the viscosity of the lubricant at high strain rates and a large shear stress similar to those in an EHD contact. They found that the lubricant under high pressure exhibits a classical visco-elastic behavior for small strain. For large strain and large stress, the lubricant behaves like a material having a limiting yield shear stress. For lubricant under a more moderate pressure but large strain, the result is that the shear stress is smaller and the lubricant is viscous.

From their experimental results for 5P4E Santotrac-50 at large strain, the relationship of the dimensionless shear stress and the dimensionless shear rate can be described reasonably well with a single

natural log function. The dimensionless shear stress $\hat{\tau}$ is defined as the actual shear stress $\tau(P,T)$ divided by the limiting shear stress $\tau_L(P,T)$, and the dimensionless shear rate $\hat{\dot{\gamma}}$ is the actual shear rate $\dot{\gamma}$ multiplying by the viscosity $\mu_o(P,T)$ and divided by the limiting shear stress $\tau_L(P,T)$. $\tau(P,T)$, $\tau_L(P,T)$ and $\mu_o(P,T)$ are all pressure and temperature dependent.

This natural log function can be expressed by

$$\hat{\dot{\gamma}} = - \ell n(1 - \hat{\tau}) \tag{4.24}$$

which governs the nonlinear viscous flow.

Based on the conventional Maxwell visco-elastic model, the total shear rate of the lubricant consists of the shear rate of elastic part $(\hat{\dot{\gamma}}_e)$ and that of the viscous part $(\hat{\dot{\gamma}}_v)$

$$\hat{\dot{\gamma}} = \hat{\dot{\gamma}}_e + \hat{\dot{\gamma}}_v \tag{4.25}$$

The elastic part can be nondimensionalized the same way as

$$\hat{\dot{\gamma}} = \frac{\dot{\gamma}_e \, \mu_o(P,T)}{\tau_L(P,T)} = \frac{\dot{\tau}(P,T) \, \mu_o(P,T)}{G_\infty(P,T)\tau_L(P,T)} = \hat{\dot{\tau}} \tag{4.26}$$

where $G_\infty(P,T)$ is the limiting elastic shear modulus at a given temperature and pressure. With the above natural log relation for the viscous part, a modified Maxwell model is obtained:

$$\hat{\dot{\gamma}} = \hat{\dot{\tau}} - \ell n(1 - \hat{\tau})$$

or

$$\dot{\gamma} = \frac{1}{G_\infty} \frac{d\tau}{dt} - \frac{\tau_L}{\mu_o} \ell n(1 - \frac{\tau}{\tau_L}) \tag{4.27}$$

In order to use this equation, three primary physical properties are required. These include the low shear stress viscosity μ_o, the limiting yield shear stress τ_L, and the limiting elastic shear modulus G_∞. These three parameters are all functions of the temperature and pressure.

In the application of the spiral bevel gears in heavy loaded cases, the pressure in most contact ellipses is very high (1 G Pa to 2 G Pa or 150,000 psi to 300,000 psi) and the slide to roll ratio is about 0.05 - 0.3. Under these severe conditions, the limiting shear stress for most lubricants should occur in most of the contact area. For the temperature calculation, it is safe to assume that the uniform limiting shear stress is applied at a given average pressure and temperature in the contact ellipse.

$$\tau = \tau_L(P_{ave}, T_{ave}) \tag{4.28}$$

where τ_L is given by experimental data.

Since experimental data for τ_L in the temperatures encountered in spiral gears are not available, the conventional way to calculate this yield shear stress postulated by Dyson is used:

$$\tau_L = \bar{G}_\infty/4 \tag{4.29}$$

where $\bar{G}_\infty$ is called limiting shear modulus, and $\bar{G}_\infty$ is a function of temperature and pressure. Based on the experimental work of Hutton (11) and Switch (27), Dyson proposed a relationship between $\bar{G}_\infty$, temperature and pressure for high viscosity index mineral oils:

$$G_{\infty}(P,T) = \frac{1.2P}{2.52 + 0.0133\ (T - 492)} - 1.45 \times 10^{4} \qquad (4.30)$$

where P is in psi, and T is in ^{o}R.

A subroutine was prepared to evaluate the traction based on Bair and Winer's model. Unfortunately, for the temperatures encountered in spiral bevel gears, the values of μ_0, τ_L and G_{∞} are not available from Bair and Winer's work.

4.5 Film Thickness

In 1916, Martin provided the first paper about roller lubrication. Although he failed to predict a correct film thickness by using the assumptions of a rigid body and an incompressible isoviscous fluid, his approach was welcomed by later investigators. The influence on the film thickness by the pressure dependence of the viscosity in the contact area was examined by Gatcombe (45) by using an exponential relationship and by Hersey and Lowdenslager (46) by using parabolic viscosity-pressure relationships. More investigations in this field were made by Cameron (49) and by McEwen (48). These results showed that the effect of pressure dependence on viscosity could not alone account for the difference between prediced and observed film thickness, although it did provide some improvement. The effects of elastic deformation and pressure dependent viscosity were considered first by Ertel and Grubin in 1945, who initiated the study of EHD lubrication. By assuming the deformation in the inlet region of contact zone was the same as that of the dry Hertzian contact, they calculated the pressure and film thickness in this region. Dowson and Higginson (19) developed a general formula for minimum film thickness for line contacts which included the effects of elastic distortion and pressure dependent viscosity. The dimensionless form of this equation is

$$H_{min,\ell} = 1.6\ G^{0.6}\ U^{0.7}\ W_D^{0.13} \tag{4.31}$$

where

$$G = \alpha E'$$

$$U = \eta_o u / E' R$$

$$W_D = W / E' R$$

R is the effective radius of the roller pair, E' is the effective elastic modulus, η_o is the atmosphere viscosity of the lubricant, α is the pressure dependent viscosity parameter, $\eta = \eta_o \exp(\alpha p)$, w is the load per unit length, and u is the speed. The thermal effect due to sliding was examined by Cheng and Sternlicht (50) by using numerical technique to solve the Reynold, elastic, energy and heat transfer equations. Their results indicated that the isothermal Dowson-Higginson equation could still predict a good approximation to the measured film thickness if η_o was taken as the value at the bulk surface temperature of the contact bodies.

The 'cylinder model' used in the lubrication analysis of gears is only good at the pitch point. Actually, the effective radius and rolling velocity are varied from point to point along the contact path. Wayne and Rodzimovsky (51) were among the first investigators who examined the actual contact ratio, actual involute profile, the combined effects of rolling and sliding, and film thickness in the whole course of the contact path. Unfortunately, their analysis did not include the elastic deformation in the contact zone. Based on the quasi-steady state assumption, Gu (52) used the EHD lubrication theory to calculate the film thickness of the spur gears by including the time dependent term $\partial(ph)/\partial t$ in the Reynolds equation. He found that this term did not have much effect on the minimum film thickness.

In spur gears, the contact between mating teeth is a line contact extended from one end of the tooth to the other end of the tooth. Provided that the bulk surface temperature of the gear teeth is known beforehand, one cannot predict accurately the minimum film thickness by

using the Dowson-Higginson equation. For conjugate spiral bevel gears, the contact is still a full line from one limit to the other limit. However, fully conjugated spiral bevel gears seldom exist in practice. The actual spiral bevel gears are crowned in both directions (lengthwise and profile-wise) to reduce sensitivity to the shift of contact patterns due to misalignment. In such cases, an elliptical contact area appears between the mating teeth under load, for which line contact solution is no longer valid.

Hamrock and Dowson (53) evaluated numerically the analysis of an isothermal EHD lubrication point contact. They showed that the minimum film thickness could be related to the well-known line contact solution by simple expression involving the ellipticity parameter (54). In this study, Hamrock-Dowson's point contact solution will be adapted in the elliptical contact of spiral bevel gears.

The effective situation of contact between the spiral bevel gear and pinion can be seen in Fig. 4-5, in which there is a flat plane contact with a body which is described by the difference between neighboring surfaces of the gear and the pinion at the contact point. This curved body has effective radii R_x and R_y along the principal axis x and y, respectively. Under a load P, the surface near the flat plane will deform to an elliptical shape with semi-major axis AMAX and semi-minor axis BMAX. V_p and V_g are the velocities of the pinion and gear at the contact point. The ellipticity parameter was defined as the ratio of AMAX to BMAX. The minimum film thickness in the contact zone was related to Dowson-Higginson's line contact solution by the equation

$$H_{min} = H_{min,\ell}(1.0 - 1.6\ e^{-0.62k}) \tag{4.32}$$

where $H_{min,\ell}$: Dimensionless film thickness of Dowson-Higginson solution

K : Ellipticity parameter

and $H_{min,\ell} = \frac{h_{min,\ell}}{R_x}$

$$U_{px} = V_p \cos \theta_p$$

$$U_{py} = V_p \sin \theta_p$$

$$U_{gx} = V_g \cos \theta_g$$

$$U_{gy} = V_g \sin \theta_g$$

$$U_x = (U_{px} + U_{gx})/2.0$$

$$U_y = (U_{py} + U_{gy})/2.0$$

$$V = \sqrt{Ux^2 + Uy^2}$$

The dimensional form $h_{min,\ell}$ of the minimum film thickness for a line contact can be written as

$$h_{min,\ell} = 1.6\ \alpha^{0.6}(\eta_o V)^{0.7}\ E'^{0.43}/w^{0.13} \tag{4.33}$$

where w = P/2AMAX is the load per unit length and P is total load. The viscosity η_o is taken at the bulk surface temperature to account for the thermal effects on the film thickness.

It is important to note that η_o, P, AMAX, BMAX and V are varied along the path of contact. V depends on the gear kinematics, and AMAX and BMAX depend on the gear geometry and dynamic load P. η_o is strongly dependent upon the local static surface temperature which, in turn, is influenced by the local film thickness through frictional heating. Thus, the film thickness and the static (bulk) surface temperature are interdependent, and must be solved as a coupled system. The dynamic load is assumed to be uninfluenced by the film thickness.

4.6 Results of Lubrication Performance

The same set of gears used for the dynamic load calculations are used here to demonstrate calculation of the lubrication performance. Results were obtained for a range of operating conditions to determine the effect of speed, load, lubricant viscosity, and ambient temperature on the film thickness, bulk temperature, and flash temperature.

The sliding velocity decreases from the beginning of the contact path where the gear tip contacts the pinion root, until the contact point is near the pitch point where the sliding velocity becomes zero. Then the sliding velocity increases all the way to the end of the contact path where the pinion tip contacts the gear root. The current set of gears has the feature that the sliding velocity at the end of the contact path is larger than that at the beginning of the contact path; this fact creates a situation where more heat is generated at the end of the contact path.

Typical distributions of the bulk temperature along the contact path are shown in Figs. 4-6 through Fig. 4-9 for various speeds. The bulk temperature of the pinion is always larger than that of the gear because the pinion speed is three times faster than the gear speed, and receives more heat in a unit time than the gear does. Although the temperature coefficients are higher near the gear tip, the maximum bulk temperature of both gears occurs at the end of the single tooth contact point where the maximum heat is generated. Distributions of the total flash temperature for the same cases are plotted on Fig. 4-10 through Fig. 4-13. The minimum flash temperature occurs at the pitch point where the sliding velocity is zero. For the high speed case, the variation

of dynamic load is less pronounced along the contact path. The rise of flash temperature on both sides of the pitch corresponds directly to the variation of sliding speed at the contact. The slight decrease at the end of the contact path is attributable to the decrease in dynamic load in this region.

Fig. 4-14 shows the distributions of the film thickness for four different gear speeds. No excessive variations are seen along the contact path. A moderate peak is evident at the pitch point for the high speed cases, and this is associated with the slight drop of bulk temperature at the pitch point. The steady rise of film thickness along the contact path is due to the increase in the entrainment velocity. The final uptrend of film thickness near the end of contact is again due to the decrease in the bulk temperature.

Finally, the effects of an increase in ambient viscosity, ambient temperature, and load on the minimum film thickness h_{min}, maximum bulk and total flash temperatures is demonstrated in Fig. 4-15. As expected, an increase in viscosity would improve lubrication performance with a much greater film thickness and a slight drop in both bulk and flash temperature. An increase in ambient temperature would reduce the film thickness considerably, and an increase in load would also reduce the film thickness due to the increase in the bulk temperature.

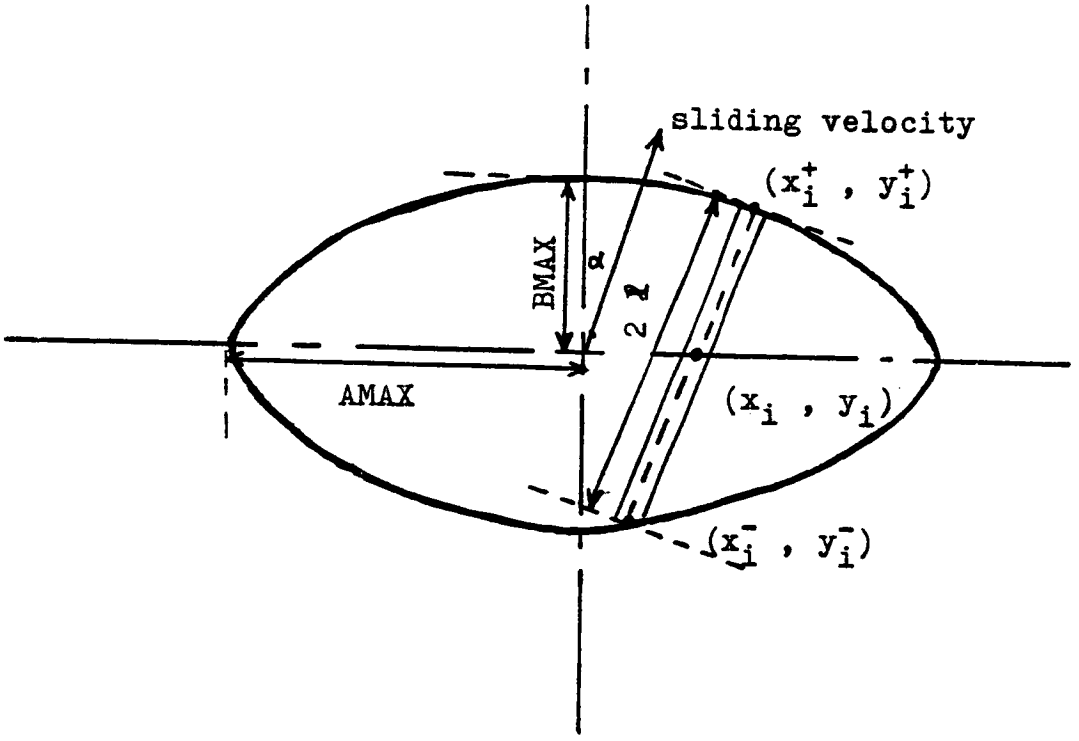

Fig. 4-1 contact shape and a differential stripe

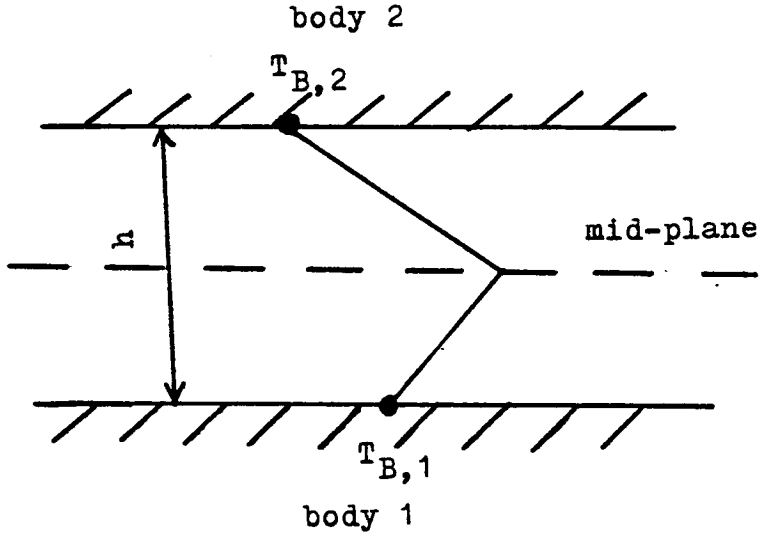

Fig. 4-2 temperature distribution across film thickness (h) with two different bulk temperatures

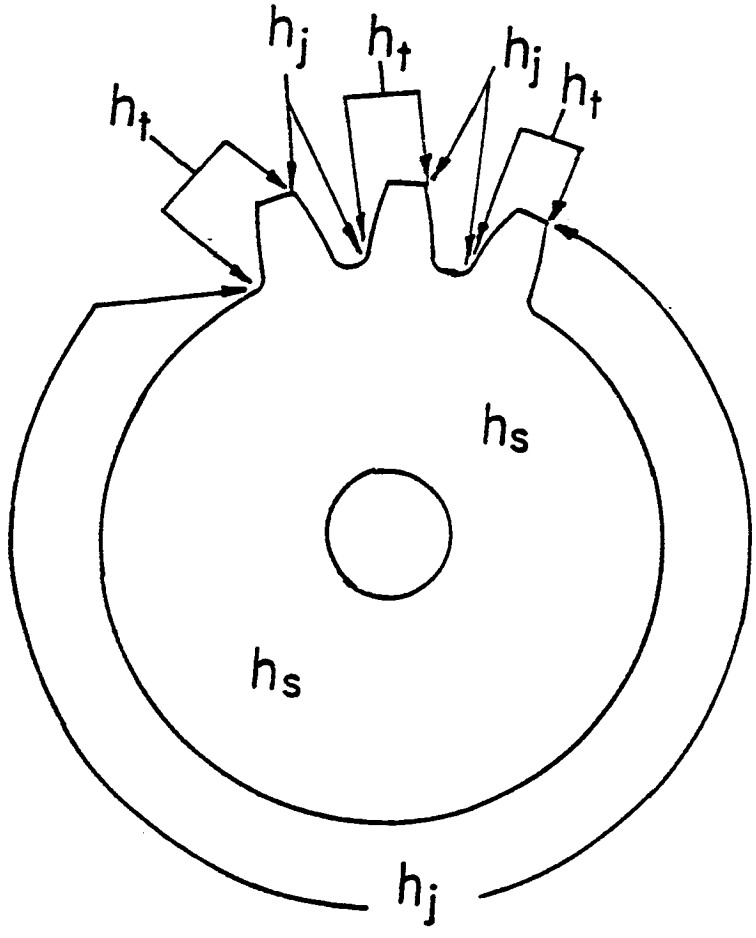

Fig. 4-3. Convective Surface on The Gear Model.

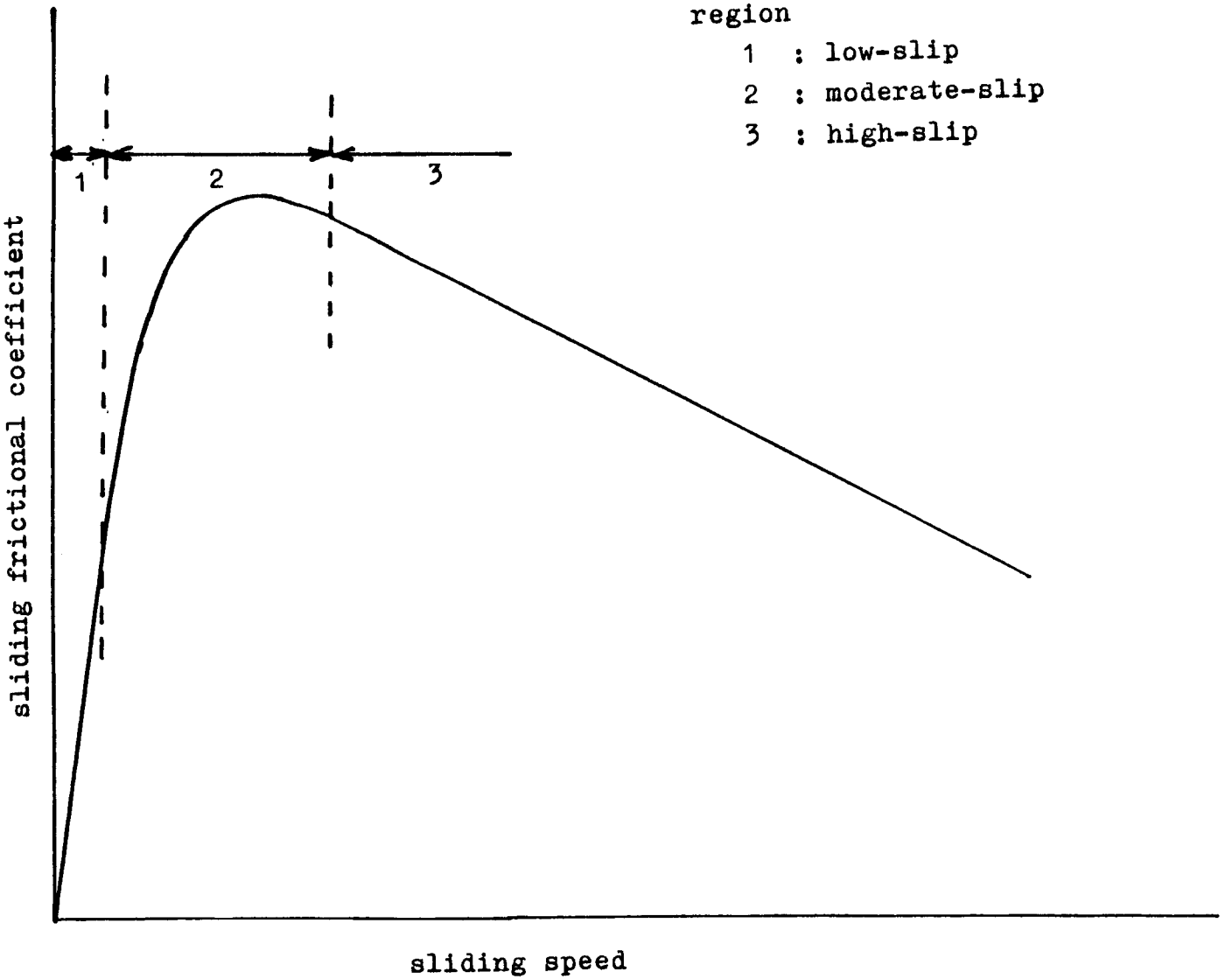

Fig. 4-4 traction coefficient curve

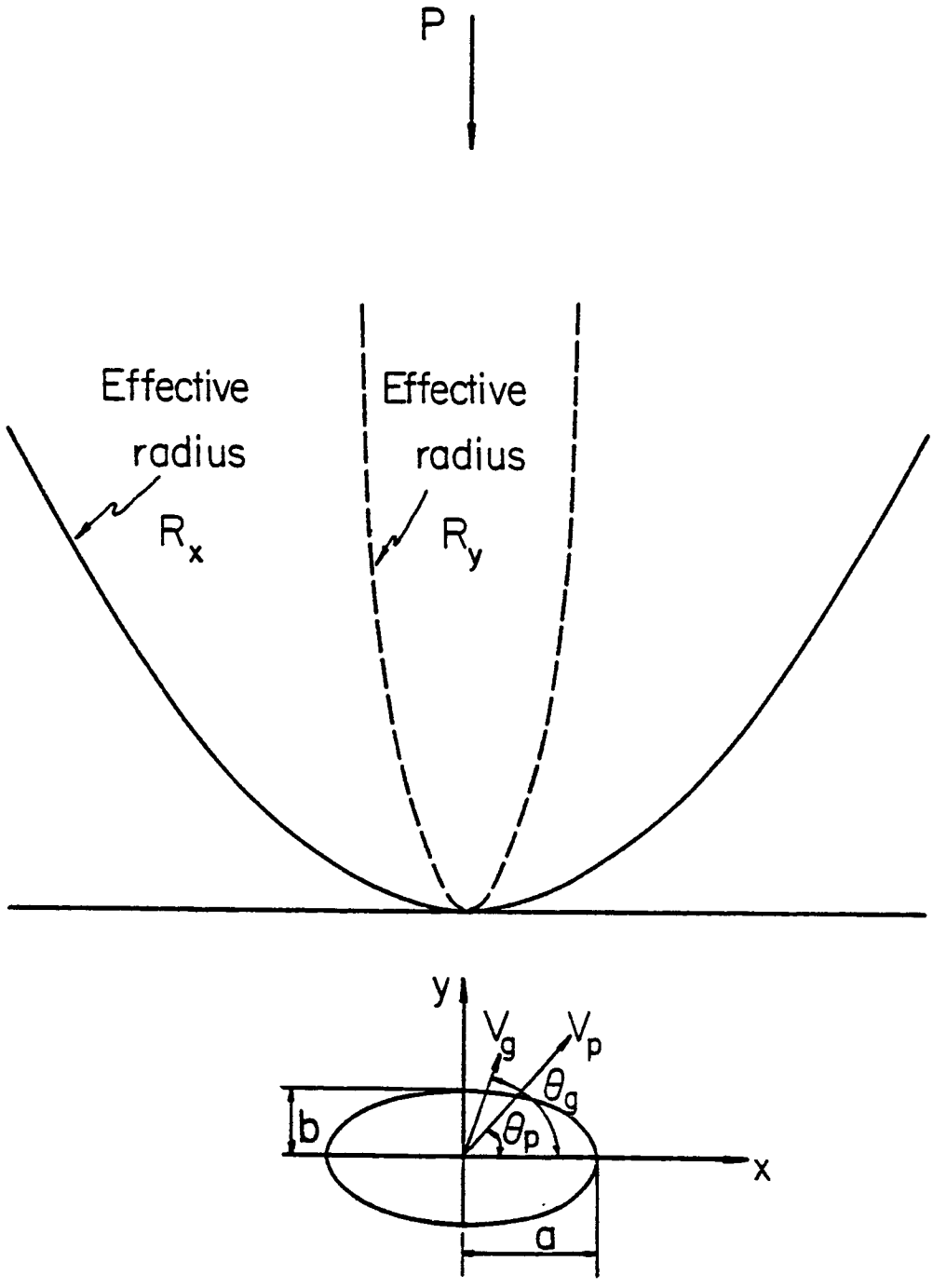

Fig. 4-5. Simulated Contact Situation And Contact Area With Velocity of Pinion And Gear

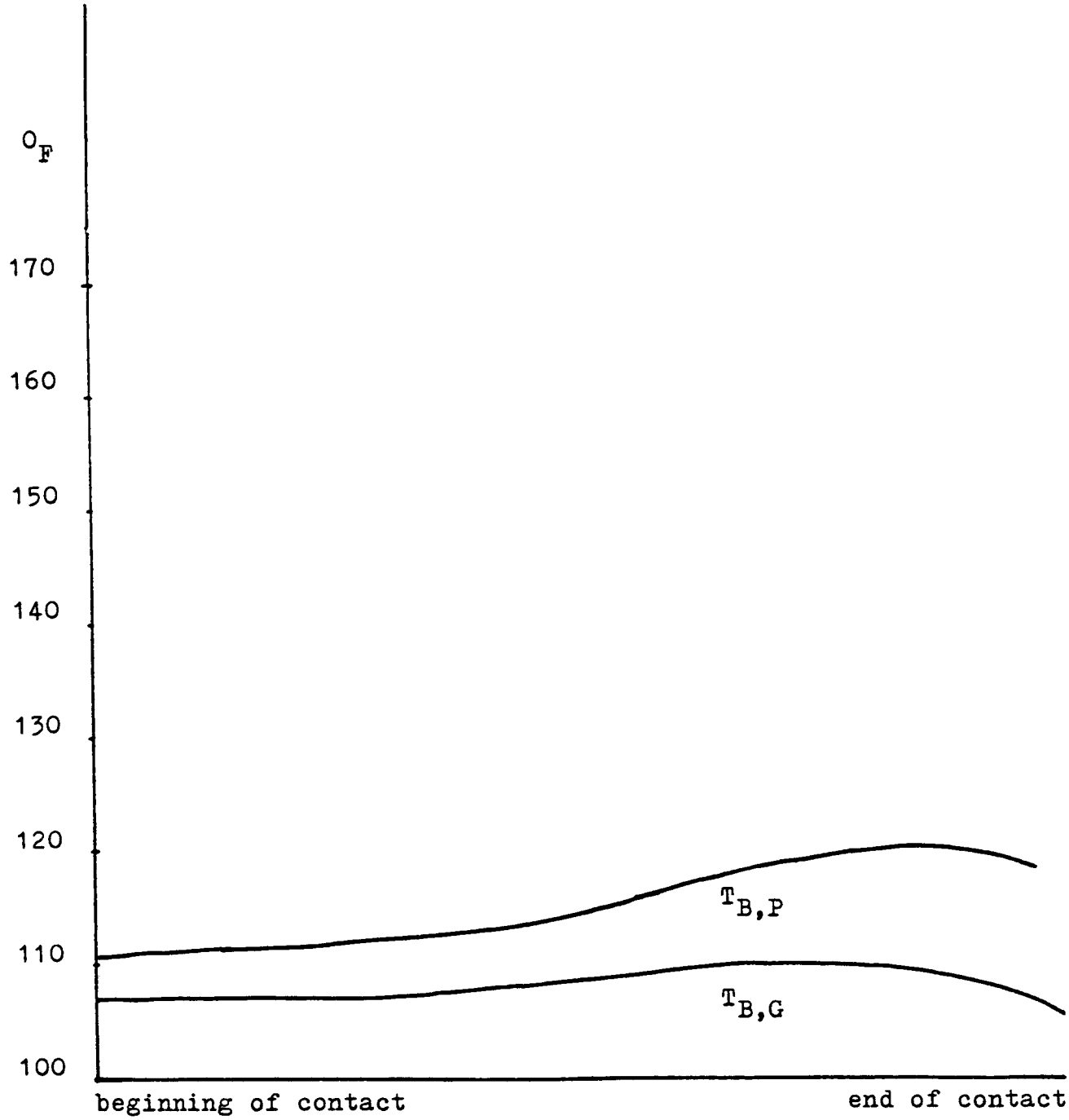

Fig. 4-6 bulk temperature distribution for gear speed 50 rad/sec

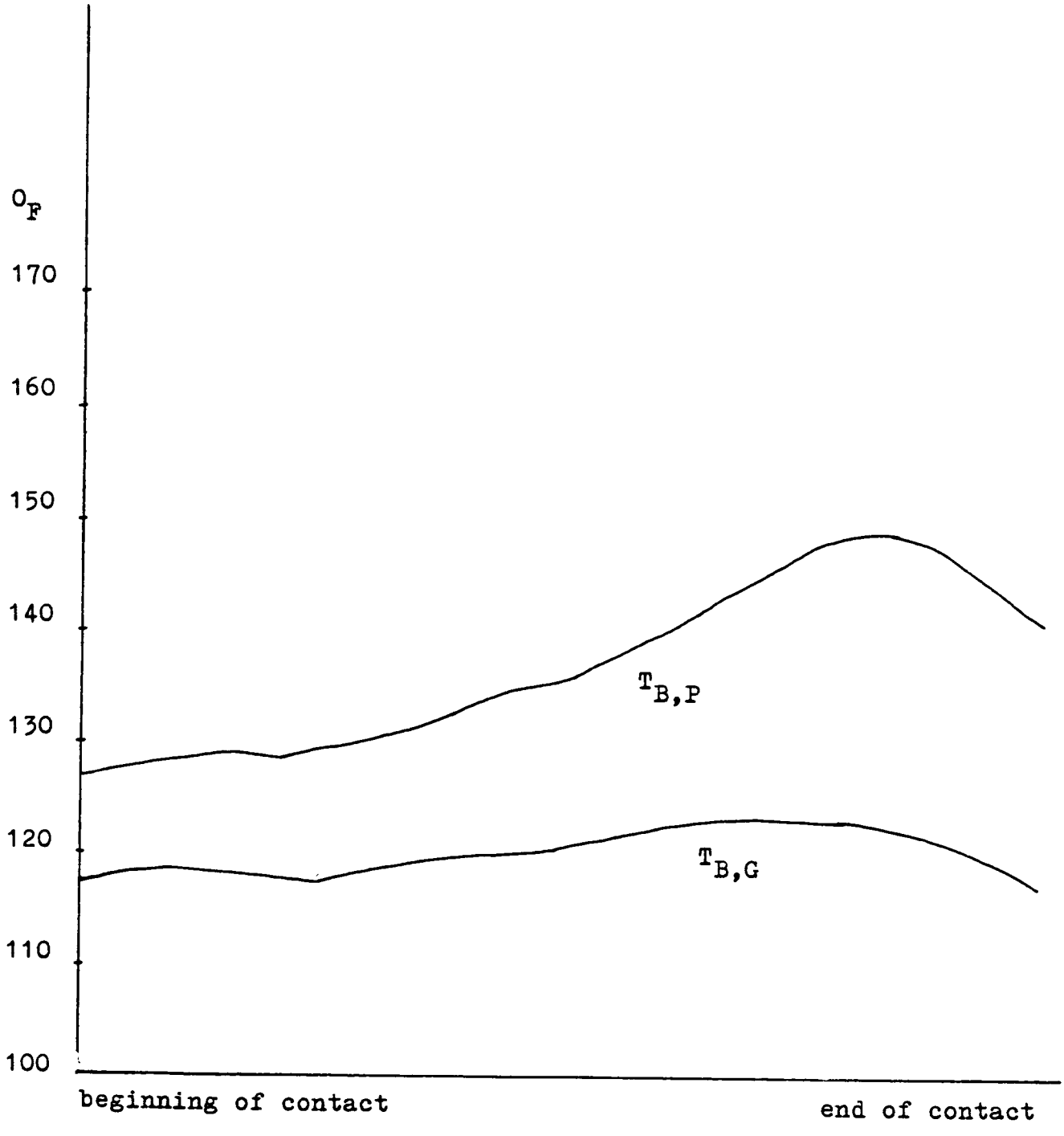

Fig. 4-7 bulk temperature distribution for gear speed 150 rad/sec

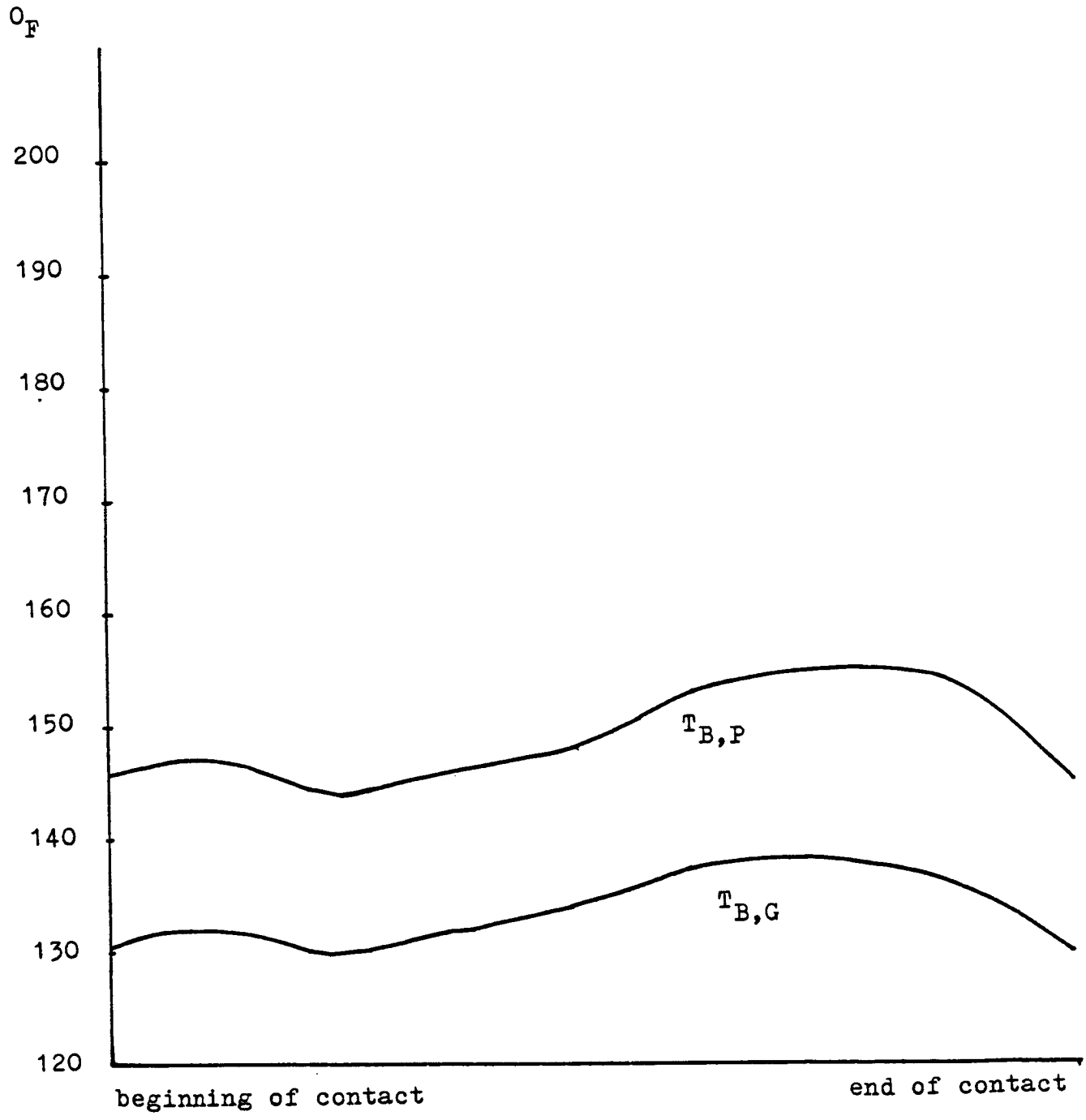

Fig. 4-8 bulk temperature distribution for gear speed 300 rad/sec

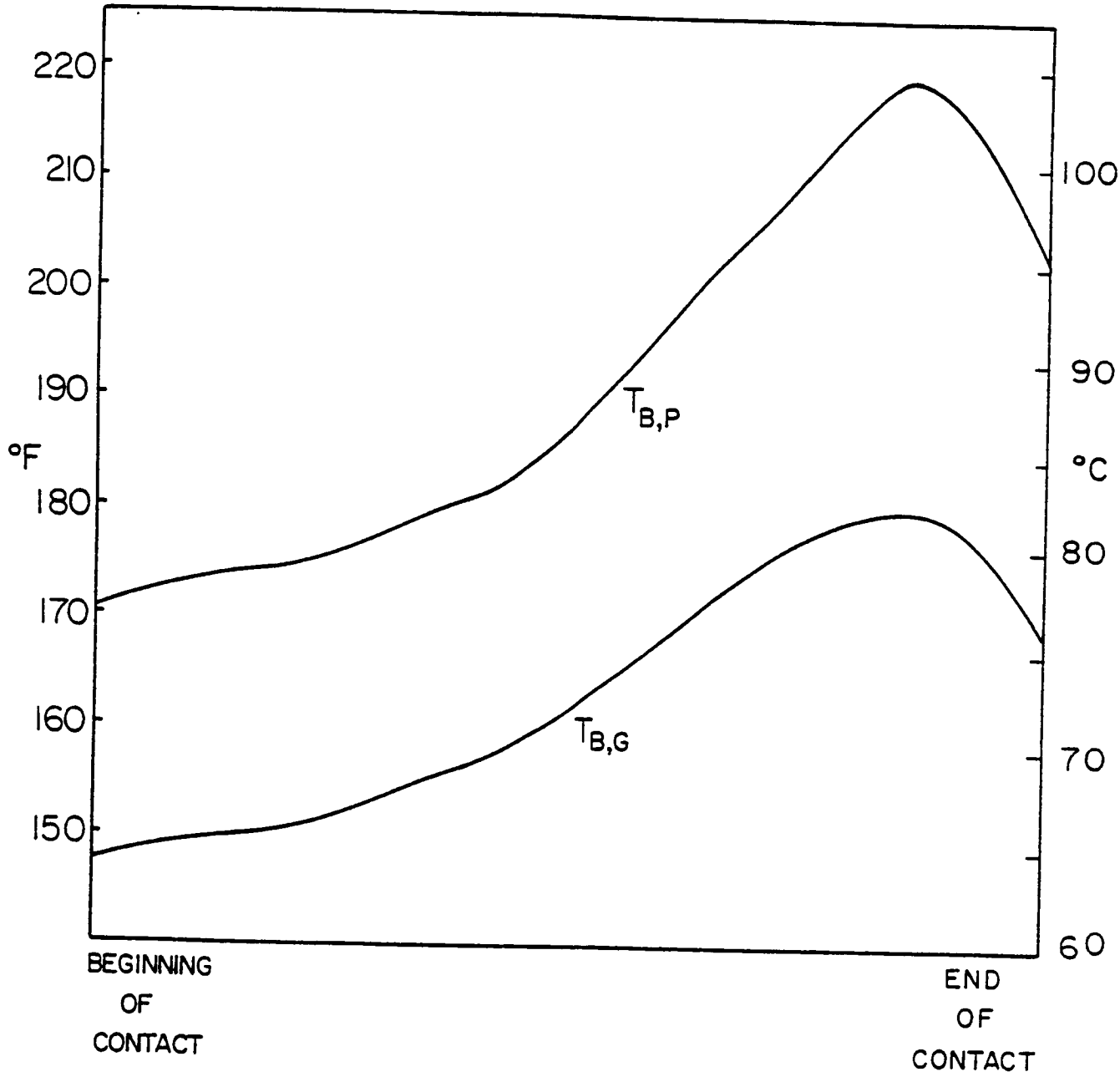

Fig. 4-9. Bulk Temperature Distribution For Gear Speed 523 rad/sec

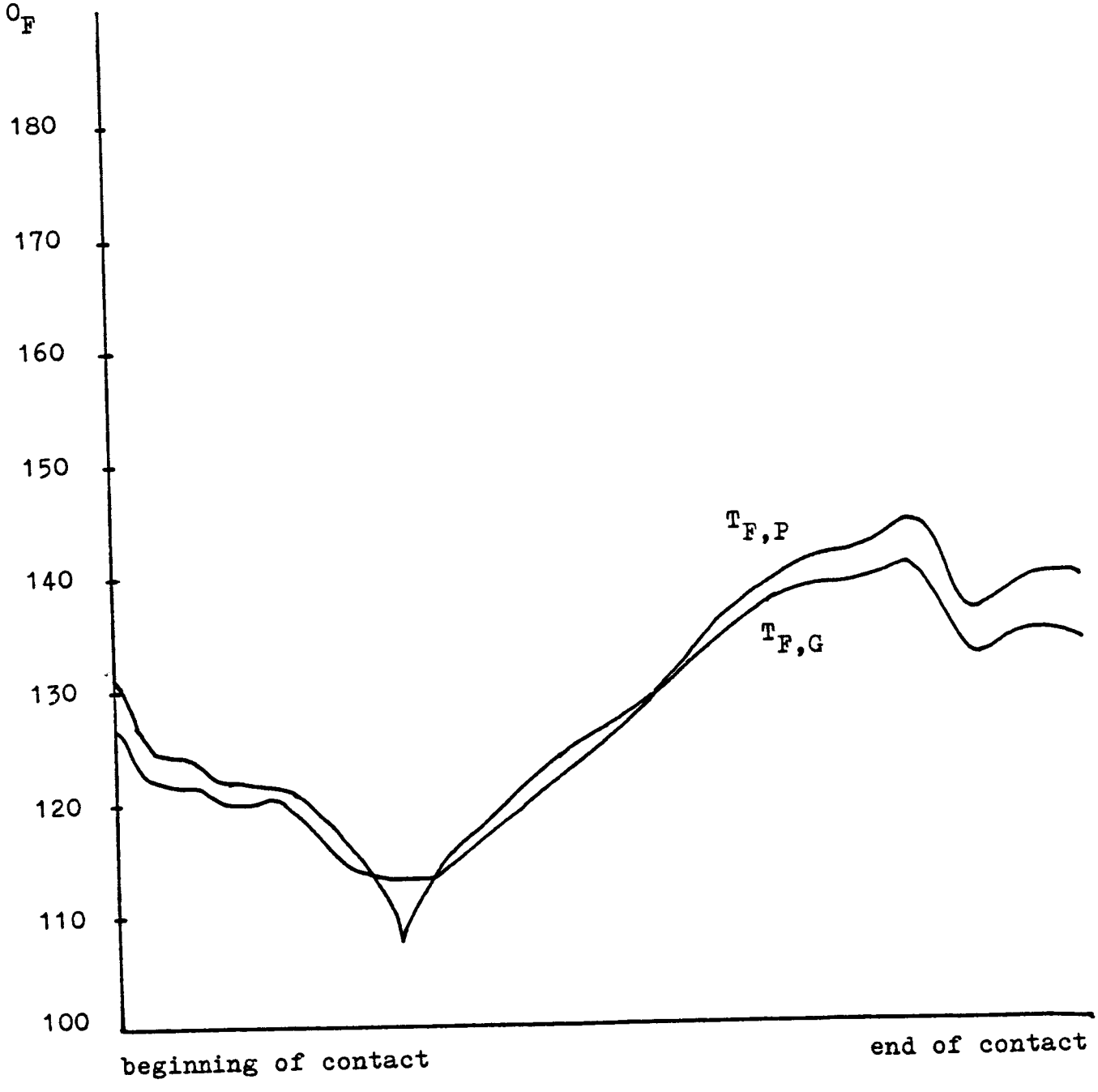

Fig. 4-10 flash temperature distribution for gear speed 50 rad/sec

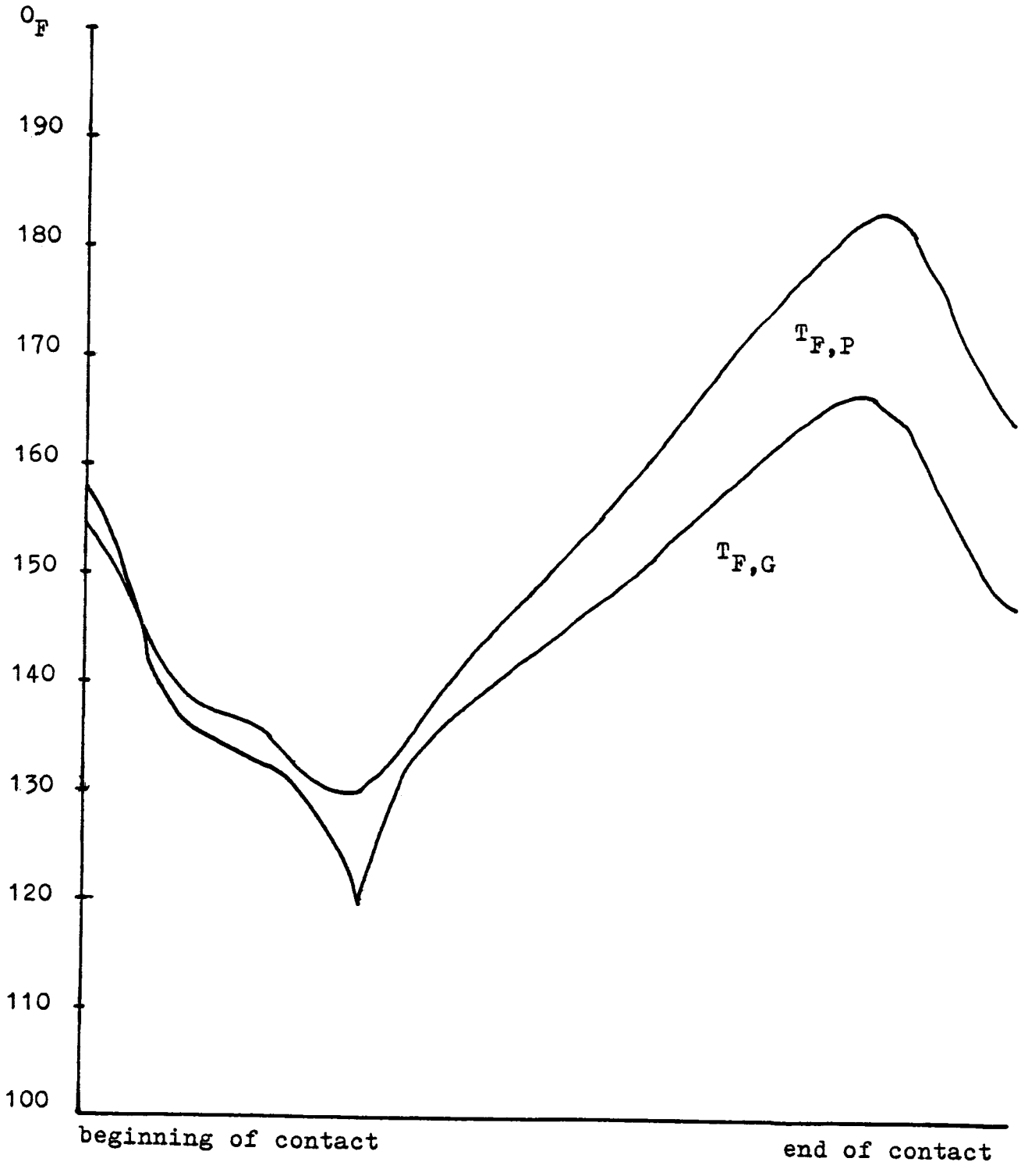

Fig. 4-11 flash temperature distribution for gear speed 150 rad/sec

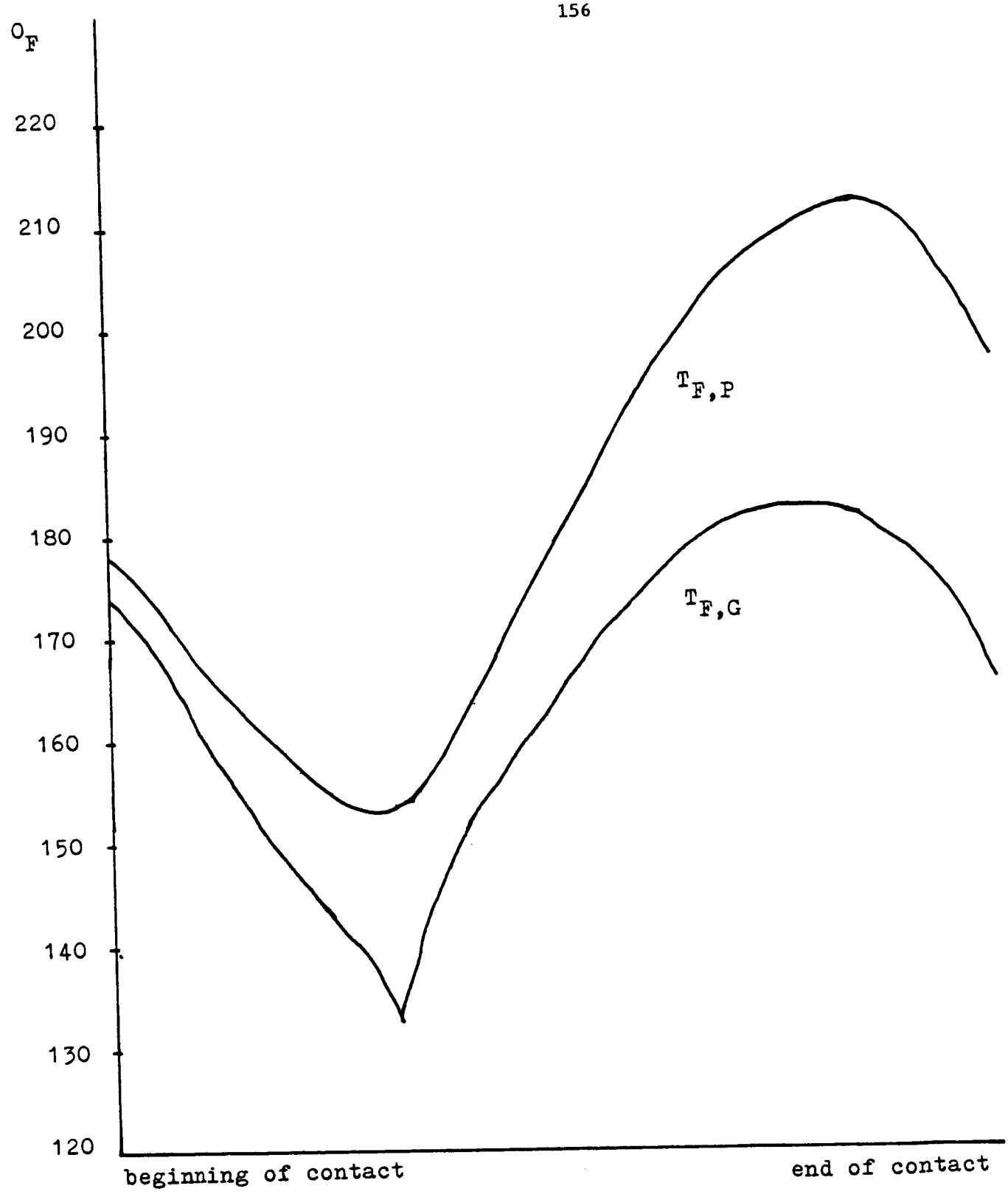

Fig. 4-12 flash temperature distribution for gear speed 300 rad/sec

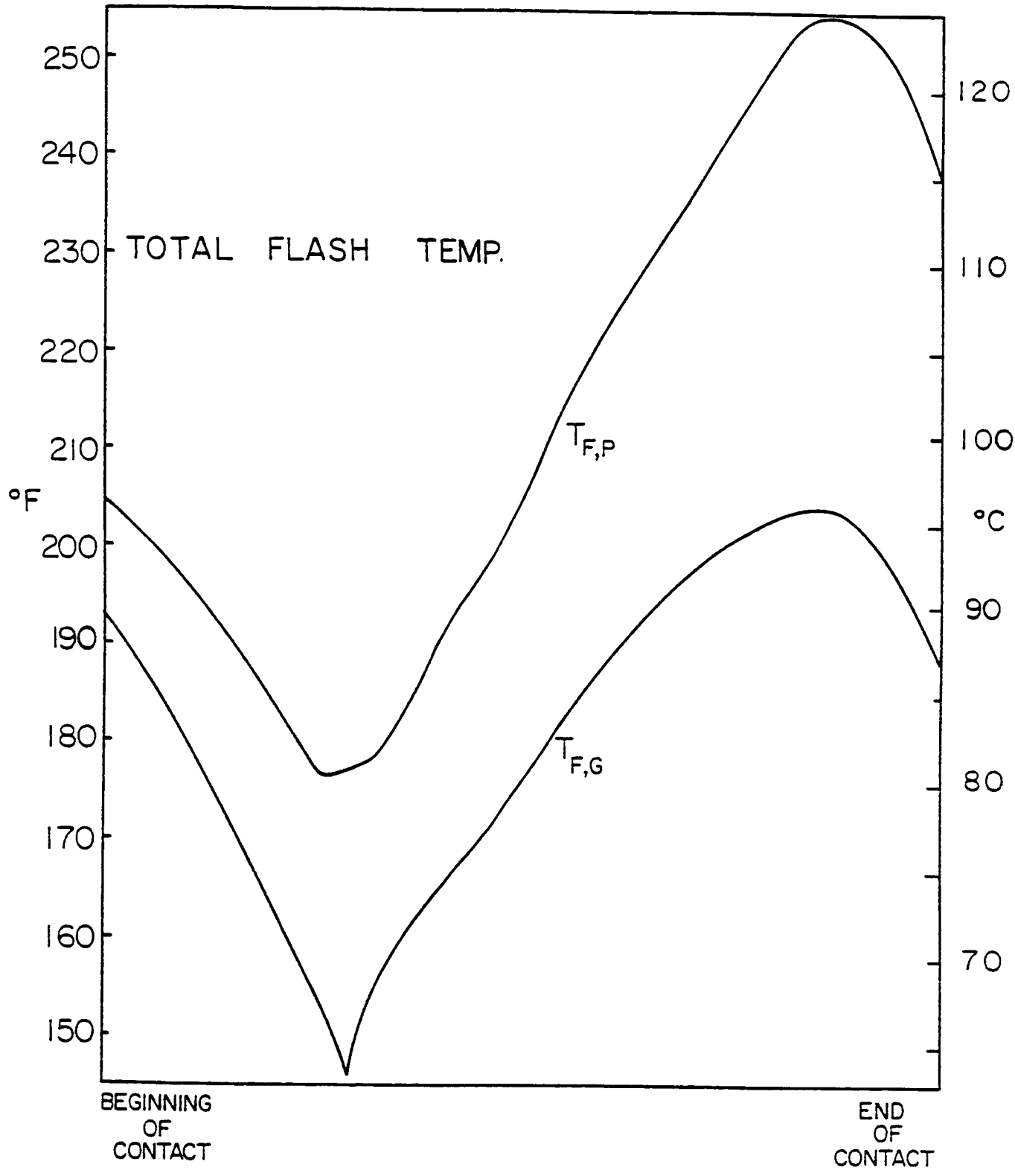

Fig. 4-13. Flash Temperature Distribution For Gear Speed 523 rad/sec.

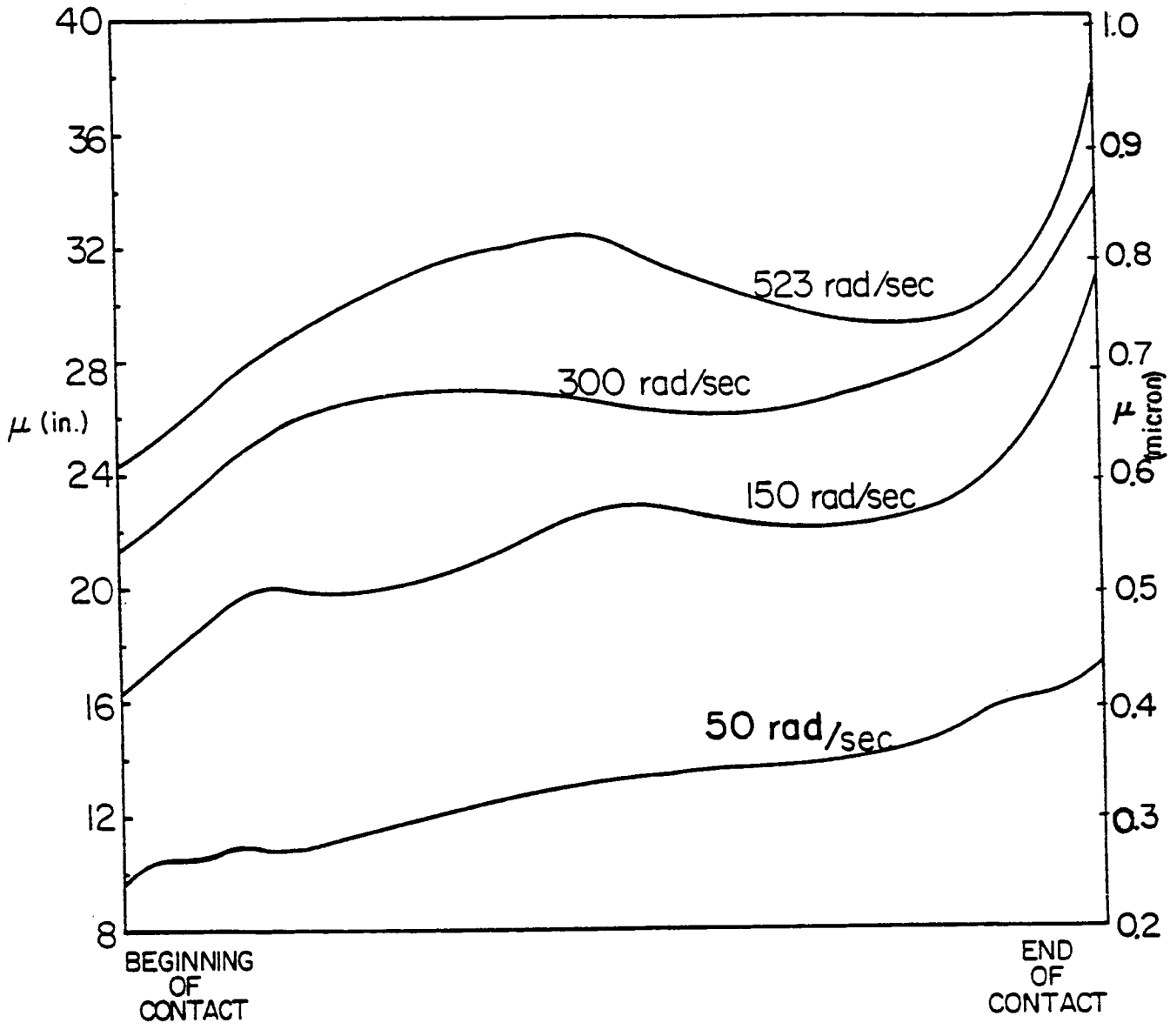

Fig. 4-14. Minimum Film Thickness is Plotted With Different Gear Speed.

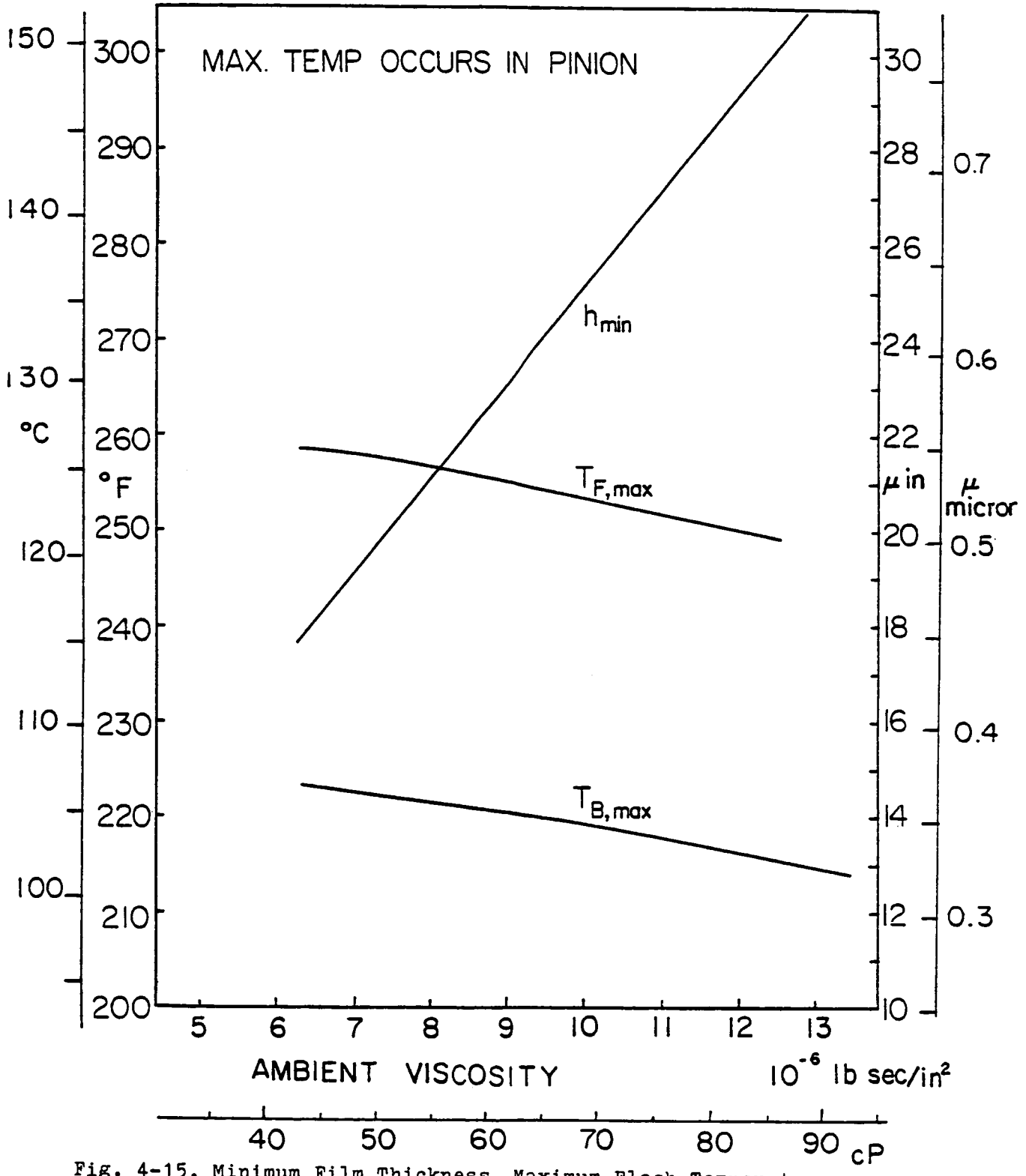

Fig. 4-15. Minimum Film Thickness, Maximum Flash Temperature And Maximum Bulk Temperature For Different Ambient Viscosity

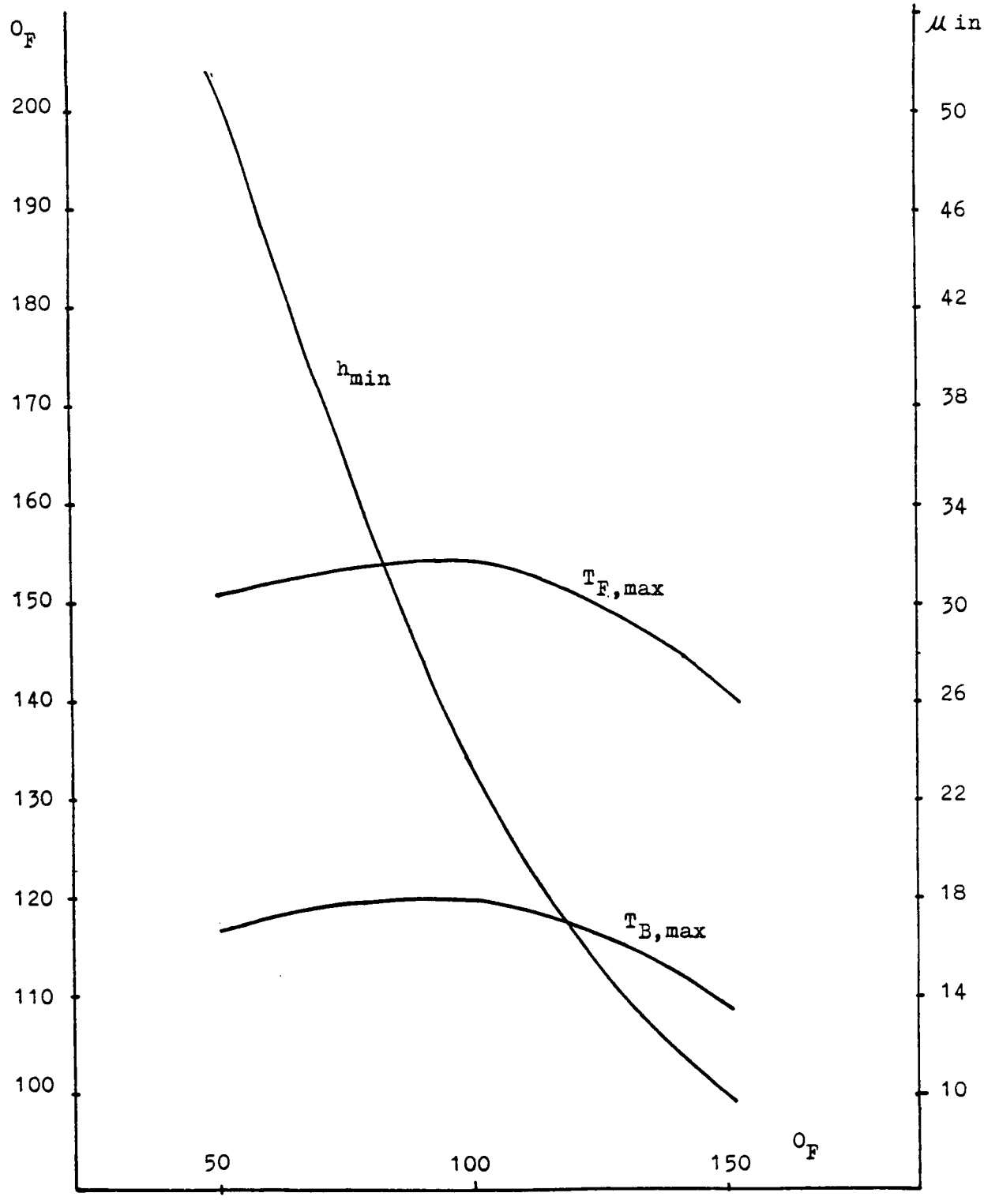

Fig. 4-16 minimum film thickness, maximum flash temperature and maximun bulk temperautre for different ambient temperatures

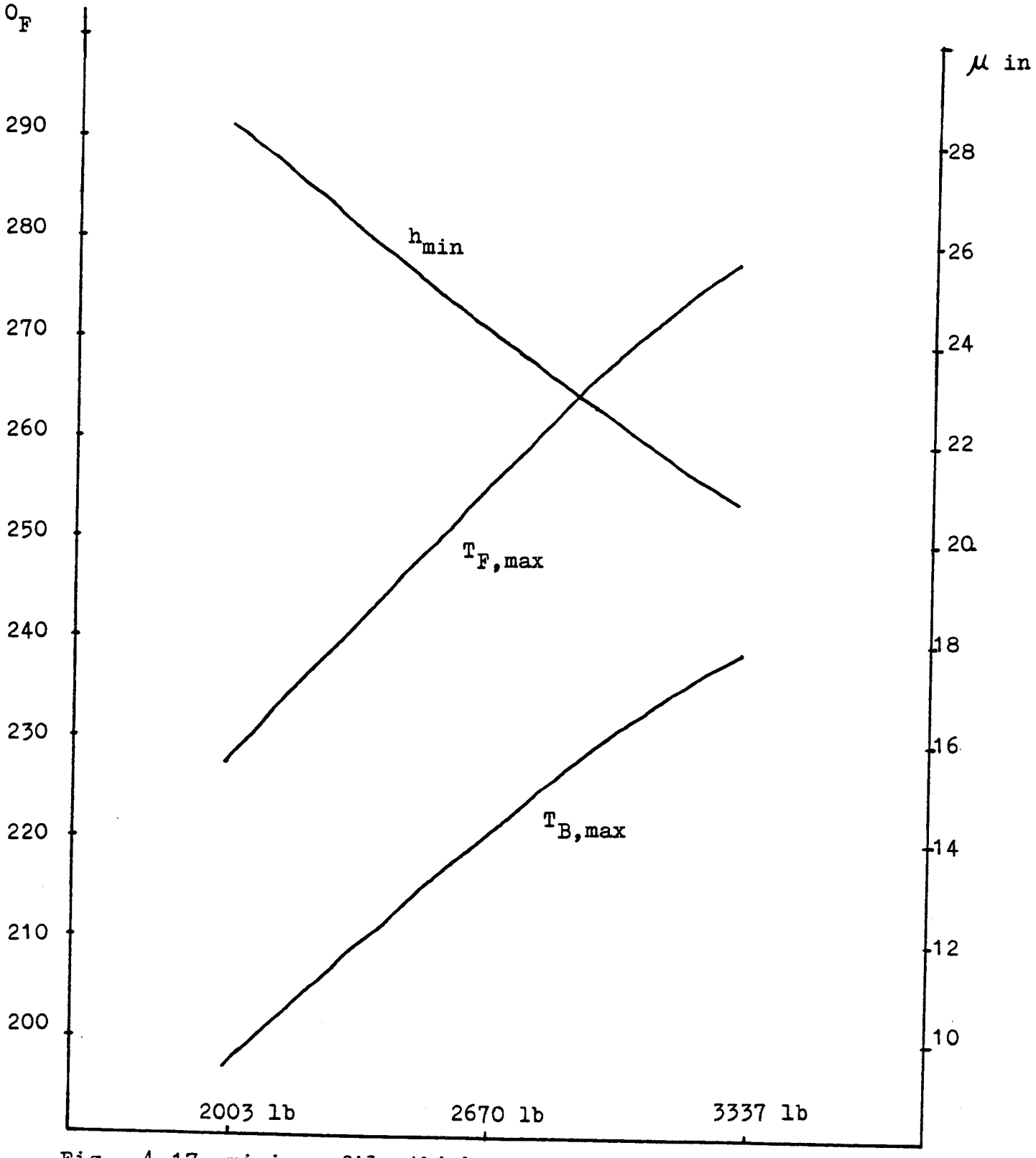

Fig. 4-17 minimum film thickness, maximum flash temperature and maximum bulk temperature for different loads

CHAPTER V

CONCLUDING REMARKS

A computer solution for the dynamic load in a pair of spiral bevel gear sets was developed by solving the equations of motion for the pinion and gear shaft. An existing finite element code was used to calculate the combined stiffness of the contacting pinion and gear teeth as a function of contact position in the zone of action. In addition to the dynamic load analysis, a computer solution was developed to predict the bulk surface temperature, the flash temperature, and the film thickness along the contact path. An existing finite element heat code was used to calculate the temperature influence coefficients from which the bulk surface temperature is calculated. Both the lubricant film thickness and the sliding traction are calculated from the recent findings in EHL theories.

Results were obtained for a set of experimental spiral bevel gears currently being tested at NASA Lewis Research Center. The results of dynamic load show that there exist numerous peaks in the variation of dynamic load against the gear shaft speed. These fluctuations correspond reasonably well with the critical frequencies of the system. The envelope of the peaks suggests that the highest dynamic load occurs somewhere near the critical frequency corresponding to the rotational mode oscillations of the two gears.

Results of the film thickness show that it's variation along the

contact path is not large, and is caused mainly by the increase in the entrainment velocity and the change in the bulk surface temperature. The total flash temperature variation is controlled by the sliding velocity, having its maximum near the end of the contact path where the transition from double to single teeth pair mesh occurs. Effects of operating variables on the minimum film thickness and maximum surface temperatures along the contact path can be obtained readily with this program. Results for the effect of change in the ambient viscosity show trends consistent with those anticipated from existing EHL theories.

TABLE II

GEAR DATA AND LUBRICANT DATA

	Gear	Pinion
Gear Data:		
Teeth	36	12
Pitch Angle	71°34'	18°26'
Shaft Angle	90°	
Spiral Angle	35°	
Diametral Pitch	5.14	
Standard Operating Conditions:		
Gear RPM	5000	
Pinion RPM	15000	
Load at Pitch Point N (lb)	11800 (2660)	
Ambient Temperature °C (°F)	37.8 (100)	
Geometric Dimensions: (see Fig. C-1)		
DGG = 0.1658 m (6.527 in)		
ROG = 0.0312 m (1.230 in)		
RIG = 0.04336 m (1.707 in)		
RZG = 0.1964 m (7.733 in)		
DGP = 0.2515 m (9.901 in)		
ROP = 0.0325 m (1.280 in)		
RIP = 0.09311 m (3.6656 in)		
RZP = 0.1987 m (7.824 in)		
Gear Material Data:		
Steel:		
Density g/cm^3 (lb/in^3)	7.81 (.282)	
Thermal Conductivity at 311°K (100°F)		
w/m°K (BTU/(sec)(in)(°F)):	46.7 (.000625)	
Young's Modulus GP_a (psi)	207. (30000000)	
Poisson Ratio	0.3	
Surface Convectivity		
w/m^2 °K (BTU/(sec)(in^2)(°F)):		
Oil Jet	397. (0.000135)	
Oil/Air Mist	19.8 (0.00000675)	
Air	3.97(0.00000135)	
Lubricant Data:		
Super-Refined, Napththenic, Mineral-Oil		
Dynamic Viscosity at 311°K (100°F)		
cp ($lb \cdot sec/in^2$)	64.7 (0.00000938)	
Density at 311°K (100°F) g/cm^3 (lb/in^3)	0.61(0.022)	
Thermal Conductivity at 311°K (100°F)		
w/m°K (BTU/(sec)(in)(°F))	0.125(0.00000168)	
Viscosity-Pressure • Temperature Relation		
$\mu = \mu_o \exp(\alpha p + \beta(\frac{1}{T} - \frac{1}{T_o}))$		
Pressure-Viscosity Coefficient		
α m^2/MN (in^2/lb)	0.023(0.00016)	
Temperature-Viscosity Coefficient		
β °K (°R)	3890 (7000)	

REFERENCES

(For Chapter II)

(1) Wang, K. L. and Cheng, H. S., "A Numerical Solution to the Dynamic Load, Film Thickness, and Surface Temperatures in Spur Gears, Part I and II." To appear in Journal of Mechanical Design Trans. of ASME.

(2) Wallace, D. B. and Seireg, A., "Computer Simulation of Dynamic Stress, Deformation, and Fracture of Gear Teeth," Journal of Engineering for Industry, Trans. ASME, Series B, Vol. 95, No. 4, Nov. 1973, P1108-1114.

(3) Wilcox, L. and Coleman, W., "Application of Finite Elements to the Analysis of Gear Tooth Stresses," Journal of Engineering for Industry, Trans. ASME, Series B, Vol. 95, No. 4, Nov. 1973, P1139-1148.

(4) Chabert, G., Dang Tran, T. and Mathis, R., "An Evaluation of Stress and Deflection of Spur Gear Teeth Under Strain," Journal of Engineering for Industry, Trans. ASME, Series B, Vol. 96, No. 1, Feb. 1974, P85-93.

(5) Gu, A., "Elastohydrodynamic Lubrication of Involute Gear," Journal of Engineering for Industry, Trans. ASME, Series B, Vol. 95, No. 4, Nov. 1973, P1104-1170.

(6) Akin, L. S., "An Interdisciplinary Lubrication Theory for Gears (with Particular Emphasis on the Scuffing Mode of Failure)," Journal of Engineering for Industry, Trans. ASME, Series B, Vol. 95, No. 4, Nov. 1973, P1178-1195.

(7) Krenzer, T. J., "Effect of the Cutter Radius on Spiral Bevel and Hypoid Tooth Contact Behavior," American Gear Manufacturers Association, AGMA 129.21, Oct. 1976.

(8) Baxter, M. L., "Effect of Misalignment on Tooth Action of Bevel and Hypoid Gears," Report from Gleason Works, Sept. 1968.

(9) Baxter, M. L., "Exact Determination of Tooth Surfaces for Spiral Bevel and Hypoid Gears," American Gear Manufacturers Association, AGMA 139.02, Oct. 1966.

(10) Bonsignore, A. T., "The Effect of Cutter Diameter on Spiral Bevel Tooth Proportions," American Gear Manufacturers Association, AGMA 124.20, Oct. 1976.

(11) "Understanding Tooth Contact Analysis," Report from Gleason Works, 1970.

(12) Baxter, M. L., "Second-Order Surface Generation," The Journal of the Mathematics Society, Vol. 23, Part 2, 1973.

REFERENCES

(For Chapters III and IV)

(1) Buckingham, E., "Analytical Mechanics of Gears," Dover Publications, Inc., New York, 1963.

(2) Tuplin, W. A., "Dynamic Loads on Gear Teeth," Machine Design, Vol. 25, No. 10, 1953.

(3) Reswick, J. B., "Dynamic Loads on Spur and Helical Gear Teeth," Trans. ASME, Vol. 77, 1955.

(4) Tuplin, W. A., "Dynamic Loads on Gear Teeth," Proceedings, International Conference on Gearing, Institution of Mechanical Engineers, London, 1958.

(5) Attia, A. Y., "Dynamic Loading of Spur Gear Teeth," Journal of Eng. for Ind., Trans. ASME, Series B, Vol. 81, 1959.

(6) Houser, D. R. and Seireg, A., "Evaluation of Dynamic Factors for Spur and Helical Gears," Journal of Eng. for Industry, Trans. ASME, May 1970.

(7) Ichimayu, K. and Hirano, I., "Dynamic Behavior of Heavy-Loaded Spur Gears," ASME Paper No. 72-PTG-14, 1972.

(8) Ishikawa, J., Hayashi, K. and Yokoyana, M., "Surface Temperature and Scoring Resistance of Heavy-Duty Gears," ASME Paper No. 72-PTG-22, 1972.

(9) Wang, O. K., "Thermal Elastohydrodynamic Lubrication of Spur Gears," Ph.D. Thesis, Northwestern University.

(10) Terauchi, Y., Miyao, Y., Fujii, M. and Sagawa, K., "Dynamic Behavior of Straight Bevel Gears," Bulletin of the JSME, Vol. 23, No. 175, 1980.

(11) Hutton, J. F., "Viscoelastic Relation Spectra of Lubricating Oils and Their Component Fractions," Proc. of the Royal Soc. of London, Series A., Vol. 304, 1968.

(12) Wallace, D. W. and Seireg, A., "Computer Simulation of Dynamic Stress, Deformation, and Fracture of Gear Teeth," Journal of Eng. for Ind., Trans. ASME, Nov. 1973.

(13) Block, H., "General Discussion on Lubrication," Inst. Mech. Engrs., London, Vol. 2, 1937.

(14) Block, H., "Theoretical Study of Temperature Rise at Surfaces of Actual Contact Under Oiliness Lubricating Conditions," Proc. Inst. Mech. Engrs., Pt. 2, 1973.

(15) Jaeger, J. C., "Moving Sources of Heat and Temperature at Sliding Contact," Journal of Proc. Roy. Soc. N. S. W. 76, 1942.

(16) Archard, F. J., "The Temperature of Rubbing Surfaces," Wear 2, 1958-1959.

(17) Cameron, A., Gordon, A. N. and Symm, G. T., "Contact Temperatures in Rolling Sliding Surfaces," Proceedings of Royal Society, A286, 1965.

(18) Francis, H. A., "Interfacial Temperature Distribution within a Sliding Hertzian Contact," Trans. ASLE, Vol. 14, 1970.

(19) Timoshenko and Goodier, "Theory of Elasticity," 1970, McGraw-Hill, Inc.

(20) Trachman, E. D., "The Rheological Effects on Friction in Elasto-hydrodynamic Lubrication," Ph.D. Thesis, Northwestern University, 1971.

(21) Plint, M. A., "Traction in Elastohydrodynamic Contacts," Proc. of the Inst. of Mech. Eng'g., Vol. 182, Pt. 1, 1967.

(22) Patir, N., "Estimate of the Bulk Temperature in Spur Gears Based on Finite Element Temperature Analysis," Master's Thesis, Northwestern University, 1976.

(23) Townsend, D. P. and Akin, L. S., "Analytical and Experimental Spur Gear Tooth Temperature as Affected by Operating Variables, NASA Technical Memorandum 81419.

(24) DeWinter, A. and Blok, H., "Fling-Off Cooling of Gear Teeth," ASME Journal of Engineering for Industry, Vol. 96, No. 1, 1974.

(25) Van Heijningen, G. J. J. and Blok, H., "Continuous as Against Intermittent Fling-Off Cooling of Gear Teeth," ASME Journal of Lubrication Technology, Vol. 96, No. 4, 1974.

(26) Misharin, J. A., "Influence of the Friction Conditions on the Magnitude of the Friction Coefficient in the Case of Rolling with Sliding," Inst. Mech. Engrs. Proc. of the International Conference on Gearing, 1958.

(27) Smith, F. W., "The Effect of Temperature in Concentrated Contact Lubrication," Trans. ASLE, Vol. 5, 1962.

(28) Crook, A. W., "The Lubrication of Rollers, III," Philosophical Transactions of the Royal Society of London, Series A, Vol. 254, 1961.

(29) Crook, A. W., "The Lubrication of Rollers, IV," Philosophical Transactions of the Royal Society of London, Series A, Vol. 255, 1963.

(30) Cheng, H. S., "A Refined Solution to the Thermal Elastohydrodynamic Lubrication of Rolling and Sliding Cylinders," Trans. ASLE, Vol. 8, No. 4, 1965.

(31) Dyson, A., "Friction Traction and Lubrication Rheology in EHD Lubrication," Philosophical Transactions of the Royal Society of London, Series A, Vol. 266, 1970.

(32) Gruber, G. J. and Litovitz, T. A., "Shear and Structural Relaxation in Molten Zinc Chloride," Journal of Chemical Physics, Vol. 40, 1964.

(33) Bell, J. C., Karmel, J. W. and Allen, C. M., "Non-Newtonian Behavior Elastohydrodyanmic Lubrication," Proc. of Roy. Soc., London, Series A, Vol. 337, 1974.

(34) Hirst, W. and Moore, A. J., "The Rheological Behavior of the Lubrication in the Contact Zone of a Rolling Contact System,"

(35) Trachman, E. G. and Cheng, H. S., "Rehological Effects on Friction in Elastohydrodynamic Lubrication," NASA CR-2206, March 1973.

(36) Smith, F. W., "Rolling Contact Lubrication. The Application of Elastohydrodynamic Theory," Journal of Basic Engineering, Trans. ASME, Series D, Vol. 87, 1965.

(37) Johnson, K. L. and Cameron, R., "Shear Behavior of EHD Oil Film at High Rolling Contact Pressure," Proc. Inst. Mech. Engr., Vol. 182, Part 1, 1968.

(38) Plint, M. A., "Traction in EHD Contact," Proc. Inst. Mech. Engr., Vol. 182, Part 1, 1968.

(39) Johnson, K. L. and Roberts, A. D., "Observations of Viscoelastic Behavior of an EHD Lubricant Film," Proc. of Roy. Soc. of London, Vol. 337, Series A, 1974.

(40) Johnson, K. L. and Tevaarwerk, J. L., "Shear Behavior of EHD Oil Film," Proc. of Roy. Soc., London, Series A, Vol. 356, 1977.

(41) Bair, S. and Winer, W. O., "Shear Strength Measurements of Lubricant at High Pressure," Journal of Lubrication Technology, Trans. ASME, Vol. 101, 1979.

(42) Bair, S. and Winer, W. O., "Some Observations on the Relationship Between Lubricant Mechanical and Dielectric Transitions Under Pressure," Journal of Lubrication Technology, Trans. ASME, Vol. 102, 1980.

(43) Tevaarwerk, J. L. and Johnson, K. L., "The Influence of Fluid Rheology on the Performance of Traction Drives," Journal of Lubrication Technology, Trans. ASME, Vol. 101, 1979.

(44) Bau, S. and Winer, W. O., "A Rheological Model for EHD Contacts Based on Primary Laboratory Data," Journal of Lubrication Technology, Trans. ASME, Vol. 101, 1979.

(45) Gatcombe, E. K., "Lubrication Characteristics of Involute Spur Gears - A Theoretical Investigation," Trans. ASME, Vol. 67, 1945.

(46) Hersey, M. D. and Lowdenslager, D. B., "Film Thickness Between Gear Teeth," Trans. ASME, Vol. 72, 1950.

(47) Cameron, A., "Hydrodynamic Theory in Gear Lubrication," J. Inst. Petrol. 38, 1952.

(48) McEwen, E., "The Effect of Variation of Viscosity with Pressure on the Load Carrying Capacity of Oil Films Between Gear Teeth," J. Inst. Petrol. 38, 1952.

(49) Dowson, D. and Higginson, G. R., "Elasto-Hydrodynamic Lubrication," Pergamon Press Ltd., 1966.

(50) Cheng, H. S. and Sternlicht, B., "A Numerical Solution for the Pressure, Temperature and Film Thickness Between Two Infinitely Long, Lubricated Rolling and Sliding Cylinders, Under Heavy Loads," ASME Paper No. 64, 1964.

(51) Adkins, R. Wayne and Radzimavsky, E. I., "Lubrication Phenomena in Spur Gears: Capacity, Film Thickness Variation, and Efficiency," Trans. ASME, Journal of Basic Engineering, Sept. 1965.

(52) Gu, A., "Elastohydrodynamic Lubrication of Involute Gears," Trans. ASME, Journal of Engineering for Industry, Nov. 1973.

(53) Hamrock, B. J. and Dowson, D., "Isothermal Elastohydrodynamic Lubrication of Point Contact," Part I," Trans. ASME, Journal of Lubrication Technology, April 1976.

(54) Hamrock, B. J. and Dowson, D., "Isothermal Elastohydrodynamic Lubrication of Point Contact, Part II," Trans. ASME, Journal of Lubrication Technology, July 1976.

NOMENCLATURE

(For Chapter II)

A_o	outer cone distance
$\bar{A}$	vector from machine center to the point on the surface
a	addendum
$\bar{a}$	linear acceleration vector
$\bar{B}$	vector from wheel center to the point on the surface
b	dedendum
DC	distance from cradle center to cam rotation center
D_ω	nominal wheel diameter
$\bar{d}$, $\bar{e}$, $\bar{c}$	machine coordinate
E_d	side dresser offset
E_m	blank offset
E_r	running offset
F	face width
$\bar{g}$	unit vector along the gear axis
L	distance along tooth axis from crossing point
L_{di}	inside dresser arm length

L_{do}	outside dresser arm length
m_i	velocity ratio
N, n	number of teeth for gear and pinion
$\overline{n}$	unit normal vector to the cutter blade
n_i	index interval
$\overline{P}$	unit vector along the pinion axis
Q	cradle setting angle
R	radius from tooth axis
$\overline{R}$	vector from crossing point to the point on the surface
$\overline{\gamma}$	vector from the intersection of plane containing the cutter tips and wheel axis to the point on the surface
γ_d	side dresser radial
$\overline{S}$	vector from machine center to the intersection of plane containing the cutter tips and the wheel axis
(S)	surface expression in matrix form
T	cam setting
T_o	standard cam setting
$\overline{t}$	unit vector along the direction of dressing diamond movement
$\overline{u}$	velocity of contact point

$\overline{V}$	linear velocity vector
$\overline{v}$	velocity of the contact point across the surface
X, Y, X	Cartesian coordinate
X	machine center to back
X_b	sliding base
X_{di}	inside diamond setting
X_{do}	outside diamond setting
$X_{g\gamma}$	gear apex withdraw
$X_{p\gamma}$	pinion apex withdraw
Z_d	side dresser axial
α	cam guide angle
β	eccentric angle
Γ, γ	pitch angle for gear and pinion
Γ_o,γ_o	face angle for gear and pinion
Γ_γ, γ_γ	root angle for gear and pinion
ε	cam rotation
η_u	cam pitch radius

θ	wheel cutter rotation angle based on the line perpendicular to the $\overline{S}$.
θ_d	dresser rotation angle
λ	work rotation
ρ	radius
Σ	shaft angle
Σ_γ	running shaft angle
$\Sigma\phi_d$	dresser block angle
ϕ_d	outside pressure angle
ψ	cradle rotation
ψ_m	spiral angle
$\overline{\omega}$	angular velocity vector

Subscripts g and p refer to gear and pinion, respectively.

NOMENCLATURE

(For Chapter III)

$\bar{a}$	acceleration vector
$\bar{F}$	external force vector
$\bar{F}c$	tooth contact force
$\bar{F}r$	bearing reaction force
FMA	scalar quantity of contact force
$\bar{H}_G$	angular momentum about gravity center
$\bar{i}$, $\bar{j}$, $\bar{k}$	unit vector
I	central mass moment of inertia about the principal axis of inertia
J	equivalent mass
ks	combined tooth contact stiffness
m	mass
$\bar{M}_G$	vector of external moment about gravity center
$\bar{\gamma}_c$	position vector from gravity center to the tooth contact point
$\bar{\gamma}_r$	position vector from gravity center to the bearing reaction point
RBG	radius of effective base circle of gear

RBP	radius of effective base circle of pinion
T_c	static force
x, y, z	translational displacement
θ	rotational displacement
$\overline{\Omega}$	relative rotational velocity of moving coordinate to fixed coordinate
ω	nominal shaft velocity
{ }	column matrix
[ ]	matrix form
[C]	damping matrix
[DC]	transformation matrix
[DG]	transformation matrix
[DK]	transformation matrix
$\{G_{ni}\}$	normal displacement at point i due to rigid body motion
{K}	stiffness matrix
[m]	mass matrix
$\{\delta_{nci}\}$	normal displacement at point i due to tooth contact force

$[\theta^u]$ transformation matrix

$[\theta^k]$ transformation matrix

Subscripts p , g refer to pinion and gear.

NOMENCLATURE

(For Chapter IV)

a	thermal diffusivity
AMAX	length of semi-major axis of contact ellipse
BMAX	length of semi-minor axis of contact ellipse
E'	effective elastic modulus
G	material parameter
G_∞	limiting elastic shear modulus
h	film thickness
h_j	surface heat transfer coefficient for oil jet cooling
h_s	surface heat transfer coefficient for free convective cooling
h_t	surface heat transfer coefficient for air/oil mist cooling
H_{min}	dimensionless film thickness of point contact solution
$H_{min,\ell}$	dimensionless film thickness of line contact solution
k	solid material thermal conductivity
k_o	oil thermal conductivity
K	ellipticity parameter
ℓ	length of contact stripe

P	pressure
q	heat flux
Q	heat flux at tooth contact point
R	nominal length, effective radius
T	temperature
T_{ave}	average temperature over whole contact ellipse
T_B	bulk temperature
T_f	flash temperature
T_{mid}	temperature at shear plane
u, V	speed
U	speed parameter
v	sliding velocity
w	load per unit length
W_D	load parameter
Z_m	distance from solid surface to shear plane
α	heat partition coefficient, pressure dependent viscosity parameter
$\dot{\gamma}$	shear rate

$\hat{\dot{\gamma}}$	dimensionless shear rate ($\dot{\gamma}\ \mu_o/\tau_L$)
$\hat{\gamma}$	shear rate of elastic part
$\hat{\gamma}$	shear rate of viscous part
η	atmosphere viscosity of lubricant
μ	low shear stress viscosity
τ	shear stress
$\hat{\tau}$	dimensionless shear stress (τ/τ_L)
τ_L	limiting shear stress

APPENDIX A

SAMPLE DATA FOR MACHINE SETTINGS

	Gear	Pinion	
		Concave	Convex
Number of Teeth	36		12
Face Width		1.00	
Shaft Angle		1.5708	
Outer Cone Distance		3.691	
Addendum	0.093		0.231
Dedendum	0.267		0.129
Pitch Angle	1.249		0.3217
Face Angle	1.276		0.3895
Root Angle	1.1813		0.2944
Spiral Angle		0.61086	
Nominal Wheel Diameter		6.0	
Machine Center to Back	0.0	-0.067	0.060
Sliding Base	-0.016	-0.009	-0.046
Blank Offset	0.000	0.041	-0.045
Cam Setting	6.916	7.089	7.279
Eccentric Angle	0.3598	0.3616	0.3604
Cradle Angle	1.2116	5.3354	5.4990
Cam Guide Angle	0.0	0.0	0.0
Standard Cam Setting	7.00	7.00	7.00
Cam Pitch Radius	6.2273	5.9567	5.9567
Index Interval	11	11	11

APPENDIX A (continued)

	Gear	Pinion	
		Concave	Convex
Dresser Block Angle	0.7854	0.7854	
Outside Pressure Angle	0.3490	0.3490	0.3482
Side Dresser Radial	3.113	3.028	2.959
Outside Dresser Arm Length	1.0	1.0	1.0
Outside Diamond Setting	0.0	0.0	0.171
Inside Dresser Arm Length	1.0	1.0	1.0
Inside Diamond Setting	0.223	0.170	0.0
Side Dresser Axial	0.0	0.023	0.029
Side Dresser Offset	1.00	0.800	1.200

APPENDIX B

From the geometry of Fig. 2-10, the motion formulas for a standard cam rotation ε_o are obtained as follows:

$$\psi_o = \frac{\eta_u}{DC + \eta_u} \varepsilon_o \tag{B-1}$$

$$\sin \psi_2 = \sin \psi_o + \sin a + \frac{\Delta\eta_u}{DC} \sin(\varepsilon_o - \psi_o) \tag{B-2}$$

$$\psi = \psi_2 - 2 \tag{B-3}$$

$$\varepsilon_2 = \varepsilon_o + \psi_2 + \psi_o \tag{B-4}$$

$$\varepsilon = \varepsilon_2 - a \tag{B-5}$$

$$\lambda = \frac{n_i}{n} \varepsilon \tag{B-6}$$

From (B-1) $$\frac{d\psi_o}{d\varepsilon_o} = \frac{\eta_u}{DC + \eta_u}$$

Differentiating (B-2) with respect to ε_o

$$\cos \psi_2 \frac{d\psi_2}{d\varepsilon_o} = \cos \psi_o \frac{d\psi_o}{d\varepsilon_o} + \frac{\Delta\eta_u}{DC} \cos(\varepsilon_o - \psi_o)(1 - \frac{d\psi_o}{d\varepsilon_o})$$

$$\frac{d\psi}{d\varepsilon o} = \frac{d\psi_2}{d\varepsilon_o} = \sec \psi_2 \left[\frac{\eta_u}{DC + \eta_u} \cos \psi_o + \frac{\Delta\eta_u}{DC + \eta_u} \cos(\varepsilon_o - \psi_o) \right]$$

$$= N \frac{\sec \psi_2}{DC + \eta_u} \tag{B-7}$$

where $N = \eta_u \cos \psi_o + \Delta\eta_u \cos(\varepsilon_o - \psi_o)$

From (B-4) and (B-5)

$$\frac{d\varepsilon}{d\varepsilon_o} = \frac{d\varepsilon_2}{d\varepsilon_o} = 1 + \frac{d\psi_2}{d\varepsilon_o} - \frac{d\psi_o}{d\varepsilon_o}$$

$$= 1 + N \frac{\sec \psi_2}{DC + \eta_u} - \frac{\eta_u}{DC + \eta_u}$$

$$= D \frac{\sec \psi_2}{DC + \eta_u} \qquad \text{(B-8)}$$

where $D = DC \cos \psi_2 + N$ and also $\frac{d\lambda}{d\varepsilon_o} = \frac{n_i}{n} = \frac{d\varepsilon}{d\varepsilon_o}$

$$\frac{d\psi}{d\lambda} = \frac{d\psi}{d\varepsilon_o} \frac{d\varepsilon_o}{d\lambda} = \frac{d\psi}{d\varepsilon_o} \frac{d\varepsilon_o}{d\varepsilon} \frac{n}{n_i}$$

$$= \frac{n}{n_i} \frac{N}{D} \qquad \text{(B-9)}$$

The term $\alpha_c = \left[\frac{\partial^2 \psi}{\partial \lambda^2}\right]$ used in determining the motion parameters is derived as follows:

$$\frac{d^2\psi}{d\lambda^2} = \frac{n}{n_i} \frac{1}{D^2} \left[D \frac{dN}{d\lambda} - N \frac{dD}{d\lambda}\right]$$

$$= \left(\frac{n}{n_i}\right)^2 \frac{1}{D^2} \left[D \frac{dN}{d\varepsilon} - N \frac{dD}{d\varepsilon}\right]$$

$$= \left(\frac{n}{n_i}\right)^2 \frac{(DC + \eta_u)}{D^3} \cos \psi_2 \left(D \frac{dN}{d\varepsilon_o} - N \frac{dD}{d\varepsilon_o}\right) \qquad \text{(B-10)}$$

and

$$\frac{dN}{d\varepsilon_o} = - \eta_u \sin \psi_o \frac{d\psi_o}{d\varepsilon_o} - \Delta\eta_u \sin\left(\varepsilon_o - \psi_o\right)\left(1 - \frac{d\psi_o}{d\varepsilon_o}\right)$$

$$= - \frac{AM}{DC + \eta_u} \qquad \text{(B-11)}$$

where

$$AM = \eta_u^2 \sin \psi_o + \Delta\eta \, DC \sin(\varepsilon_o - \psi_o)$$

$$\frac{dD}{d\varepsilon o} = - DC \sin \psi_2 \frac{d\psi_2}{d\varepsilon_o} = \frac{AM}{DC + \eta_u} \qquad \text{(B-12)}$$

$$= \frac{1}{DC + \eta_u} [DC \, N \tan \psi_2 + AM) \qquad \text{(B-12)}$$

$$\therefore \quad \frac{d^2\psi}{d\lambda^2} = \left(\frac{n}{n_i}\right)^2 \frac{\cos \psi_2}{D^3} \{N(DC \, N \tan \psi_2 + AM) - D \, AM\} \qquad \text{(B-13)}$$

APPENDIX C

The details of the mass, viscous and stiffness matrices of the equation of motion are shown here.

MAXC	Number of contact points at each time
AXYZCG (I,K)	Normal vector of gear surface at contact point (inward to gear body)
AXYZCP (I,K)	Normal vector of pinion surface at contact point (outward to pinion body)
AI (J,K)	Stiffness of contact point I due to a unit load applied at contact point K
XGG, YGG, ZGG	Translational displacements of gear gravity center
AXG, AYG, AZG	Rotational displacements of gear body
SGP, YGP, ZGP	Translational displacements of pinion gravity center
AXP, AYP, AZP	Rotational displacements of pinion body
SYZCG (I,K)	Position vector from gear gravity center to contact point K
XYZCP (I,K)	Position vector from pinion gravity center to contact point K

where I = 1, 2, 3 indicates the component in three-dimensional axis. J and K equal one to MAXC. Array ABG (J,I), J = 1 to 12, I - 1 to MAXC was introduced for convenience in developing equations:

$$ABG(1,I) = \sum_{K} - AI(I,K)*AXYZCG(1,K)$$

$$ABG(2,I) = \sum_K - AI(I,K)*AXYZCG(2,K)$$

$$ABG(3,I) = \sum_K - AI(I,K)*AXYZCG(3,K)$$

$$ABG(4,I) = \sum_K - AI(I,K)[XYZCG(2,K)*AXYZCG(3,K) - XYZCG(3,K)*AXYZCG(2,K)]$$

$$ABG(5,I) = \sum_K - AI(I,K)[AYZCG(3,K)*AXYZCG(1,K) - XYZCG(1,K)*AXYZCG(3,K)]$$

$$ABG(6,K) = \sum_K - AI(I,K)[XYZCG(1,K)*AXYZCG(2,K) - XYZCG(2,K)*AXYZCG(1,K)]$$

$$ABG(7,I) = \sum_K AI(I,K)*AXYZCP(1,K)$$

$$ABG(8,I) = \sum_K AI(I,K)*AXYZCP(2,K)$$

$$ABG(9,I) = \sum_K AI(I,K)*AXYZCP(3,K)$$

$$ABG(10,I) = \sum_K AI(I,K)[XYZCP(2,K)*AXYZCP(3,K) - XYZCP(3,K)*AXYZCP(2,K)]$$

$$ABG(11,I) = \sum_K AI(I,K)[XYZCP(3,K)*AXYZCP(1,K) - XYZCP(1,K)*AXYZCP(3,K)]$$

$$ABG(12,I) = \sum_K AI(I,K)[XYZCP(1,K)*AXYZCP(2,K) - XYZCP(2,K)*AXYZCP(1,K)]$$

The summation is from K = 1 to K = KMAXC, and I = 1 to KMAXC.

The force situation is shown in Fig. 3-1 and Fig. C-1.

For the gear, the components of the contact force are

$$\text{AXYZCG}\ (1,I)\ \{\text{ABG}(J,I)\}^T \begin{Bmatrix} D_g \\ D_p \end{Bmatrix} \bar{i}_g$$

$$+\text{AXYZCG}\ (2,I)\ \{\text{ABG}(J,I)\}^T \begin{Bmatrix} D_g \\ D_p \end{Bmatrix} \bar{j}_g$$

$$+\text{AXYZCG}\ (3,I)\ \{\text{ABG}(J,I)\}^T \begin{Bmatrix} D_g \\ D_p \end{Bmatrix} \bar{k}_g \qquad J = 1 \text{ to } 12$$

where { } denotes column matrix, $\begin{Bmatrix} D_g \\ D_p \end{Bmatrix}^T$ = (XGG, YGG, ZGG, AXG, AYG, AZG, XGP, YGP, ZGP, AXP, AYP, AZP) and I from one to MAXC. The damping force at contact point I is

the force terms due to bearing reaction are

$$-2\text{KXP}*\text{XGP} + \text{KXP}(\text{RIP}-\text{R2P})*\text{AZP}\ \bar{i}_p$$

$$-\text{KYP}*\text{YGP}\ \bar{j}_p$$

$$-2\text{KZP}*\text{ZGP} + \text{KZP}(\text{R2P}-\text{R1P})*\text{AXP}\ \bar{k}_p$$

and the torque due to these bearing forces are

$$-(\text{R1P}-\text{YGP}_o)\text{KZP}*\text{ZGP}-(\text{R1P}-\text{YGP}_o)^2\text{KZP}*\text{AXP}$$

$$+(\text{R2P}+\text{YGP})\text{KZP}-(\text{R2P}+\text{YGP}_o)\text{KZP} + \text{AXP}\ \bar{i}_p$$

$$+(\text{R1P}-\text{YGP}_o)\text{KXP}*\text{XGP}-(\text{RIP}-\text{YGP}_o)^2\text{KXP}*\text{AZP}$$

$$=(\text{R2P}+\text{YGP}_o)\text{KXP}*\text{XGP}-(\text{R2P}+\text{YGP}_o)^2\text{KXP}*\text{AZP}\ \bar{k}_p$$

where YGP_o is the rigid body displacement of the pinion in the pinion fixed coordinate.

The damping force due to the bearing is

$$C'_{xp}*\dot{XGP} + C'_{azp}*\dot{AZP}\ \ \bar{i}_p$$

$$+C'_{yp}*\dot{YGP}\ \ \bar{j}_p$$

$$+C'_{zp}*\dot{ZGP} + C'_{axp}*\dot{AXP}\ \ \bar{k}_p$$

and the damping torque is

$$C''_{zp}*\dot{ZGP} + C''_{axp}*\dot{AXP}\ \ \bar{i}_p$$

$$+C''_{xp}*\dot{XGP} + C''_{azp}*\dot{AZP}\ \ \bar{k}_p$$

Now the coefficients of damping will be determined. Let I = 1 to MAXC and introduce array CBG(j,I), J = 1 to 12 for convenience, and define

```
CBG (1,I) = -AXYZCG(1,I)
CBG (2,I) = -AXYZCG(2,I)
CBG (3,I) = -AXYZCG(3,I)
CBG (4,I) = -[XYZCG(2,I)*AXYZCG(3,I)-XYZCG(3,I)*AXYZCG(2,I)]
CBG (5,I) = -[XYZCG(3,I)*AXYZCG(1,I)-XYZCG(1,I)*AXYZCG(3,I)]
CBG (6,I) = -[XYZCG(1,I)*AXYZCG(2,I)-XYZCG(2,I)*AXYZCG(1,I)]
CBG (7,I) = AXYZCP(1,I)
CBG (8,I) = AXYZCP(2,I)
CBG (9,I) = AXYZCP(3,I)
CBG(10,I) = XYZCP(2,I)*AXYZCP(3,I)-XYZCP(3,I)*AXYZCP(2,I)
```

CBG (11,I) = XYZCP(3,I)*AXYZCP(1,I)-XYZCP(1,I)*AXYZCP(3,I)

CBG (12,I) = XYZCP(1,I)*AXYZCP(2,I)-XYZCP(2,I)*AXYZCP(1,I)

For gear, J = 1 to 12

C_{cxg} = AXYZCG(1,I) {CGB(J,I)}^{T} C_c

C_{cyg} = AXYZCG(2,I) {CBG(J,I)}^{T} C_c

C_{czg} = AXYZCG(3,I) {CBG(j,I)}^{T} C_c

C'_{cxg} = [XYZCG(2,I)*AXYZCG(3,I)-XYZCG(3,I)*AXYZCG(2,I)]
{CBG(J,I)}^{T} C_c

C'_{cyg} = [XYZCG(3,I)*AXYZCG(1,I)-XYZCG(1,I)*AXYZCG(3,I)]
{CBG(J,I)}^{T} C_c

C'_{czg} = [XYZCG(1,I)*AXYZCG(2,I)-XYZCG(2,I)*AXYZCG(1,I)]
{CBG(J,I)}^{T} C_c

C'_{xg} = -COG

C'_{yg} = -C1G - C2G

C'_{azg} = C1G*(R1G-XGG$_o$)-C2G*(R2G-XGG$_o$)

C'_{zg} = -C1G-C2G

C'_{ayg} = -C1G*(R1G+XGG$_o$)+C2G*(R2G-XGG$_o$)

C''_{zg} = -(R1G+XGG$_o$)C1G+(R2G-XGG$_o$)C2G

C''_{azg} = -(R1G+XGG$_o$)^2 C1G-(R2G-XGG$_o$)^2 C2G

$$C''_{yg} = (R1G+XGG_o)C1G-(R2G-XGG_o)C2G$$

$$C''_{ayg} = -(R1G+XGG_o)^2\ C1G-(R2G-XGG_o)^2C2G$$

For pinion, J = 1 to 12

$$C_{cxp} = -AXYZCP(1,I)\{CBG(J,I)\}^T\ C_c$$

$$C_{cyp} = -AXYZCP(2,I)\{CBG(J,I)\}^T\ C_c$$

$$C_{cap} = -AXYZCP(3,I)\{CBG(J,I)\}^T\ C_c$$

$$C_{cxg}\begin{Bmatrix}\dot{D}_g\\ \dot{D}_p\end{Bmatrix}\bar{i}_g + C_{cyg}\begin{Bmatrix}\dot{D}_g\\ D_p\end{Bmatrix}\bar{j}_g + C_{czg}\begin{Bmatrix}\dot{D}_g\\ D_p\end{Bmatrix}\bar{k}_g$$

The torque due to this contact force is

$$[XYZCG(2,I)*AXYZCG(3,I)-XYZCG(3,I)*AXYZCG(2,I)]\ \{ABG(J,I)\}^T \begin{Bmatrix}D_g\\ D_p\end{Bmatrix}\bar{i}_g$$

$$+\ [XYZCG(2,I)*AXYZCG(3,I)-XYZXG(3,I)*AXYZCG(2,I)]\ \{ABG(J,I)\}^T \begin{Bmatrix}D_g\\ D_p\end{Bmatrix}\bar{j}_g$$

$$+\ [XYZCG(1,I)*AXYZCG(2,I)-XYZCG(2,I)*AXYZCG(1,I)]\ \{ABG(J,I)\}^T \begin{Bmatrix}D_g\\ D_p\end{Bmatrix}\bar{k}_g$$

and the damping torque is

$$C'_{cxg} \begin{Bmatrix} \dot{D}_g \\ \dot{D}_p \end{Bmatrix} \bar{i}_g + C'_{cyg} \begin{Bmatrix} \dot{D}_g \\ \dot{D}_p \end{Bmatrix} \bar{j}_g + C'_{czg} \begin{Bmatrix} \dot{D}_g \\ \dot{D}_p \end{Bmatrix} \bar{k}_g$$

The force terms due to the bearing reaction are

$$-KXG + XGG\ \bar{i}_g$$

$$-2KYG*YGG+KYG*(R\pm G+XGG)-KYG*(R2G-XGG)\ \bar{j}_g$$

$$-2KZG*ZGG-KZG*(R1G+XGG)*AYG+KZG*(R2G-XGG)*AYG\ \bar{k}_g$$

The torque terms due to these bearing reactions are

$$-R1G+XGG_o)*KZG\ ZGG-(R1G+XGG_o)^2*KZG*AYG$$

$$+R2G-XGG_o)*KZG*ZGG-(R2G-XGG_o)^2*KZG*AYG\ \bar{j}_g$$

$$+(R1G+XGG_o)*KYG*YGG-(R2G-XGG_o)^2\ *KYG\ AZG\ \bar{k}_g$$

where XGG_o is the rigid body displacement of gear in the gear fixed coordinate.

The damping force is

$$c'_{xg} * \dot{XGG}\ \bar{i}_g$$

$$c'_{yg} * \dot{ZGG} + C'_{azg} * \dot{AZG}\ \bar{j}_g$$

$$c'_{zg} * \dot{ZGG} + C'_{ayg} * \dot{AYG}\ \bar{k}_g$$

and the damping torque is

$$c''_{zg} * \dot{ZGG} + C''_{ayg} * \dot{AYG}\ \bar{j}_g$$

$$C''_{yg} * \dot{YGG} + C''_{ayg} * \dot{AZG}\ \bar{k}_g$$

For pinion case, the components of contact force are

$$-AXYZCP(1,I)\ \{ABG(J,I)\}^T \begin{Bmatrix} D_g \\ D_p \end{Bmatrix} \bar{i}_p$$

$$-AXYZCP(2,I)\ \{ABG(J,I)\}^T \begin{Bmatrix} D_g \\ D_p \end{Bmatrix} \bar{j}_p$$

$$-AXYZCP(3,I)\ \{ABG(J,I)\}^T \begin{Bmatrix} D_g \\ D_p \end{Bmatrix} \bar{k}_p \qquad I = 1 \text{ to MAXC and}$$

$$J = 1 \text{ to } 12$$

the damping force at contact point I is

$$C_{cxp} \begin{Bmatrix} \dot{D}_g \\ \dot{D}_p \end{Bmatrix} \bar{i}_p + C_{cyp} \begin{Bmatrix} \dot{D}_g \\ \dot{D}_p \end{Bmatrix} \bar{j}_p + C_{czp} \begin{Bmatrix} \dot{D}_g \\ \dot{D}_p \end{Bmatrix} \bar{k}_p$$

the torque due to this contact force is

$$-[XYZCP(2,I)*AXYZCP(3,I)-XYZCP(3,I)*AXYZCP(2,I)\ \{ABG(J,I)\}^T \begin{Bmatrix} D_g \\ D_p \end{Bmatrix} \bar{i}_p$$

$$-[XYZCP(3,I)*AXYZCP(1,I)-XYZCP(1,I)*AXYZCP(3,I)]\{ABG(J,I)\}^T \begin{Bmatrix} D_g \\ D_p \end{Bmatrix} \bar{j}_p$$

$$-[XYZCP(1,I)*AXYZCP(2,I)-XYZCP(2,I)*AXYZCP(1,I)]\{ABG(J,I)\}^T \begin{Bmatrix} D_g \\ D_p \end{Bmatrix} \bar{k}_p$$

J = 1 to 12 and the damping torque is

$$C'_{cxp}\begin{Bmatrix}\dot{D}_g\\ \dot{D}_p\end{Bmatrix} + C'_{cyp}\begin{Bmatrix}\dot{D}\\ \dot{D}_p\end{Bmatrix}\bar{j}_p + C'_{czp}\begin{Bmatrix}\dot{D}_g\\ \dot{D}_p\end{Bmatrix}\bar{k}_p$$

$$C'_{cxp} = -[XYZCP(2,I)*AXYZCP(3,I)-XYZCP(3,I)*AXYZCP(2,I)]$$
$$\{CBG(J,I)\}^T C_c$$

$$C'_{cyp} = -[XYZCP(3,I)*AXYZCP(1,I)-XYZCP(1,I)*AXYZCP(3,I)]$$
$$\{CBG(J,I)\}^T C_c$$

$$C'_{czp} = -[XYZCP(1,I)*AXYZCP(2,I)-XYZCP(2,I)*AXYZCP(1,I)]$$
$$\{CBG(J,I)\}^T C_c$$

$$C'_{xp} = -C1P - C2P$$

$$C'_{azp} = C1P*(R1P-YGP_o) - C2P*(R2P+YGP_o)$$

$$C'_{yp} = -COP$$

$$C'_{zp} = -C1P - C2P$$

$$C'_{axp} = -C1P*(R1P-YGP_o) + C2P*(R2P+YGP_o)$$

$$C''_{zp} = -(R1P-YGP_o)C1P + (R2P+YGP_o)C2P$$

$$C''_{axp} = -(R1P-YGP_o)^2C1P-(R2P+YGP_o)^2C2P$$

$$C''_{xp} = (R1P-YGP_o)C1P-(R2P+YGP_0)C2P$$

$$C''_{azp} = -(R1P-YGP_o)^2C1P-(R2P+YGP_o)^2C2P$$

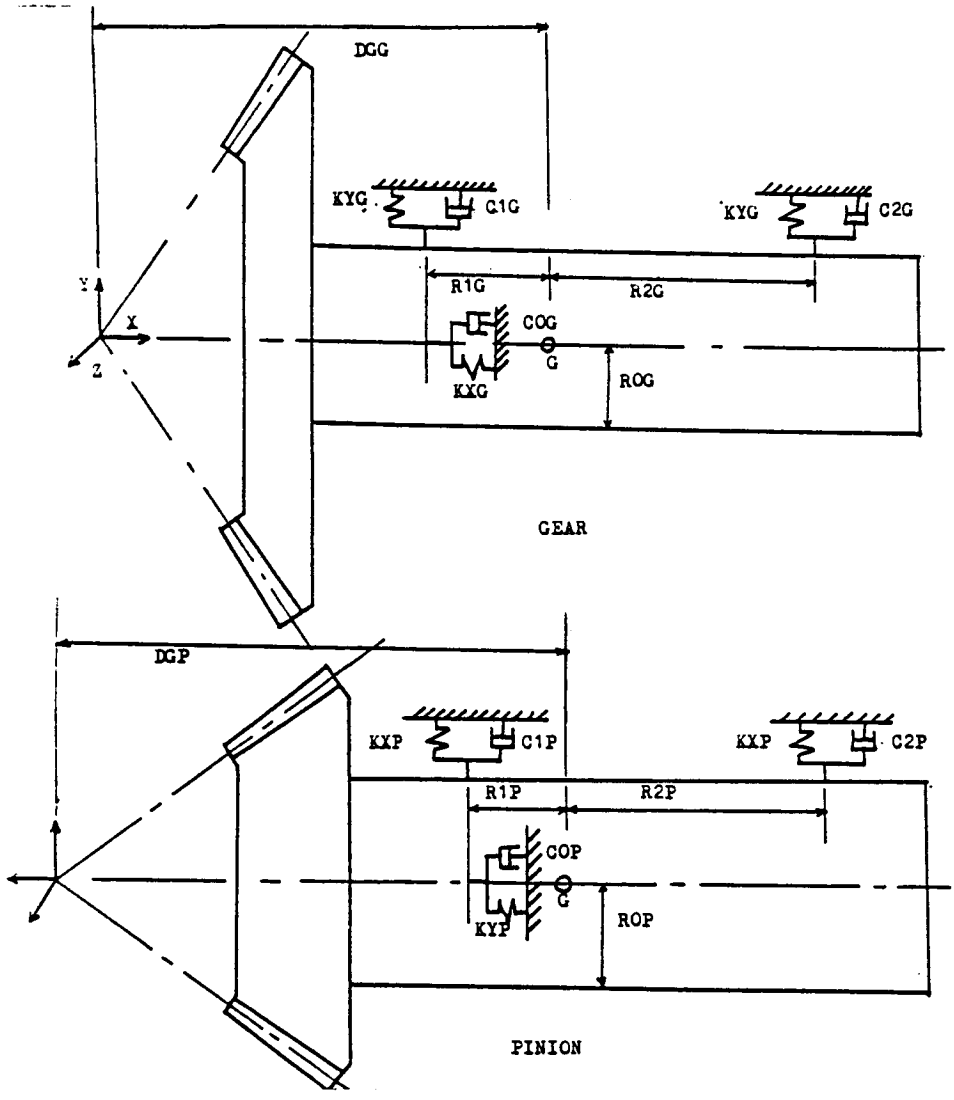

Fig. C-1. Bearing Force Configuration

APPENDIX D

INTERPOLATION OF THE COEFFICIENTS OF DEFLECTION AND BULK TEMPERATURE

(A) Deflection Coefficient

There are thirty nodal points in the contacting tooth surface. The deflection coefficient D_{ij} is the deflection (normal direction) at point i due to a unit load applied at point j. The coefficient $D_{\lambda j}$ was obtained from the finite element method. Fig. D-1 shows these grid points in the axial plane and also shows the contact path. It is desired to determine the deflection D_I^C at contact point I in surface element α with four corner points j1, j2, j3 and j4, due to a unit load at this point I. The concept of the shape function used in the finite element method was borrowed here to solve the problem. A mapping diagram is shown in Fig. D-2, correspondent to Fig. D-1. All the surface elements in this mapping diagram are of the same size as the square shape. Introducing two new local coordinate variables r and s, one can obtain the deflection at I by

$$D_I^C = 0.25*(1-r)*(1-s)*D_{J1,J1} + 0.25*(1+r)*(1-s)*D_{J2,J2}$$
$$+ 0.25*(1+r)*(1+s)*D_{J3,J3} + 0.25*(1-r)*(1+s)*D_{J4,J4}$$

r, s are defined as

$$X_J = 0.25*(1-r)*(1-s)*X_{J1} + 0.25*(1+r)*(1-s)*X_{J2}$$
$$+ 0.25*(1+r)*(1+s)*X_{J3} + 0.25*(1-r)*(1+s)*X_{J4}$$

$$Y_J = 0.25*(1-r)*(1-s)*Y_{J1} + 0.25*(1+r)*(1-s)*Y_{J2}$$
$$+ 0.25*(1+r)*(1+s)*Y_{J3} + 0.25*(1-r)*(1+s)*Y_{J4}$$

which X and Y are the coordinates in the axial plane.

(B) Bulk Temperature

The temperature rise (T_I^C) at contact point I due to a unit heat flux at the same point can be calculated the same way as that for the deflection coefficient. If T_{ij} is the temperature rise at nodal point i due to a unit heat flux at nodal point j, then

$$T_J^C = 0.25*(1-)*(1-s)*T_{J1,J1} + 0.25*(1+r)*(1-s)*T_{J2,J2}$$
$$+ 0.25*(1+r)*(1+s)T_{J3,J3} + 0.25*(1-r)*(1-s)*T_{J4,J4}$$

Now the temperature rise ($T_{J,I}^C$) at contact point J due to a unit heat flux at contact point I ($I \neq J$) has to be determined. If point J is far away from point I, then the temperature rise at point J will not be influenced by the local temperature jump at point I. Fig. D-3 shows this situation where contact I is in surface element β with nodal points I1, I2, I3, I4 and contact point J is in surface element α with nodal point J1, J2, J3 and J4. The temperature rise at nodal points I1, I2, I3, and I4 due to heat flux at contact point J is

$$T_{II,J} = 0.25*(1-r_J)*(1-s_J)*T_{II,J1} + 0.25*(1+r_J)*(1-s_J)*T_{II,J2}$$
$$+ 0.25*(1+r_J)*(1+s_J)*T_{II,J3} + 0.25*(1-r_J)*(1+s_J)*T_{II,J4}$$

where II = I1, I2, I3 and I4, respectively, and r_J, s_J are local

coordinates in surface element α. Then the temperature rise at contact point I will be

$$T^{C}_{I,J} = 0.25*(1-r_I)*(1-s_I)*T_{I1,J} + 0.25*(1+r_I)*(1-s_I)*T_{I2,J}$$
$$+ 0.25*(1+r_I)*(1+s_I)*T_{I3,J} + 0.25*(1-r_I)*(1+s_I)*T_{I4,J}$$

where γ_I and S_I are local coordinates in surface element β.

If contact point I is close to contact point J, the local temperature effect should be counted. One can make a square with the same size as any other squares so that the contact point I will be within this square and contact point J will become one of the four corner points of this square (see Fig. D-4). Then the temperature at each corner point due to heat flux at point J can be determined as above. Let r_I and s_I be the local coordinates in the new surface element, then

$$T^{C}_{I,J} = 0.25*(1-r_I)*(1-s_I)*T_J + 0.25*(1+r_I)*(1-s_I)*T_1$$
$$+ 0.25*(1+r_I)*(1+s_I)*T_2 + 0.25*(1-r_I)*(1+s_I)*T_3$$

the order of T_J, T_1, T_2 and T_3 will be changed, depending on how this new element is formed. In order to cover all the possible cases where this new element may locate, a new element layer was created to surround the original mapping diagram (as shown in Fig. D-4). The temperature at these new added grid points due to heat flux at any possible grid point was given artificially.

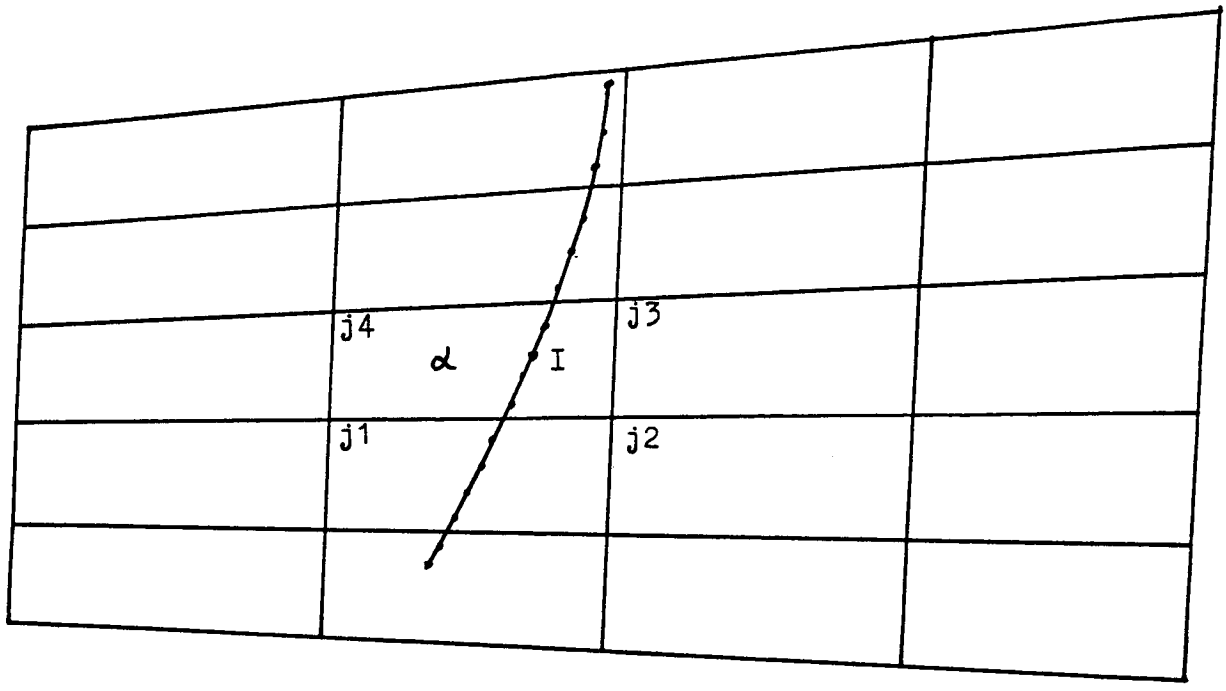

Fig. D-1. Grid Points And Contact Path in Axial Plane

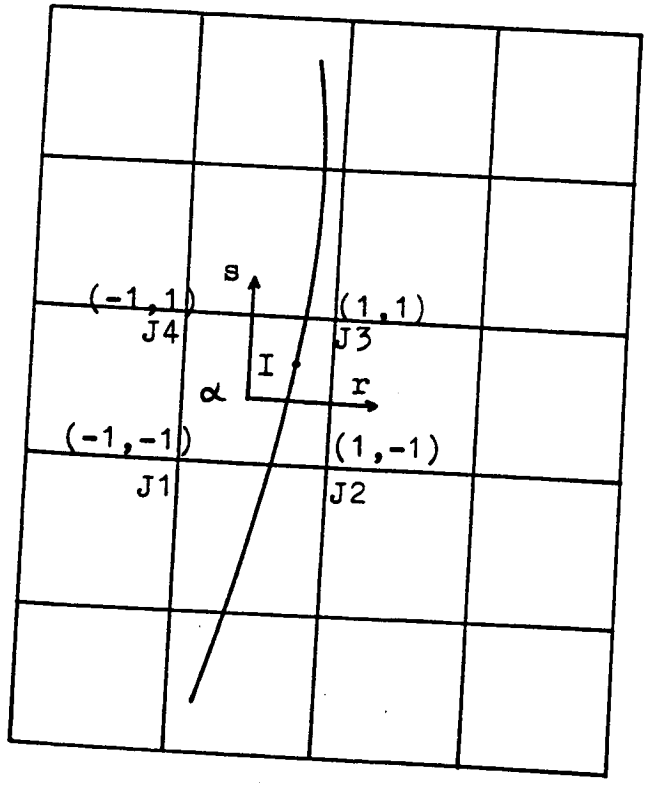

Fig. D-2. Mapping Diagram

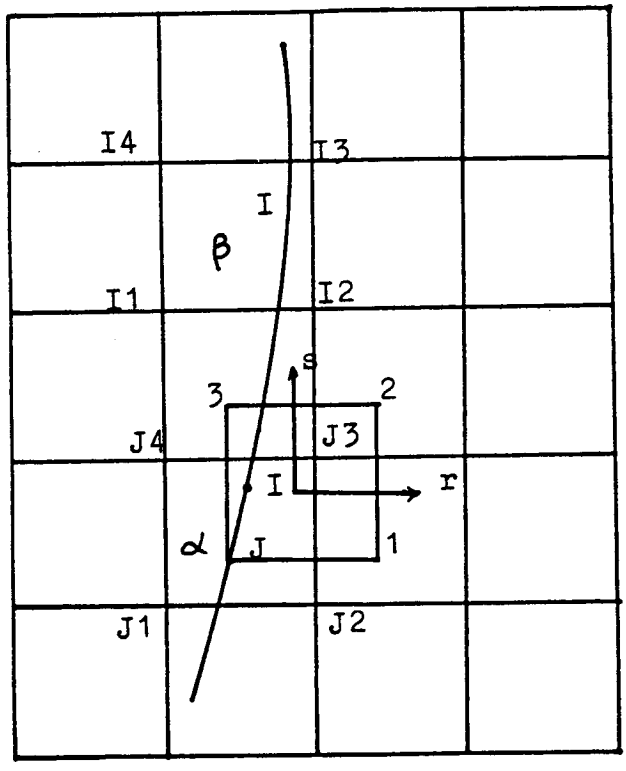

Fig. D-3. Mapping Diagram For Temperature Calculation

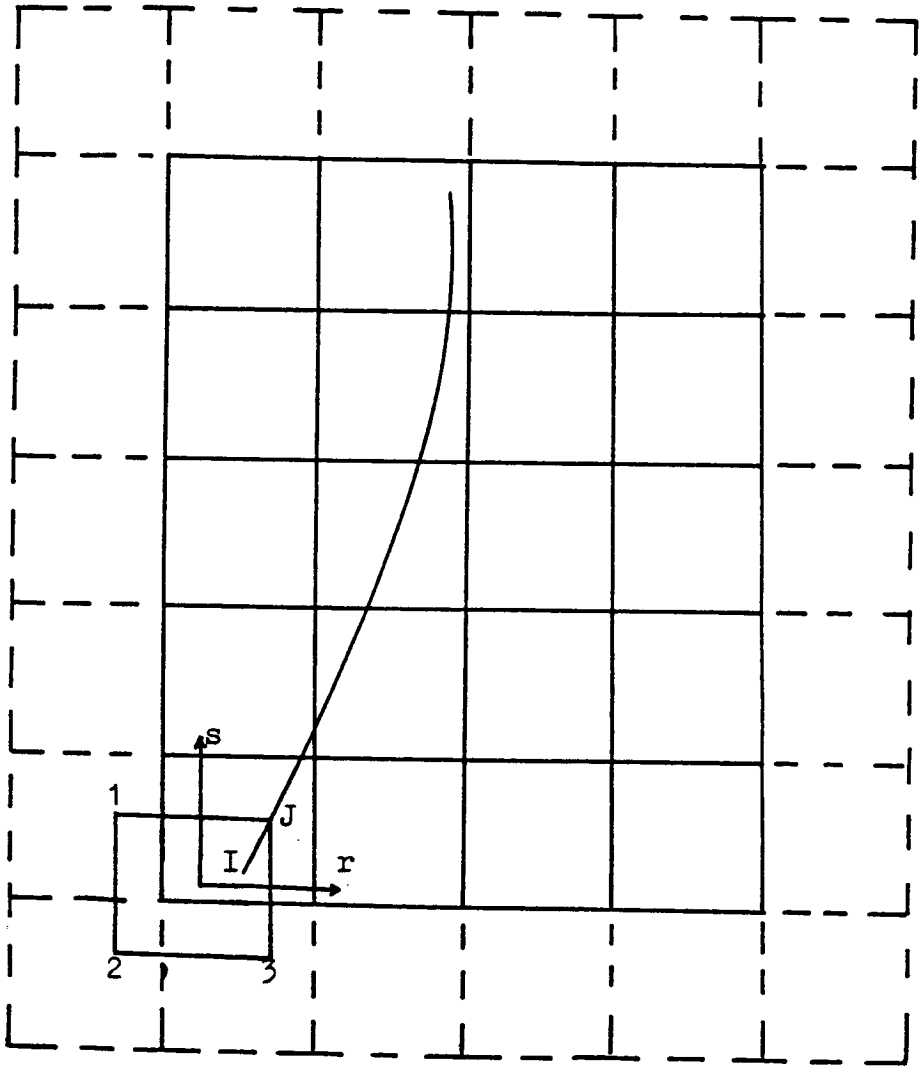

Fig. D-4. Mapping Diagram With A New Element Layer

NASA
National Aeronautics and Space Administration

Report Documentation Page

1. Report No.	2. Government Accession No.	3. Recipient's Catalog No.
NASA CR-4077 AVSCOM TR 87-C-17		

4. Title and Subtitle

A Computer Solution for the Dynamic Load, Lubricant Film Thickness and Surface Temperatures in Spiral Bevel Gears

5. Report Date
July 1987

6. Performing Organization Code

7. Author(s)
H. C. Chao and H. S. Cheng

8. Performing Organization Report No.
None (E-3540)

10. Work Unit No.
1L161102AH45
505-63-51

9. Performing Organization Name and Address
Northwestern University
Center for Engineering Tribology
Evanston, Illinois 60201

11. Contract or Grant No.
NSG-3143

13. Type of Report and Period Covered
Contractor Report
Final

12. Sponsoring Agency Name and Address
U.S. Army Aviation Research and Technology Activity - AVSCOM, Propulsion Directorate, Lewis Research Center, Cleveland, Ohio 44135 and NASA Lewis Research Center, Cleveland, Ohio 44135

14. Sponsoring Agency Code

15. Supplementary Notes
Project Manager, John J. Coy, Propulsion Directorate, U.S. Army Aviation Research and Technology Activity - AVSCOM, Lewis Research Center.

16. Abstract
A complete analysis of spiral bevel gear sets is presented. The gear profile is described by the movements of the cutting tools. The contact patterns of the rigid body gears are investigated. The tooth dynamic force is studied by combining the effects of variable teeth meshing stiffness, speed, damping, and bearing stiffness. The lubrication performance is also accomplished by including the effects of the lubricant viscosity, ambient temperature, and gear speed. A set of numerical results is also presented.

17. Key Words (Suggested by Author(s))
Gears; Spiral bevel gears; Transmissions; Machine design; Vibration; Lubrication

18. Distribution Statement
Unclassified - unlimited
STAR Category 37

19. Security Classif. (of this report)	20. Security Classif. (of this page)	21. No. of pages	22. Price*
Unclassified	Unclassified	204	A10

*For sale by the National Technical Information Service, Springfield, Virginia 22161

NASA-Langley, 1987